GEOTECHNICAL SPECIAL PUBLICATION NO. 194

Soils and Rock Instrumentation, Behavior, and Modeling



Edited by
Louis Ge, Ph.D., P.E.
Boming Tang, Ph.D.
WeiHong Wei, Ph.D.
Renpeng Chen, Ph.D.

ASCE
GEO INSTITUTE

GEOTECHNICAL SPECIAL PUBLICATION NO. 194

SOILS AND ROCK INSTRUMENTATION, BEHAVIOR, AND MODELING

SELECTED PAPERS FROM THE 2009 GEOHUNAN INTERNATIONAL CONFERENCE

August 3–6, 2009
Changsha, Hunan, China

HOSTED BY
Changsha University of Science and Technology, China

CO-SPONSORED BY
ASCE Geo-Institute, USA
Asphalt Institute, USA
Central South University, China
Chinese Society of Pavement Engineering, Taiwan
Chongqing Jiaotong University, China
Deep Foundation Institute, USA
Federal Highway Administration, USA
Hunan University, China
International Society for Asphalt Pavements, USA
Jiangsu Transportation Research Institute, China
Korea Institute of Construction Technology, Korea
Korean Society of Road Engineers, Korea
Texas Department of Transportation, USA
Texas Transportation Institute, USA
Transportation Research Board (TRB), USA

EDITED BY
Louis Ge, Ph.D., P.E.
Boming Tang, Ph.D.
WeiHong Wei, Ph.D.
Renpeng Chen, Ph.D.

Published by the American Society of Civil Engineers

Library of Congress Cataloging-in-Publication Data.

Soils and rock instrumentation, behavior, and modeling ; selected papers from the 2009 GeoHunan International Conference, August 3-6, 2009, Changsha, Hunan, China / hosted by Changsha University of Science and Technology, China ; co-sponsored by ASCE Geo-Institute, USA ; edited by Louis Ge.
p. cm. -- (Geotechnical special publication ; no. 194)
Includes bibliographical references and indexes.
ISBN 978-0-7844-1046-2
1. Road materials--Congresses. 2. Soils--Congresses. 3. Engineering geology--Instruments--Congresses. 4. Pavements--Congresses. I. Ge, Louis. II. Changsha li gong da xue. III. American Society of Civil Engineers. Geo-Institute. IV. GeoHunan International Conference on Challenges and Recent Advances in Pavement Technologies and Transportation Geotechnics (2009 : Changsha, Hunan Sheng, China)

TE200.S63 2009
624.1'51--dc22 2009022725

American Society of Civil Engineers
1801 Alexander Bell Drive
Reston, Virginia, 20191-4400

www.pubs.asce.org

Any statements expressed in these materials are those of the individual authors and do not necessarily represent the views of ASCE, which takes no responsibility for any statement made herein. No reference made in this publication to any specific method, product, process, or service constitutes or implies an endorsement, recommendation, or warranty thereof by ASCE. The materials are for general information only and do not represent a standard of ASCE, nor are they intended as a reference in purchase specifications, contracts, regulations, statutes, or any other legal document. ASCE makes no representation or warranty of any kind, whether express or implied, concerning the accuracy, completeness, suitability, or utility of any information, apparatus, product, or process discussed in this publication, and assumes no liability therefore. This information should not be used without first securing competent advice with respect to its suitability for any general or specific application. Anyone utilizing this information assumes all liability arising from such use, including but not limited to infringement of any patent or patents.

ASCE and American Society of Civil Engineers—Registered in U.S. Patent and Trademark Office.

Photocopies and reprints.
You can obtain instant permission to photocopy ASCE publications by using ASCE's online permission service (http://pubs.asce.org/permissions/requests/). Requests for 100 copies or more should be submitted to the Reprints Department, Publications Division, ASCE, (address above); email: permissions@asce.org. A reprint order form can be found at http://pubs.asce.org/support/reprints/.

Copyright © 2009 by the American Society of Civil Engineers. All Rights Reserved.
ISBN 978-0-7844-1046-2
Manufactured in the United States of America.

Geotechnical Special Publications

1 *Terzaghi Lectures*
2 *Geotechnical Aspects of Stiff and Hard Clays*
3 *Landslide Dams: Processes, Risk, and Mitigation*
7 *Timber Bulkheads*
9 *Foundations & Excavations in Decomposed Rock of the Piedmont Province*
11 *Dynamic Response of Pile Foundations - Experiment, Analysis and Observation*
14 *Geotechnical Aspects of Karst Terrains*
15 *Measured Performance Shallow Foundations*
16 *Special Topics in Foundations*
17 *Soil Properties Evaluation from Centrifugal Models*
18 *Geosynthetics for Soil Improvement*
19 *Mine Induced Subsidence: Effects on Engineered Structures*
21 *Hydraulic Fill Structures*
22 *Foundation Engineering*
23 *Predicted and Observed Axial Behavior of Piles*
24 *Resilient Moduli of Soils: Laboratory Conditions*
25 *Design and Performance of Earth Retaining Structures*
27 *Geotechnical Engineering Congress*
28 *Detection of and Construction at the Soil/Rock Interface*
29 *Recent Advances in Instrumentation, Data Acquisition and Testing in Soil Dynamics*
32 *Embankment of Dams - James L. Sherard Contributions*
33 *Excavation and Support for the Urban Infrastructure*
34 *Piles Under Dynamic Loads*
35 *Geotechnical Practice in Dam Rehabilitation*
37 *Advances in Site Characterization: Data Acquisition, Data Management and Data Interpretation*
39 *Unsaturated Soils*
40 *Vertical and Horizontal Deformations of Foundations and Embankments*
41 *Predicted and Measured Behavior of Five Spread Footings on Sand*
42 *Serviceability of Earth Retaining Structures*
43 *Fracture Mechanics Applied to Geotechnical Engineering*
44 *Ground Failures Under Seismic Conditions*
45 *In Situ Deep Soil Improvement*
46 *Geoenvironment 2000*
47 *Geo-Environmental Issues Facing the Americas*
48 *Soil Suction Applications in Geotechnical Engineering*
49 *Soil Improvement for Earthquake Hazard Mitigation*
50 *Foundation Upgrading and Repair for Infrastructure Improvement*
51 *Performance of Deep Foundations Under Seismic Loading*
52 *Landslides Under Static and Dynamic Conditions - Analysis, Monitoring, and Mitigation*
53 *Landfill Closures - Environmental Protection and Land Recovery*
54 *Earthquake Design and Performance of Solid Waste Landfills*
55 *Earthquake-Induced Movements and Seismic Remediation of Existing Foundations and Abutments*
56 *Static and Dynamic Properties of Gravelly Soils*
57 *Verification of Geotechnical Grouting*
58 *Uncertainty in the Geologic Environment*
59 *Engineered Contaminated Soils and Interaction of Soil Geomembranes*
60 *Analysis and Design of Retaining Structures Against Earthquakes*
61 *Measuring and Modeling Time Dependent Soil Behavior*
62 *Case Histories of Geophysics Applied to Civil Engineering and Public Policy*
63 *Design with Residual Materials: Geotechnical and Construction Considerations*
64 *Observation and Modeling in Numerical Analysis and Model Tests in Dynamic Soil-Structure Interaction Problems*
65 *Dredging and Management of Dredged Material*
66 *Grouting: Compaction, Remediation and Testing*
67 *Spatial Analysis in Soil Dynamics and Earthquake Engineering*
68 *Unsaturated Soil Engineering Practice*
69 *Ground Improvement, Ground Reinforcement, Ground Treatment: Developments 1987-1997*
70 *Seismic Analysis and Design for Soil-Pile-Structure Interactions*
71 *In Situ Remediation of the Geoenvironment*
72 *Degradation of Natural Building Stone*
73 *Innovative Design and Construction for Foundations and Substructures Subject to Freezing and Frost*

74 ***Guidelines of Engineering Practice for Braced and Tied-Back Excavations***
75 ***Geotechnical Earthquake Engineering and Soil Dynamics III***
76 ***Geosynthetics in Foundation Reinforcement and Erosion Control Systems***
77 ***Stability of Natural Slopes in the Coastal Plain***
78 ***Filtration and Drainage in Geotechnical/Geoenvironmental Engineering***
79 ***Recycled Materials in Geotechnical Applications***
80 ***Grouts and Grouting: A Potpourri of Projects***
81 ***Soil Improvement for Big Digs***
82 ***Risk-Based Corrective Action and Brownfields Restorations***
83 ***Design and Construction of Earth Retaining Systems***
84 ***Effects of Construction on Structures***
85 ***Application of Geotechnical Principles in Pavement Engineering***
86 ***Big Digs Around the World***
87 ***Jacked Tunnel Design and Construction***
88 ***Analysis, Design, Construction, and Testing of Deep Foundations***
89 ***Recent Advances in the Characterization of Transportation Geo-Materials***
90 ***Geo-Engineering for Underground Facilities***
91 ***Special Geotechnical Testing: Central Artery/Tunnel Project in Boston, Massachusetts***
94 ***Performance Confirmation of Constructed Geotechnical Facilities***
95 ***Soil-Cement and Other Construction Practices in Geotechnical Engineering***
96 ***Numerical Methods in Geotechnical Engineering: Recent Developments***
97 ***Innovations and Applications in Geotechnical Site Characterization***
98 ***Pavement Subgrade, Unbound Materials, and Nondestructive Testing***
99 ***Advances in Unsaturated Geotechnics***
100 ***New Technological and Design Developments in Deep Foundations***
101 ***Slope Stability 2000***
102 ***Trends in Rock Mechanics***
103 ***Advances in Transportation and Geoenvironmental Systems Using Geosynthetics***
104 ***Advances in Grouting and Ground Modification***
105 ***Environmental Geotechnics***
106 ***Geotechnical Measurements: Lab & Field***
107 ***Soil Dynamics and Liquefaction 2000***
108 ***Use of Geophysical Methods in Construction***
109 ***Educational Issues in Geotechnical Engineering***
110 ***Computer Simulation of Earthquake Effects***
111 ***Judgment and Innovation: The Heritage and Future of the Geotechnical Engineering Profession***
112 ***Soft Ground Technology***
113 ***Foundations and Ground Improvement***
114 ***Soils Magic***
115 ***Expansive Clay Soils and Vegetative Influence on Shallow Foundations***
116 ***Deep Foundations 2002: An International Perspective on Theory, Design, Construction, and Performance***
117 ***Discrete Element Methods: Numerical Modeling of Discontinua***
118 ***A History of Progress: Selected U.S. Papers in Geotechnical Engineering***
119 ***Soil Behavior and Soft Ground Construction***
120 ***Grouting and Ground Treatment***
121 ***Probabilistic Site Characterization at the National Geotechnical Experimentation Sites***
122 ***Sinkholes and the Engineering and Environmental Impacts of Karst***
123 ***Recent Advances in Materials Characterization and Modeling of Pavement Systems***
124 ***GeoSupport 2004: Drilled Shafts, Micropiling, Deep Mixing, Remedial and Specialty Foundation Systems***
125 ***Current Practices and Future Trends in Deep Foundations***
126 ***Geotechnical Engineering for Transportation Projects***
127 ***Recycled Materials in Geotechnics***
128 ***Soil Constitutive Models: Evaluation, Selection, and Calibration***
129 ***Advances in Designing and Testing Deep Foundations***
130 ***Advances in Pavement Engineering***
131 ***Contemporary Issues in Foundation Engineering***
132 ***Advances in Deep Foundations: In Memory of Michael W. O'Neill***
133 ***Earthquake Engineering and Soil Dynamics***
134 ***Soil Dynamics Symposium in Honor of Professor Richard D. Woods***
135 ***Erosion of Soils and Scour of Foundations***

136 *Innovations in Grouting and Soil Improvement*
137 *Legal and Liability Issues in Geotechnical Engineering*
138 *Site Characterization and Modeling*
139 *Calibration of Constitutive Models*
140 *Slopes and Retaining Structures under Seismic and Static Conditions*
141 *International Perspectives on Soil Reinforcement Applications*
142 *Waste Containment and Remediation*
143 *Geomechanics: Testing, Modeling, and Simulation*
144 *Sinkholes and the Engineering and Environmental Impacts of Karst*
145 *Seismic Performance and Simulation of Pile Foundations in Liquefied and Laterally Spreading Ground*
146 *Asphalt Concrete: Simulation, Modeling and Experimental Characterization*
147 *Unsaturated Soils 2006*
148 *Advances in Unsaturated Soil, Seepage, and Environmental Geotechnics*
149 *Site and Geomaterial Characterization*
150 *Soil and Rock Behavior and Modeling*
151 *Advances in Earth Structures: Research to Practice*
152 *Ground Modification and Seismic Mitigation*
153 *Foundation Analysis and Design: Innovative Methods*
154 *Pavement Mechanics and Performance*
155 *Underground Construction and Ground Movement*
156 *Geomechanics II: Testing, Modeling, and Simulation*
157 *Computer Applications in Geotechnical Engineering*
158 *Contemporary Issues in Deep Foundations*
159 *Case Studies in Earth Retaining Structures*
160 *Dynamic Response and Soil Properties*
161 *Embankments, Dams, and Slopes: Lessons from the New Orleans Levee Failures and Other Issues*
162 *Problematic Soils and Rocks and In Situ Characterization*
163 *Geoenvironmental Engineering*
164 *Innovative Applications of Geophysics in Civil Engineering*
165 *Geosynthetics in Reinforcement and Hydraulic Applications*
166 *Educational Activities in Geotechnical Engineering*
167 *Geotechnics of Soil Erosion*
168 *Grouting for Ground Improvement: Innovative Concepts and Applications*
169 *Soil and Material Inputs for Mechanistic-Empirical Pavement Design*
170 *Probabilistic Applications in Geotechnical Engineering*
171 *Advances in Shallow Foundations*
172 *Soil Improvement*
173 *Advances in Measurement and Modeling of Soil Behavior*
174 *Designing Our Underground Space*
175 *Field Measurements in Geomechanics 2007*
176 *Analysis of Asphalt Pavement Materials and Systems: Emerging Methods*
177 *GeoCongress 2008: Geotechnics of Waste Management and Remediation*
178 *GeoCongress 2008: Geosustainability and Geohazard Mitigation*
179 *GeoCongress 2008: Characterization, Monitoring, and Modeling of GeoSystems*
180 *From Research to Practice in Geotechnical Engineering*
181 *Geotechnical Earthquake Engineering and Soil Dynamics IV*
182 *Pavements and Materials: Characterization, Modeling, and Simulation*
183 *Sinkholes and the Engineering and Environmental Impacts of Karst*
184 *Pavements and Materials: Modeling, Testing, and Performance*
185 *Contemporary Topics in Deep Foundations*
186 *Contemporary Topics in In-Situ Testing, Analysis, and Reliability of Foundations*
187 *Contemporary Topics in Ground Modification, Problem Soils, and Geo-Support*
188 *Advances in Ground Improvement: Research to Practice in USA and China*
189 *Characterization, Modeling, and Performance of Geomaterials*
190 *Asphalt Material Characterization, Accelerated Testing, and Highway Management*
191 *Road Pavement Material Characterization and Rehabilitation*
192 *Recent Advancement in Soil Behavior, In Situ Test Methods, Pile Foundations, and Tunneling*
193 *Material, Design, Construction, Maintenance, and Testing of Pavement*

This page intentionally left blank

Preface

The papers in this Geotechnical Special Publication were presented in the session of Soils and Rock Instrumentation, Behavior and Modeling at GeoHunan International Conference: Challenges and Recent Advances in Pavement Technologies and Transportation Geotechnics. The conference was hosted by Changsha University of Science and Technology on August 3-6, 2009.

This page intentionally left blank

Contents

Grout Efficiency of Lifting Structure in Soft Clay **1**
James -C. Ni and Wen-Chieh Cheng

Modeling Resilient Modulus of Unbound Granular Materials under Repeated Loading **9**
Cheng Chen, Louis Ge, and Jia Sheng Zhang

Study on the Deformation and Evolution Mechanism of Soil-Rock-Mixture Slope under Excavation Disturbance **16**
Zhong Zhou, Ru-Song Nie, Bao-Chen Liu, and Xiao-Li Yang

Development and Application of Constitutive Model for Simulation of Mechanical Behavior of Granular Material **24**
Xueyan Liu, A. Scarpas, C. Kasbergen, and W. X. Zhang

Application of Fuzzy Sets to Geological Strength Index (GSI) System Used in Rock Slope **30**
Yong-Jie Zhang, Wen-Gui Cao, and Ming-Hua Zhao

Measurement of Soil Air Suction Change during Freezing-Thawing Process **36**
Yan Liu, Xinbao Yu, and Xiong (Bill) Yu

Investigation of the Performance of Flexible Airport Pavements under Moving Aircraft Wheel Loads with Wander Using Finite Element Analysis **44**
Dona Johnson and Beena Sukumaran

Characteristics of Pore Pressure and Volume Change during Undrained Loading of Unsaturated Compacted Granite Soil **50**
Chan-Kee Kim, Woong-Ki Hwang, Yongkyu Choi, Minhee Lee, and Tae-Hyung Kim

Sonic Wave Testing Technique in Lamellar Rock Mass **57**
Qingfa Chen, Keping Zhou, and Feng Gao

The Pumping Test Data Analyses of Andesite Rock Blocks Aquifer with Varied Hydraulic Boundaries by Generalized Radial Flow Model **64**
Wen-Chieh Cheng and James -C. Ni

Constitutive Model of Soil-Structure Interface under Constant Stress Increment Ratio Stress Paths **72**
Ai-Zhao Zhou, Ting-Hao Lu, and Zhuang-Ping Gao

A Dynamic Damage Statistical Constitutive Model of Rock Considering Strain Rate under Uniaxial Loading Conditions **78**
Heng Zhao, Wen-Gui Cao, and Ling Zhang

The Application of PFWD in Sub-Grade Compactness Test **84**
Peng Wang and Chengchao Gua

Research on the Disturbed State Concept for Soft Clay Roadbed **92**
Xiao-Jun Yu and Jian-Yong Shi

Numerical Simulation of Soil-Pile Interaction in Expansive Soils Foundation 99
Chun-Shun Zhang, Yong-He Wang, Hong-Bin Xiao, and Zhen-Hui Fan

Indexes

Author Index..... 107

Subject Index..... 109

Grout Efficiency of Lifting Structure in Soft Clay

James -C. Ni[1] and Wen-Chieh Cheng[2]

[1]Associate Professor, Dep. of Civil Engineering, National Taipei University of Technology, 1, Sec. 3, Chung-hsiao E. Rd., Taipei, 10608, Taiwan; ckni@ntut.edu.tw
[2]Ph.D. Candidate, College of Engineering, National Taipei University of Technology, 1, Sec. 3, Chung-hsiao E. Rd., Taipei, 10608, Taiwan; s2428030@gmail.com

ABSTRACT: An inclined eight-story reinforced concrete building on a thick soft clay deposit was leveled by compensation grouting with short gel time grout injected through sleeved pipes. The monitoring system is used to record the injected grout volume, the mat foundation's heaved volume after grouting, and the mat foundation's settled volume during pore pressure dissipation. The grouting efficiencies improved from negative value to less than 1, and the stress histories of clay soils changed from normally consolidated to over-consolidated. A final compensation efficiency of 9.78% was achieved and the building was successfully leveled.

INTRODUCTION

Compensation grouting is a technique to offset subsidence caused during bored tunneling and underground excavation. The basic principle is to inject grout into the zone between the tunnel and overlying buildings to compensate for the ground loss and stress relief induced by underground excavation (Mair & Hight 1994). The compensation grouting operation is a series of grouting tubes known as a Tube A Manchette (TAM), radiating horizontally from a vertical shaft as shown in Figure 1. An electro-level beam embedded horizontally above the TAM is used to indicate when to start grouting and when to stop grouting, so that settlements are limited to specified amounts (Boone 1997). The low-viscosity particulate grouts intrude into the soil and introduce solids enabling the uplift displacement which contributes to the compensation effect of ground settlement associated with bored tunneling (Wongsaroj 2007). The major limitation is that the high mobility and low viscosity of the grout can cause difficulties in controlling grout locality. Grout with a quick set time can be used to partially solve this problem.

The effectiveness of compensation grouting can be evaluated by the amount of soil heave for a given injected grout volume (Soga 2004). Grouting efficiency, η, is defined as

the ratio of the soil heaved volume, V_E, to the injected volume of grout, V_{inj} .

$$Grouting\ efficiency,\ \eta = \frac{V_E}{V_{inj}} \quad (1)$$

The grout efficiency is usually smaller than 1 owing to loss of fluid from the grout bleeding, escape of the grout from the designated area by migration along fractures, and soil settlement due to the dissipation of positive excess pore pressures generated during grout injection. Komiya et al. (2001) conducted a field trial of shield tunneling in a deep soft clay deposit to investigate the long-term consolidation effect on grouting efficiency. A mixture of cement, water and water-glass with gel time of 20 seconds was used as the grout. The grouting program included tail void grouting operation immediately after the machine passage and grout jacking when the machine was approximately 5 meters ahead of the injection points. In both cases, the monitoring results show that the upward displacement owing to either grouting is negated by the consolidation settlement resulting in a net settlement. It is likely that the considerable consolidation of clay after grout injection is due to the dissipation of the excess pore pressures generated when the injected grout sheared the sensitive and compressible clay. This indicates that the grouting efficiency in soft clay may be negative.

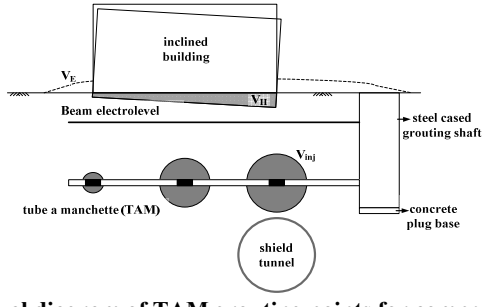


FIG. 1. Conceptual diagram of TAM grouting points for compensation grouting

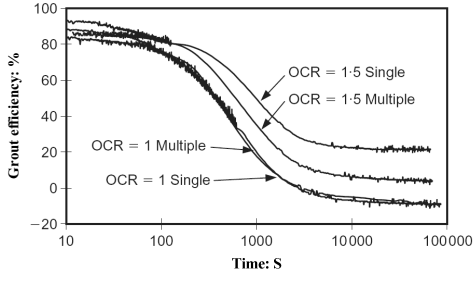


FIG. 2. Fracture grouting efficiency in OCR = 1 and 1.5 clay

From laboratory testing results, Au et al. (2003) found that the grout efficiency dramatically reduced to negative value with time for normally consolidated or lightly over-consolidated clays (see Figure 2) due to extensive shearing during the injection and the ultimate increase in mean effective pressure around the injection point caused by the injection pressure locked in when the grout solidified. However, for heavily over-consolidated clays, pore water migrated from the positive excess pore pressure zone around the injection point to the negative zone some distance away from the injection point during the consolidation stage. The compression near the injection point and swelling at some distance away from the injection point resulted in a negligible consolidation effect for heavily over-consolidated clays.

In addition to the efficiency loss discussed above, the efficiency of compensation grouting defined as the ratio of building settled volume to total injected grout volume may be further reduced by far-field geometry effects (i.e. the grout beneath the mat foundation can only contribute the effective lift of inclined building) as shown in Figure 1.

$$Compensation\ efficiency,\ \xi = \frac{V_H}{V_{inj}} \tag{2}$$

The efficiency of compensation grouting is a function of ground conditions, grout rheology, injection method and the building weight.

GEOLOGICAL CONDITION

The soil profile at the site consisted of miscellaneous urban fill, very soft silty clay, and thick deposit of soft silty clay as shown in Figure 3. Static groundwater levels in the vicinity of the grouting area were one meter below the surface. The eight-story reinforced concrete building with a one-story basement was inclined to the south at 1/200. The mat foundation of 32 meters by 18meters is 3.85 meters below the surface. Concrete piles of 0.35 meters in diameter and 9 meters in length were used as retaining wall during basement excavation.

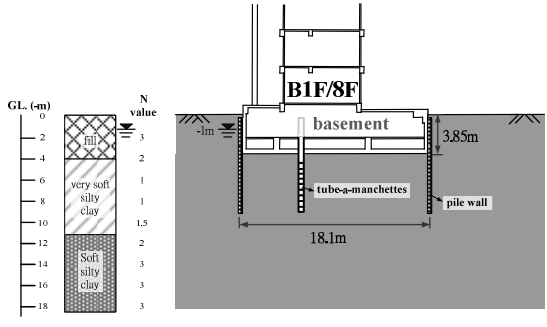


FIG. 3. Subsurface profile, basement and injection pipe

GROUTING DESIGN

The thick soft clay deposit rules out other grouting methods other than fracture grouting. To conduct the repetitive grouting procedure, a series of grouting tubes (TAM) were installed five meters beyond the mat foundation. The grout hole spacing was two meters on center. Drill casings were one meter in length, and were drilled through reinforced concrete floor in the mat foundation with small equipment for grout casing insertion. Water was used as the flush medium.

Because of cost consideration, the common grouting pumps were used. To improve the compensation efficiency, the grout hose system of 1.5 shots and quick set grout were adopted to limit the travel of grout. Two stages of grout mixes were used. The first stage grout mix is given in Table 1 and was used to stabilize the clays between five to nine meters below ground level and provide the reaction for the next lifting stage. The second stage grout mix is given in Table 2 was used to grout the clays between four to six meters below ground level and lift the building.

Table 1. Grout mixes used for foundation stabilization (gel time 20~25 seconds)

A liquid				B liquid	
Cement	Pulverized Coal	CaO	Water	Na_2O-3SiO_2	Water
400kg	300kg	90kg	250L	150L	350L
500L				500L	
1000L					

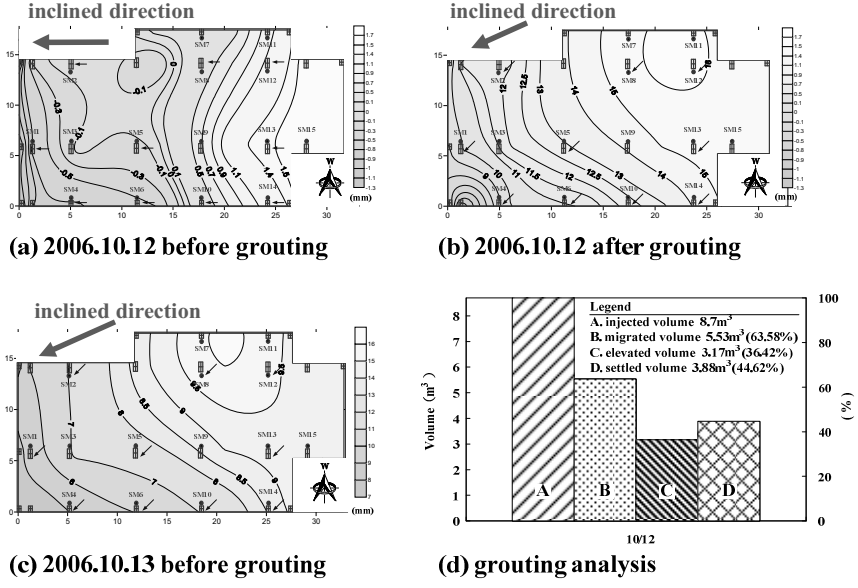
Table 2. Grout mixes used for lift grouting (gel time 15~20 seconds)

A liquid				B liquid	
Cement	Pulverized Coal	CaO	Water	Na_2O-3SiO_2	Water
400kg	300kg	90kg	325L	250L	250L
500L				500L	
1000L					

MONITORING SYSTEM AND GROUTING PERFORMANCE

The elevations of building columns in the basement were monitored before and after each day's grouting program. The difference of contour lines between pre-grouting and post-grouting provides the elevated volume of the inclined building. Also the difference of contour lines between post-grouting and pre-grouting provides the settled volume due to the dissipation of excess pore pressure from the grouting. Figure 4 shows that the overnight settlement of 3.88 m^3 is more than the elevated volume of 3.17 m^3 at day one.

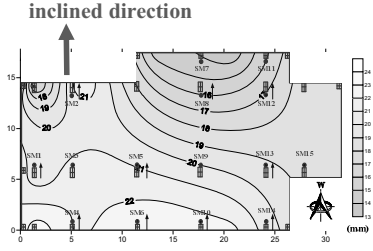
This indicates that the compensation efficiency is negative initially. However, the normally consolidated clay was gradually changed to lightly over-consolidated clay due to repetitive grouting, and this explained why the overnight settlement of 0.43 m^3 is less than the elevated volume of 3.86 m^3 at day four as shown in Figure 5(d). The compensation efficiency is gradually improved to a positive value. To understand how long it takes for the excess pore pressure to dissipate, the injection was suspended for seven days after the fourth day of grouting. The results are shown in Figure 5(f). It takes five days to reach the final accumulative settlement of 3.82 m^3 which is near the elevated volume of 3.86 m^3 at day four. Figure 6 shows that the accumulative elevated volume surpasses the accumulative settled volume from day four. From day four on, the elevated volume is larger than the settled volume for every grouting day. This indicates that the higher the over-consolidation ratio, the better the grouting efficiency. To reduce the differential settlement of the eight-story building on very soft clay, the final compensation efficiency of 9.78 % is obtained by subtracting final settled volume of 6.68% from the final elevated volume of 14.36% as shown in Figure 7. The higher the over-consolidation ratio, the less the compressibility, and the better the compensation efficiency. Since the sandy soils are a lot less compressible than clayey soils, it is logical to assume that a sand deposit provides better compensation efficiency than a clay deposit.



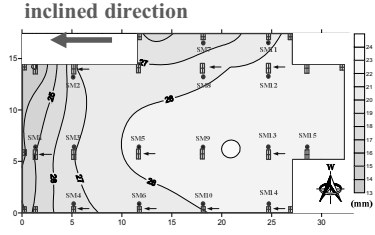
(a) 2006.10.12 before grouting **(b) 2006.10.12 after grouting**

(c) 2006.10.13 before grouting **(d) grouting analysis**

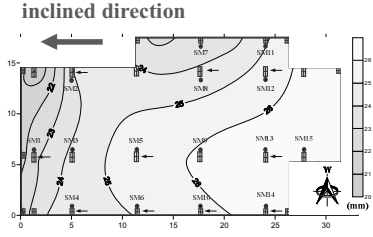
FIG. 4. Grouting results of day one



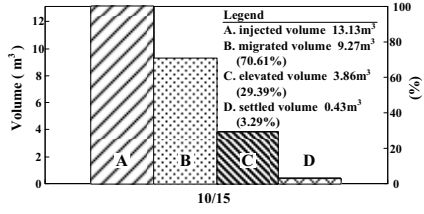
(a) 2006.10.15 before grouting



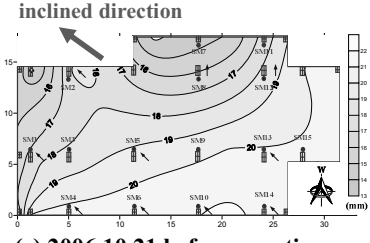
(b) 2006.10.15 after grouting



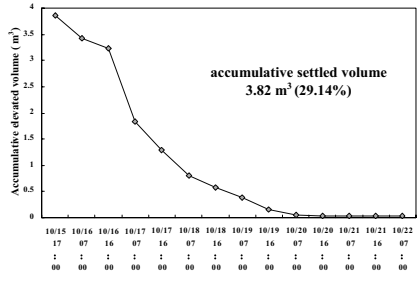
(c) 2006.10.16 before grouting



(d) grouting results of 2006.10.15



(e) 2006.10.21 before grouting



(f) settlement due to dissipation of pore pressure

FIG. 5. Grouting results of day four through day ten

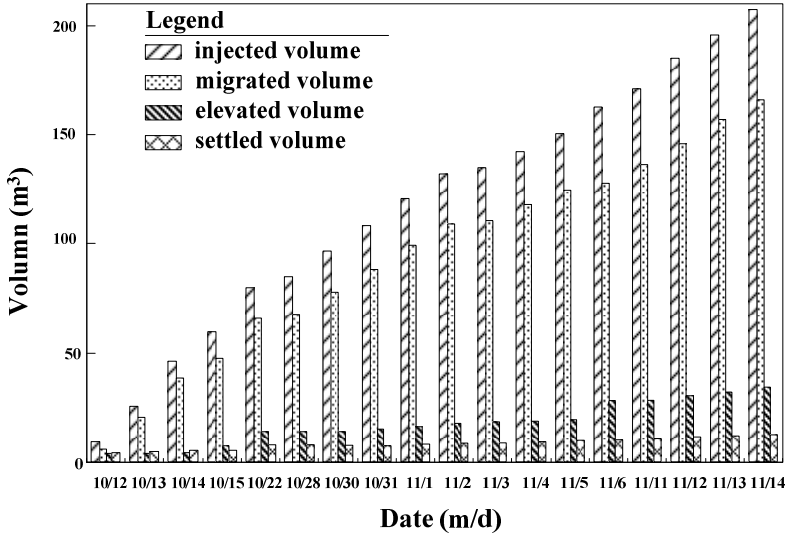


FIG. 6. Bar chart of accumulative injected, migrated, elevated and settled volume

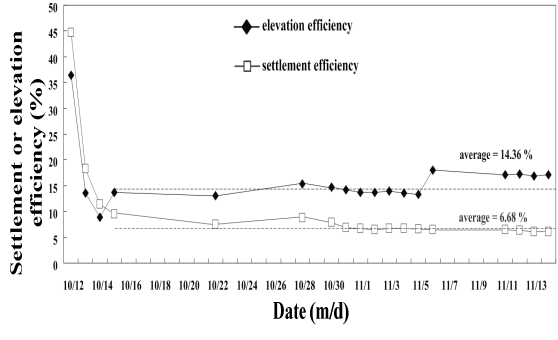


FIG. 7. The variation of elevation and settlement efficiency

CONCLUSIONS

1) Compensation fracture grouting can be used successfully to level an inclined eight-story reinforced concrete building on the thick soft clay deposit with a final compensation efficiency of 9.78%. 2) Field investigations verify that grouting efficiency can be improved from a negative value to less than one by repetitive fracture grouting with a short gel time grout. This study shares the same conclusions from other researchers in the laboratory testing and in the shield tunneling areas of research.

REFERENCES

Au, S.K.A., Soga, K., Jafari, M.R., Bolton, M.D., & Komiya, K. (2003). "Factors affecting long-term efficiency of compensation grouting in clays." *Journal of Geotechnical and Geoenvironmental Engineering*, 129(3): 254–262.

Boone, S., Heenan, D., & Pennington, B. (1997). "Monitoring systems for control of compensation grouting." *Geotechnical Special Publication*, 66: 101–117.

Komiya, K., Soga, K., Akagi, H., Jafari, M.R., & Bolton, M.D. (2001). "Soil consolidation associated with grouting during shield tunneling in soft clayey ground." *Geotechnique*, 51(10): 835–846.

Mair, R. J., & Hight, D. W. (1994). "Compensation grouting." *World Tunnelling*, November, 361–367.

Soga, K., Au, S.K.A., Jafari, M.R., & Bolton, M.D. (2004). "Laboratory investigation of multiple grout injections into clay." *Geotechnique,* 54(2): 81–90.

Wongsaroj, J., Soga, K., & Main, R.J. (2007). "Modelling of long-term ground response to tunneling under St. James's Park, London." *Geotechnique*, 57(1): 75–90.

Modeling Resilient Modulus of Unbound Granular Materials under Repeated Loading

Cheng Chen[1,2], Louis Ge[3], A.M. ASCE, and Jia Sheng Zhang[2]

[1]Xiang Tan University, College of Civil Engineering and Mechanics, Xiangtan, China. E-mail: chencheng401@sina.com
[2]Central South University, School of Civil Engineering and Architecture, Changsha, China.
[3]Missouri University of Science and Technology, Department of Civil, Architectural, and Environmental Engineering, 1401 N Pine Street, Rolla, MO 65409; PH (573) 341-7193; FAX (573) 341-4729; E-mail: geyun@mst.edu

ABSTRACT: Resilient modulus of unbound granular materials is a key design parameter for mechanistic empirical pavement design. But the complexity of the affected factors has made it challenging and difficult for practical designers and researchers to find an appropriate model to describe the entire stress-strain response where the plastic deformation is accumulated during the repeated loading condition. A cyclic plasticity model based on fuzzy sets plasticity theory is presented in this paper to model the resilient modulus and permanent strain behavior of unbound granular materials under repeated loading. The concept of the fuzzy set plasticity is first introduced, followed by its model formulation and numerical simulation. The model was calibrated against a resilient modulus testing data of a typical Missouri soil. The numerical results showed that the fuzzy set model is capable of mimicking and simulating the resilient and permanent responses of unbound granular materials under repeated loading.

INTRODUCTION

Pavement design is a process intended to find the most economical methods for the pavement, taking into account the properties of the soil foundation and the traffic to be carried during the service life of the road. And resilient modulus of unbound granular materials is a key parameter for mechanistic empirical pavement design. With the laboratory resilient modulus testing data, many computational modeling, which correlate the resilient modulus to different confining pressure and deviator stress, can be calibrated (Werkmeister et al., 2004). However, the complexity of the affected factors has made it challenging and difficult for practical designer and

researchers to find an appropriate model to describe the entire stress-strain response where the plastic deformation is accumulated during the repeated loading condition. And the disadvantages of traditional design have become more obvious during the last decades as a consequence of the growth of transportation needs and the urge for using recycled materials. So developing reliable and versatile constitutive models to describe the appropriate characterization of the unbound granular materials has been challenging tasks. Over the years, many constitutive models have been proposed and developed, which employ analytical methods focusing on the realistic stress-strain behaviors of unbound granular materials under repeated load cycles including the resilient behavior, plastic response and permanent deformation based on theory of plasticity (e.g. Lekarp, 1997; Jacobsson, 1998; Frost et al., 2004; Garcia-Rojo and Herrmann, 2005). In the mean time, the selection of the most appropriate material model has been used in the analytical design of the pavement.

A cyclic plasticity model based on fuzzy sets plasticity theory is presented in this paper to model the resilient modulus and shakedown behavior of unbound granular materials under repeated loading. The concept of the fuzzy set plasticity is first introduced, followed by its model formulation. The model developed here is capable of simulating realistic stress-strain behaviors of unbound granular materials under repeated load cycles including nonlinear dilatancy behavior, material memory, accurate reverse loading feature, non-proportional loading, and long-term cyclic effects. The resilient modulus calculated from each load cycle is recorded and calibrated through a set of common Missouri subgrade soils and unbound granular base materials in accordance with the AASHTO T 307 test method.

MODEL FORMULATION

As previously mentioned, many elastoplastic constitutive models, normally with a great number of constants and parameters, have been developed to describe the complex behavior of the granular materials. The determination of these parameters naturally requires more extensive laboratory test data and site investigation plans compared to what simpler models need. Nevertheless, the stress-strain state of the pavement structure can be modeled more realistically using the advanced models. With that in mind, we intend to assess whether the fuzzy set plasticity model can mimic more realistic stress-strain behavior of granular material under repeated loading.

The original fuzzy set plasticity model consists of deviatoric and locking fuzzy surfaces to account for material responses under purely deviatoric shearing and isotropic compression/extension condition. In this study, the model has been simplified and only deviatoric component of the original fuzzy set model was used for the simulation. Further and detailed information about fuzzy set plasticity can be found at Ge and Sture (2008).

The fuzzy surface in compression is expressed as $F_c = r - a_0 - a_1 p = 0$ which represents a three-stress-invariant yield surface. p is the mean stress and is one third of first stress invariant I_1. r is the multiplication of q and g, where q is defined in a way similar to second deviatoric stress invariant J_2, and g is the Willam-Warnke function (Willam and Warnke, 1974). For proportion loading, g is 1, so that $r = q$.

At each stress state, the value of the membership function γ will be explicitly defined and the plastic modulus on the loading surfaces can be found at Ge and Sture (2008), which is given as follows.

$$H = \frac{M\gamma^d}{1-\gamma^{d+1}}$$

where M and d are model parameters, is the plastic modulus. Although the value of γ is 1 at fully elastic state and 0 at the fully plastic state, the assignment of the value in elastoplastic state is deterministic and can be arbitrarily defined as needed. A linear variation with respect to stress state was adopted in this study.
A classical flow rule incorporating current stress state η and state parameter ψ is used (Been and Jefferies, 1985).

$$\frac{\partial \varepsilon_v^p}{\partial \varepsilon_d^p} = A[M_c(1+\kappa_d\psi)-\eta]$$

where A and κ_d are model parameter and M_c is the stress ratio q/p at critical state condition and is identical to the model parameter a_l. ψ=0. η is the current stress ratio q/p.

The resilient behavior is often expressed in terms of the resilient modulus $M_r = \frac{\Delta(\sigma_1-\sigma_3)}{\varepsilon_a}$, Δ indicate "change in", and σ_1, σ_2, and ε_a, = major and minor principal stress and recoverable axial strain, respectively. And regarding the combined effects of stress level and test material density, the shear modulus values have been used (Iwasaki and Tatsuoka, 1977).

$$G = G_0\left(\frac{p}{p_0}\right)^m$$

where G_0 and p_0 are initial shear modulus and mean stress. m is a stress exponent depending on the shear strain level.

Since modeling the resilient modulus of unbound granular material under repeated loading is the main task of this research, laboratory test on loose sandy soils and unbound granular base materials were used for model calibration and verification purposes.

RESULTS AND DISCUSSION

Table 1 lists the model parameters that were used in the fuzzy set plasticity model, which was calibrated against the resilient modulus testing data on a Missouri subgrade soils (Petry et al., 2008). The stress paths for the investigation of the resilient modulus due to sequences of varied amplitude loading are presented on the p-q stress space shown in Figure 1. All loading procedures are limited to pulse series where the confining pressure remains constant, as can be seen from the slopes of the stress paths. The confining pressure for these stress paths O_1- A_1- B_1- C_1- D_1- E_1, O_2-

A_2- B_2- C_2- D_2- E_2, and O_3- A_3- B_3- C_3- D_3- E_3 are selected as 2 psi, 4 psi, and 6 psi, respectively. The initial void ratios were reported 0.41. Fig. 2 shows the resilient modulus versus deviator stress response while Fig. 3 presents the permanent axial strain versus number of cycles.

Table 1. Model parameters used in the simulation

K	G_0	M	d	$\kappa_d\psi$	a_0	a_1	m	A
5800	4809	2520	0.98	0	10.57	1.03	0.54	0.071

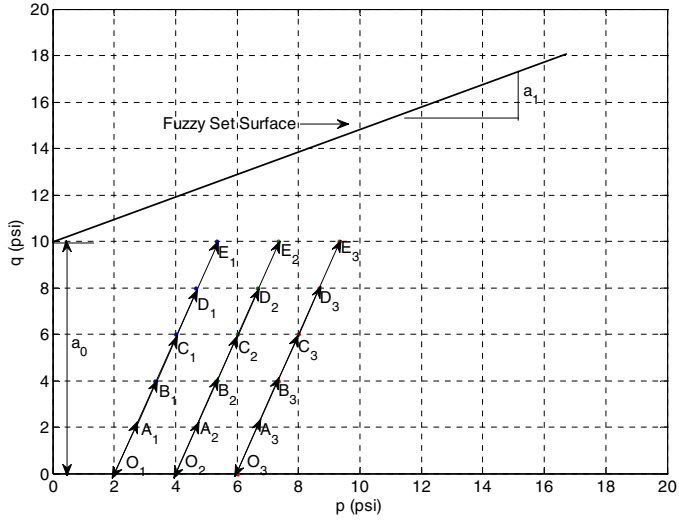


FIG. 1. Stress paths for varied amplitude loading.

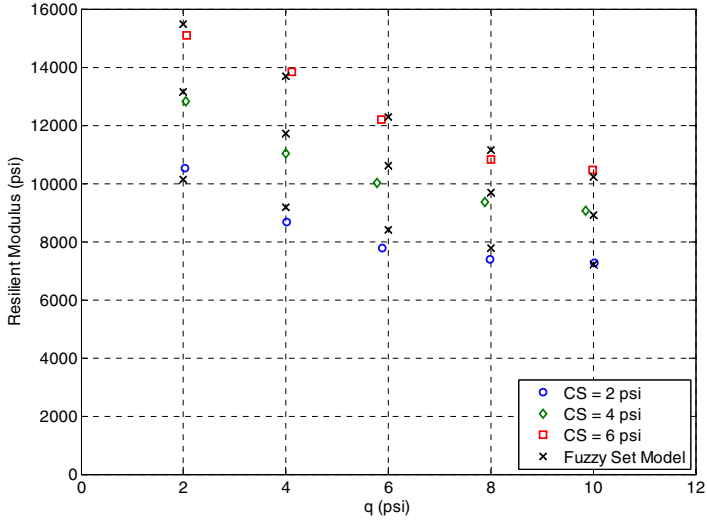


FIG. 2. Resilient modulus vs. deviator stress.

In Fig. 2, the fuzzy set model shows a good match against the three stress paths. It is seen that the resilient modulus increases after the confining pressure p increased. And it is also shown that the resilient modulus decreases when the deviator stress is increased. The results in Fig. 3 show that, after a number of cycles at each stress level, the rate of accumulation of permanent strain is decaying towards a zero rate. An increase of applied deviator stress results in more permanent axial strain.

CONCLUSIONS

A simplified fuzzy set plasticity model was developed and its capability and performance was assessed through one of the AASHTO T 307 tests on common Missouri subgrade soils and unbound granular base materials. After comparing with these test data, the simplified fuzzy set plasticity model perform fairly well in modeling resilient modulus of unbound granular materials under repeating loading. More work need to be done to fully assess the resilient and permanent deformation behaviors of unbound granular materials under complex loading/unloading conditions. The fuzzy set plasticity model can be verified against more factors affecting the resilient response, such as: stress level, density, particle size, stress history, number of load cycles.

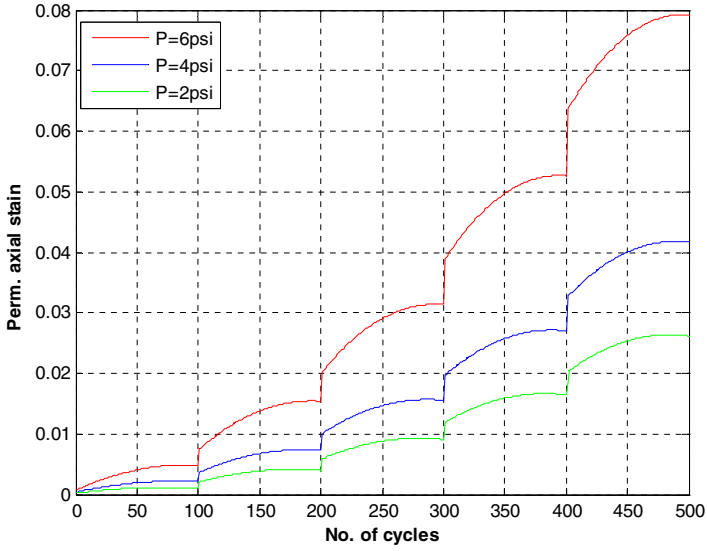


FIG. 3. Permanent axial strain vs. Number of loading cycles.

ACKNOWLEDGMENTS

This study was financially supported by the Fund of China Scholarship Council ([2007]3020) and the Scientific Research Fund of Hunan Provincial Educational Department (06C832).

REFERENCES

Been, K., and Jefferies, M. G. (1985). "A state parameter for sands." *Géotechnique,* 35(1): 99-112.

Frost, M.W., Fleming, P.R., and Rogers, C.D.F. (2004). "Cyclic triaxial tests on clay subgrades for analytical pavement design." *Journal of Transportation Engineering*, ASCE, 130(3), 378-386.

Garcia-Rojo, R., and Herrmann, H.J. (2005). "Shakedown of unbound granular material." *Granular Matter*, 7, 109-118.

Ge, L., and Sture, S. (2008). "Cyclic plasticity constitutive model for granular materials." *Computers and Geotechnics* (under review).

Iwasaki, T., and Tatsuoka, F. (1977). "Effects of grain size and grading on dynamic shear moduli of sands". *Soils and Foundations*. 17(3): 19-35.

Jacobsson, L. (1998). "Review of research on railway ballast behavior – Experimental findings and constitutive models." Chalmers University of Technology, Sweden, 1998.

Lekarp, F. (1997). “Permanent deformation behaviour of unbound granular meterials.” Licentiate thesis, Department of Infrastructure and Planning, KTH, Sweden, 1997.

Petry, T.M., Richardson, D.N., Ge, L., Han, Y.-P., and Lusher, S.M. (2008). Resilient Moduli of Typical Missouri Soils and Unbound Granular Base Materials, report #RI06-001, Missouri Department of Transportation.

Werkmeister, S., Dawson, A.R., and Wellner, F. (2004). “Pavement design model for unbound granular materials.” *Journal of Transportation Engineering*, ASCE, 130(5), 665-674.

Willam, K. J., and Warnke, E. P. (1974). “Constitutive model for the triaxial behavior of concrete.” In: *Seminar on Concrete Structures Subjected to Triaxial Stress,* ISMES, Bergamo, Italy, 1974.

Study on the Deformation and Evolution Mechanism of Soil-Rock-Mixture Slope under Excavation Disturbance

Zhong Zhou[1], Ru-Song Nie, Bao-Chen Liu, Xiao-Li Yang

[1]School of Civil Engineering and Architecture, Central-South University, Changsha, Hunan 410075, China; PhD; zhongzhou78@yahoo.com.cn

ABSTRACT: In recent years, with the construction of the freeways, large-scale hydro projects and deep foundation pit projects, project accidents aroused by people's excavation are more and more outstanding, especially in the western of China, which surface is most covered by soil-rock-mixture slope, the human project activity has already become the main induced factor of the geologic hazard. Based on in-situ simulation experiment of excavation and 3D finite element method numerical simulation, the deformation and evolution mechanism of soil-rock-mixture landslide under excavation disturbance was studied. The study results show that stability and displacement field of soil-rock-mixture slope are obviously influenced by excavating effect, and most of soil-rock-mixture landslides caused by excavation are shallow draught slope failures.

INTRODUCTION

Soil-rock-mixture is one kind of natural substance formed in geological history. It behaves between soil mass and rock mass, which has the inherent unique properties of inhomogeneity, discontinuity and difficult to gather sample. The body of soil-rock-mixture slope is composed of soil-rock-mixture medium, widely spread in the area of China as well as all over the world. This kind of landslides often bring about a serious harm and gigantic property loses to national economic construction, the people regular and safe life due to it's larger landslide scale, numerous influencing factors, paroxysmal landside, complicate slippage conditions. Therefore, there have peculiar theory and practical value to carry out systems analysis and study on this kind of landslides.

In recent years, with the construction of expressway, large-scale hydraulic engineering and new foundation trench excavating project, the engineering accidents caused by man-made slope-cutting and excavation have been highlighted. Especially in the coverage area of earth-rock aggregate slope, the engineering activities of human beings have become the main inducing factors of geologic hazards. For instance, from 1989 to 2000, 1298 places had large-scale or serious paroxysmal geologic hazard occurred with large loss. 772 of these hazards were landslides, and

119 of them were collapses. 543 landslides and 79 collapses were caused by slope-cutting and excavation, which respectively occupied 70.3% and 66.4% of the total. At present, the stability of lower slope during slope-cutting and excavation has aroused the concern of scholars at home and abroad. However, the research on the moving law of lower slope under the disturbance of excavation has not been mature enough. Therefore, it has special theoretical and practical values to do a deep research on the distortion theory of earth-rock aggregate slope under the disturbance of excavation.

This paper aims at the study on the formation and evolution mechanism of earth-rock aggregate slope under the influence of step-by-step excavation through the on-site excavation simulation test and three-dimensional finite element numerical simulation test so as to provide technical and theoretical supports for a better understanding and prevention of such landslides in future.

ON-SITE EXCAVATION SIMULATION TEST

Test Design

Choose the typical earth-rock aggregate slope at the exit of Qinglong Tunnel in Guizhou section of Shanghai-Ruili Expressway to make on-site excavation test and comprehensive monitoring to its original position and research the forming conditions, deformation and displacement features and destruction and slide laws of earth-rock aggregate slope under the disturbance of excavation. Refer to the literature for the landform, topography, engineering geology, hydrological and geological conditions, soil properties and floor plan of monitoring spot. Measure and read the slope cracks by steel tape, and observe the deep displacement by inclinometer. There are 6 inclinometer holes in the test area, both of them with a depth of 11m.

Excavation Sequence

After setting up the monitoring spot of the inclinometer and surface displacement, put it still there for about a week so that the inclinometer can achieve a balance with the surrounding soil. In consideration of the dangers of man-made excavation, excavators have been adopted for this test. The excavation sequence is as shown in Figure 1. Excavate from soil layer 1 to 4, with an excavation depth of 2m for each layer, one layer per day until the collapse of the slope. On April 16, 2005, the first excavation was carried out and the excavation period is 13:30-14:00 daily. The monitoring frequency is four times per day, and the measuring and reading time is respectively at 4:00,10: 00,16:00 and 22:00 daily.

Analysis of Test Achievements

Choose the monitoring data at 16:00 per day as the displacement value of the slope after the excavation of this soil layer. Settle and analyze the inclinometer data of each hole, and then draft them into figures. Figure 2 is the functional curve between the displacement and depth of inclinometer hole ZK1 - ZK3 in L1 section under the effect of step-by-step excavation. It can be seen from Figure 2: With the increasing depth of excavation, the sliding displacement of the slope increases gradually; the displacement deformation zone basically takes place within 0-4m

under the ground. The displacement decreases along with the increasing depth, and the slope surface bears the largest deformation. Each monitoring hole has a clear position of sliding surface, and the positions of sliding surfaces at ZK1-ZK3 monitored by this test are respectively at 3.5m, 3.5m and 4m.

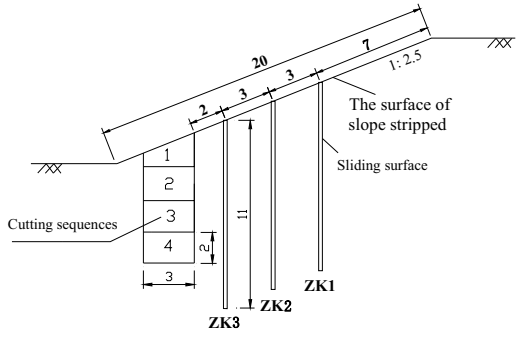


FIG. 1 Cutting sequences (m)

Figure 3 is the functional curve between the horizontal displacement and excavation depth of ZK1 along with the time. The following phenomena can be seen. With the increasing excavation depth, the horizontal displacement increases gradually; the deformation of earth-rock aggregate slope disturbed by excavation is relaxation deformation, which decreases downward from the slope surface. The displacement at 0.5m is basically equivalent to 2 times of that at 2.5m; however, there is hardly displacement at 5m. The minor changes in value are only caused by measurement errors.

The position of the sliding surface can be determined through combining the position of the sliding surface monitored by inclinometer and the cracks at the anterior and posterior borders of the landslide. The position and shape of L1 sliding surface are shown in Figure 4. It can be seen from Figure 4: The sliding surface of earth-rock aggregate slope is very shallow, with a depth of within 3-4m under the ground, and this belongs to shallow landslide; the slope shape of the sliding deformation zone approximates a hemicycle, and the three-dimensional shape of it approximates 1/4 spheroid. Under the known shape of sliding surface, soil density, cohesion C and angle of internal friction φ in sliding zone, on the basis of method of slices from limit equilibrium, the stability factors of L1 and L2 sections have been calculated, and they are respectively 1.04 and 1.02. They are located at the critical point of sliding instability and belong to instable slope. They are prone to slide under the influence of excavation or rainfall infiltration. In the afternoon of April 20, the inclinometer monitoring was stopped, with no longer color strip cloth covering the test zone. On April 23 and 24, there was heavy rain continuously at test spot. On April 25, the slope collapsed. As a result, the excavation groove at the anterior border of the landslide was buried, and the inclinometer pipe was broken, as shown in Photo 1.

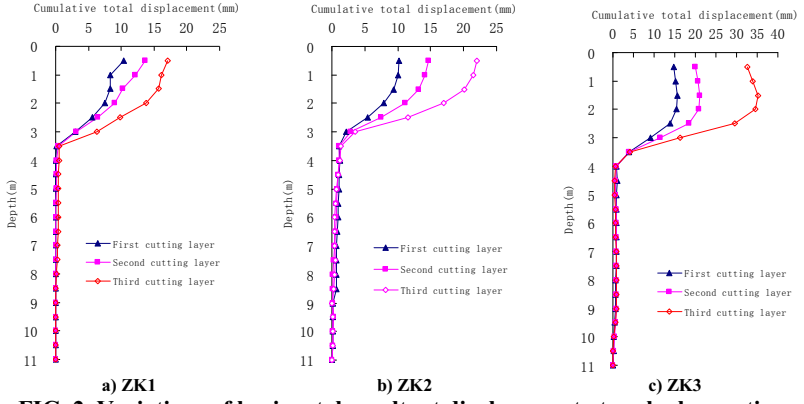


FIG. 2 Variations of horizontal resultant displacement at each observation point under excavation disturbance in field test

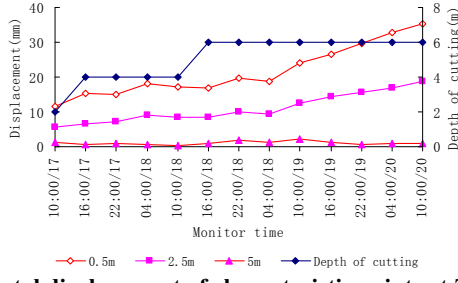


FIG. 3 Horizontal displacement of characteristic points at ZK1 and its cut depth

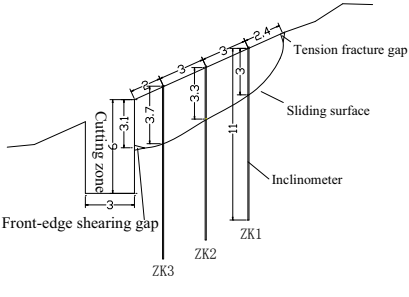


FIG.4 The shape of sliding surface at profile L1 (m)



Photo 1 The slope after landslide

THREE-DIMENSIONAL NUMERICAL SIMULATION TEST

Establishment of Finite Element Mode

Through long-term geologic process, the natural slope is in a relative stability state. However, the excavation breaks the relative balance state and causes the unloading rebound deformation of the slope towards the free face, and the increasing deformation will result in landslide. The process of road cutting excavation is actually a process of unloading for slope rock mass gradually. This paper uses the element birth and death of finite element to simulate the process of road cutting excavation. Firstly, determine the initial stress and displacement field of the whole slope. Then, kill the elements of excavation parts stage by stage in order to determine the stress and displacement field after excavation. Finally, determine the stress and displacement values caused by excavation through post processing.

Figure 5 is the finite element network of numerical model, the size and detailed dimension of which have been marked. X-direction is the longitudinal direction of excavation, with a width of 20m. Y-direction is the down the slope, with a length of 36m. Z-direction is the vertical direction, with a height of 24m. An octahedral unit with 20 nodes is adopted, with 2,220 elements and 10,431 nodes in total. The four flanks of the model limits the displacement in X-direction and Y-direction, and the bottom face limits the displacement in X-direction, Y-direction and Z-direction of all. The slope is free surface. Study the sliding and evolving law of the model under the effect of gravity during the process of step-by-step excavation. Table 1 shows the property indices of the earth-rock aggregate slope in physical mechanics.

Table 1 The Parameters of The Soil Layers

Types of stratum	Elastic modulus (Mpa)	Poisson's ratio	Density (kN/m^3)	Cohesion (kPa)	Angle of internal friction (°)	Angle of dilatancy (°)
Soil-rock-mixture	10	0.364	17.3	15	25.5	5
Muddy siltstone	2632.5	0.219	25	200	28	3

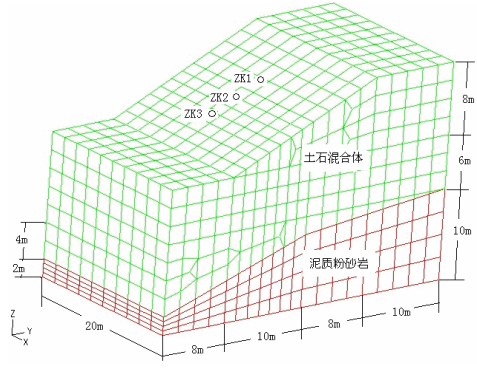


FIG. 5 The finite element model of the slope (m)

Analysis of Simulation Result

According to the test excavation sequence shown in Figure 1, gradually excavate the slope of the road cutting. In the analysis of numerical simulation, the horizontal displacement down the slope along the monitoring line ZK1-ZK3 while gradually excavating is shown in Figure 6. The analytic result of finite element numerical simulation shows that the displacements ZK1, ZK2 and ZK3 down the slope increase gradually along with the depth of excavation. Especially, while excavating layer 2-3, namely, while the slope becomes from stability to instability, the displacement of the slope body increases obviously. The horizontal displacement near to excavation profile is larger than that far away it. The position of sliding face is about 4m under the slope surface, and it approximates the on-site measured distance of 3.5~4m from the sliding face to the ground.

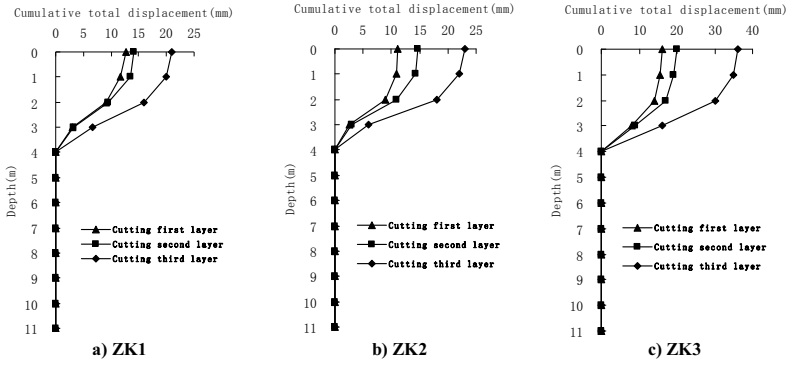
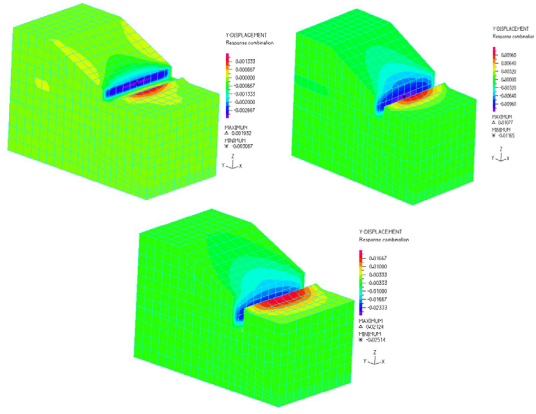


FIG. 6 Variations of horizontal displacement at each observation point under excavation disturbance using FEM

Figure 7 shows the horizontal displacement of the slope under the influence of step-by-step excavation. It is seen that the deeper the excavation is, the greater the free face is; due to the self-weight stress, the distortion of the upper covering slope becomes greater; the landslide zone becomes increasingly obvious. The shape of landslide zone approximates that of landslide zone observed on the actual slope.

Figure 8 shows the plastic strain vector after the completion of excavation. There is a clear plastic zone on the slope. Thus, the slope is in a critical stability state, once induced by external factors, it is possible to cause destruction. Plastic zone mainly distributes in a hemispheric zone over the free face and within 4m under the slope. The plastic zone focuses on the slope toe at about 4m under the slope, which is just the position of sliding face shown by on-site monitoring achievements. Plastic strain is along the Y obliquely down the slope and then gradually points horizontally to the outside of the slope.



a) Cutting first layer b) Cutting second layer c) Cutting third layer

FIG. 7 The horizontal displacement of soil-rock-mixture slope under step by step excavation (m)

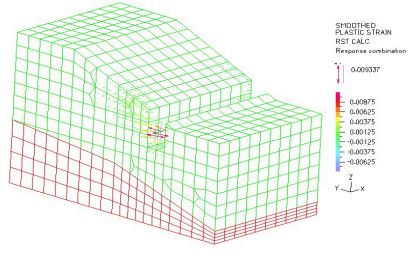


FIG. 8 The displacement vector of plastic strain

CONCLUSIONS

1) On-site excavation simulation test and three-dimensional finite element simulative calculation shows that the displacement field and stability of earth-rock aggregate slope have been impacted obviously by excavation effect, most results of which are shallow traction destruction.

2) The deformation and evolution features of earth-rock aggregate slope under the influence of disturbance in the excavation: sliding bed is 3-4m under the slope, sliding deformation zone is within 0-4m under the slope surface and as approximate as 1/4 spherical. The greatest deformation is the slope, and the deformation gradually decreases from its surface to its deep part. As to the displacement on the same profile, the nearer it is to the free face, the greater the displacement is.

3) Through a comparative analysis between the numerical simulation results and on-site monitoring achievements about the deformation of earth-rock aggregate slope

under the influence of step-by-step excavation, we find that these two are greatly consistent not only in the shape and position of landslide zone but also in the sliding displacement and have played important roles in mutual verification.

ACKNOWLEDGMENTS

The authors appreciate the support of the National Science Foundation of China.

REFERENCES

Zhou Zhong, Fu He-lin, Liu Bao-chen, et. (2006). "Experimental Study of the Permeability of Soil-Rock-Mixture." *J. Journal of Hunan University* (Natural Sciences), Vol. 33(6): 25-28. (in Chinese)

Sun Guang-zhong，Yao Bao-kui. (1988). "Chinese Typical Slope." *M. Beijing：Science Press*, VA: 1-12.(in Chinese)

Zhou Zhong. (2006). "Study on the fluid-soild coupling characteristic of soil-rock-mixture landslide and its prediction and forecast ." *D. Changsha: Central South University*. VA: 1-6.(in Chinese)

Wang Qun，Yang Shun-quan，Wei Jun-cai etc. (2002). "Present situation and control counter measure of geological hazards induced by human activity in Hunan province." *J. The Chinese Journal of Geological Hazard and Contral*, Vol. 13(2): 56-62. (in Chinese)

S. Kwon, J. W. Wilson. (1999). "Deformation mechanism of the underground excavations at the WIPP site." *J. Rock Mechanics and Rock Engineering*, Vol. 32(2): 101-122.

Mancheol Suh, Min-Ho Koo, Suck-Won Choi etc. (2004). Instability of an underground ancient tomb due to excavation and its relationship to the temperature and ground water." *J. Geotechnical and Geological Engineering*，Vol. 22(2)：269-283.

D. F. Malan. (2002). "Manuel Rocha Medal Recipient Simulating the Time-dependent Behaviour of excavations in Hard Rock." *J. Rock Mechanics and Rock Engineering*, Vol. 35(4): 225-254.

Zhou Zhong, Fu He-lin, Liu Bao-chen, et. (2006). "Study on In-situ Monitoring of Cut tests on a Well-instrumented Colluvial Slope." *J. Chinese Journal of Rock Mechanics and Engineering*, Vol. 25(10): 2065-2070. (in Chinese)

Deng Qin，Li Jiang-lin，Zhang Zhi-gang. (2006). "Elementary Introduction on Research and Development of Unloading Rock Mass Mechanics." *J. Journal of Heilongjiang Hydraulic Engineering College*, Vol. 33(2): 27-29. (in Chinese)

Development and Application of Constitutive Model for Simulation of Mechanical Behavior of Granular Material

Xueyan Liu[1], A. Scarpas, C. Kasbergen, and W.X. Zhang[2]

[1]Section of Structural Mechanics, Faculty of Civil Engineering and Geosciences, Delft University of Technology, Stevinweg 1, 2628 CN Delft, The Netherlands, x.liu@tudelft.nl
[2]College of Resources and Civil Engineering, Northeastern University, China.

ABSTRACT: In this contribution, on the basis of micropolar (Cosserat) continua approach, a constitutive model for simulation of granular material (e.g. sand) response in the elastoplastic range has been presented. Numerical analyses on strain localization in single and two phase materials are carried out in the last part of this contribution. The influence of the additional micropolar parameters and solid-fluid interactions on the formation of strain localization is investigated.

INTRODUCTION

The analysis of strain localization is of importance in engineering practice because localization is a precursor to sudden failure. Numerical simulations of strain localization by means of the finite element method are known to lead to mesh sensitivity when the classical continuum models without enrichment are considered. In order to obtain a meaningful representation of the continuum response in the presence of strain localization, much effort has been devoted in recent years to devise regularization strategies which are able to both, simulate the development of shear band independent of the finite element mesh and, retain the nature of the governing equations. In the micropolar continuum approach, the constitutive formulations offer the possibility of simulating correctly the behaviour and the characteristics of shear bands in granular materials by introducing an internal length into the solution of the initial value problem. Although there is a wide interest in micropolar continuum theories, a critical perusal of the literature reveals that the necessary internal length scale parameters are often arbitrarily chosen with constant values. However, it is observed that the internal scales need to change to accommodate the possible variation in the contact surface between the particles.

In this contribution, the generalized numerical formulations for the case of a 3D elasto-plastic micropolar continuum have been developed. The evolution of the micropolar parameters has been defined on the basis of the cumulative effective plastic strain and particle characteristics. Numerical analyses show that due to the presence of an internal length scale changing in magnitude during the deformation of the material,

mesh independence can be ensured.

3D MICROPOLAR CONTINUUM FORMULATION

The formulation developed by de Borst (1991) for the case of 2D micropolar continua is herein extended to 3D micropolar continua. The nine stress components are denoted by $\tilde{\boldsymbol{\sigma}}$ and the nine couple-stresses by $\tilde{\mathbf{m}}$. Similarly, the nine strain components by $\tilde{\boldsymbol{\varepsilon}}$ and the nine micro-curvatures by $\tilde{\boldsymbol{\kappa}}$.

On the basis of these, vector of generalized stress is defined as $\boldsymbol{\sigma} = [\tilde{\sigma}, \quad \tilde{\mathbf{m}}]$ and a vector of generalized strain as $\boldsymbol{\varepsilon} = [\tilde{\varepsilon}, \quad \tilde{\kappa}]$. The elastic relation between stress and strain is defined as $\boldsymbol{\sigma} = \mathbf{D}^e \boldsymbol{\varepsilon}$ with:

$$\begin{aligned}
&\mathbf{D}^e = \mathrm{diag}\left[\mathbf{D}_1, \quad \mathbf{D}_2, \quad \mathbf{D}_2, \quad \mathbf{D}_2, \quad \mathbf{D}_3,\right], \\
&\mathbf{D}_1 = \begin{bmatrix} 2\mu c_1 & 2\mu c_2 & 2\mu c_2 \\ 2\mu c_2 & 2\mu c_1 & 2\mu c_2 \\ 2\mu c_2 & 2\mu c_2 & 2\mu c_1 \end{bmatrix}, \quad \mathbf{D}_2 = \begin{bmatrix} \mu + \mu_c & \mu - \mu_c \\ \mu - \mu_c & \mu + \mu_c \end{bmatrix}, \\
&\mathbf{D}_3 = \mathrm{diag}\left[2\mu l_t^2, \quad 2\mu l_t^2, \quad 2\mu l_t^2, \quad 2\mu l_c^2, \quad 2\mu l_c^2, \quad 2\mu l_c^2, \quad 2\mu l_c^2, \quad 2\mu l_c^2, \quad 2\mu l_c^2\right]
\end{aligned} \tag{1}$$

with $c_1 = (1 - n)/(1 - 2n)$ and $c_2 = n/(1 - 2n)$. $m = E/2(1 + n)$. E is Young's modulus and n is Poisson's ratio. m_c, l_c, l_t are three additional material parameters due to the bending and due to the torsional couple-stresses. In order to derive the general expression of the second and third stress invariants in their familiar form, the transformation:

$$\mathbf{s} = \begin{Bmatrix} \bar{\mathbf{s}} \\ \bar{\mathbf{m}} \end{Bmatrix} = \mathbf{P} \cdot \begin{Bmatrix} \tilde{\mathbf{s}} \\ \tilde{\mathbf{m}} \end{Bmatrix} \quad \text{with} \quad \mathbf{P} = \mathrm{diag}\left[\mathbf{P}_1, \quad \mathbf{P}_2, \quad \mathbf{P}_2, \quad \mathbf{P}_2, \quad \mathbf{P}_3\right] \tag{2}$$

can be utilized with

$$\begin{aligned}
&\mathbf{P}_1 = \mathrm{diag}\left[1, \quad 1, \quad 1\right], \mathbf{P}_2 = \begin{bmatrix} a_1 & a_2 \\ a_2 & a_1 \end{bmatrix}, \\
&\mathbf{P}_3 = a_3 \mathrm{diag}\left[l_t^{-1}, \quad l_t^{-1}, \quad l_t^{-1}, \quad l_c^{-1}, \quad l_c^{-1}, \quad l_c^{-1}, \quad l_c^{-1}, \quad l_c^{-1}, \quad l_c^{-1}\right]
\end{aligned} \tag{3}$$

in which a_1, a_2 and a_3 are additional material parameters. The choice $a_1 = a_2 = 1/2$ and $a_3 = 1$ (de Borst, 1991) is adopted. Then, in index notation it holds:

$$J_2 = \frac{1}{2}\left(\bar{s}_{ij}\bar{s}_{ij} + \bar{m}_{ij}\bar{m}_{ij}\right) \quad \text{and} \quad J_3 = \frac{1}{3}\left(\bar{s}_{ij}\bar{s}_{jk}\bar{s}_{ik} + \bar{m}_{ij}\bar{m}_{jk}\bar{m}_{ik}\right) \tag{4}$$

COMPUTATIONAL PLASTICITY

An implicit Euler backward algorithm for integration of the 3D constitutive equations is utilized. Defining the yield surface via $F(\boldsymbol{\sigma}, \alpha) = 0$ in which α is an evolution function which characterizes the size of the surface $\boldsymbol{\sigma}$ corresponds to the current state of stress. Admitting an additive decomposition of strains and postulating

$\dot{\varepsilon}^p = \dot{\lambda}\mathbf{N}(\boldsymbol{\sigma},\alpha) = \dot{\lambda}\,\partial Q/\partial\boldsymbol{\sigma}$ with Q the potential function and $\dot{\alpha} = \dot{\lambda} g(\boldsymbol{\sigma},\alpha)$, a non-linear system is set up as:

$$\begin{aligned} F &= F(\boldsymbol{\sigma}_{n+1},\alpha_{n+1}) = 0 \\ G &= \boldsymbol{\sigma}_{n+1} - \boldsymbol{\sigma}^e + \Delta\lambda D^e : N(\boldsymbol{\sigma}_{n+1},\alpha_{n+1}) \\ S &= \alpha_{n+1} - \alpha_n - \Delta\lambda g(\boldsymbol{\sigma}_{n+1},\alpha_{n+1}) \end{aligned} \tag{5}$$

whose iterative solution results to $(\boldsymbol{\sigma}_{n+1},\alpha_{n+1})$.

MICROPOLAR FORMULATION OF THE DESAI MODEL

The chosen form of the model yield function is given by:

$$F = \frac{J_2}{p_a^2} - \left[-\alpha\cdot\left(\frac{I_1+R}{p_a}\right)^n + \gamma\cdot\left(\frac{I_1+R}{p_a}\right)^m\right]\cdot F_s = 0 \tag{6}$$

with $F_s = (1-\beta\cdot\cos 3\theta)^{-0.5}$ and $\cos 3\theta = 1.5\sqrt{3}\cdot J_3 / J_2^{3/2}$. A physical interpretation of the various parameters can be founded in Desai (1980) and Liu et al. (2004). The potential surface is given by:

$$Q = \frac{J_2}{p_a^2} - \left[-\alpha_Q\cdot\left(\frac{I_1+R}{p_a}\right)^n + \gamma\cdot\left(\frac{I_1+R}{p_a}\right)^m\right]\cdot F_s = 0 \tag{7}$$

All parameters are experimentally determinable. Specific forms for the hardening and softening parameter α and the nonassociative control parameter α_Q can be found in Liu et al. (2004).

EVOLUTION FORMULATION FOR THE LENGTH SCALES

As the particles translate and rotate a significant change in length scales is expected due to the effect of the shape indices and surface roughness of the particles. In this contribution, similar as in Abu-Rub and Voyiadjis (2004), the average internal length scale l_{Ave} is assumed to start with an initial value and then decreased exponentially as a function of shape indices and the effective plastic rotation strain ξ_R. The evolution equation has the form of $l_{Ave} = l_o e^{-k_0\xi_R}$ where k_0 is a material constant and l_o is the initial length scale which is assumed to be as $l_o = \left[(I_{SPH}/I_R)d_{50} + (I_R/I_{SPH})d_{50} + R_a\right]/2$ and I_{SPH}, I_R, d_{50} are the sphere city index, roughness index and the mean particle size respectively. R_a is the mean surface roughness. For the sake of simplification, in this contribution, the length scale parameters l_c, l_t in Eq. (1) and (3) are calculated on the base of l_{Ave}.

NUMERICAL EXAMPLES

Example 1: Strain localization in 3D specimen

A cubic 3D specimen is selected for the numerical simulations, Fig. 1. The finite element mesh consists of 20-noded brick elements. The material parameters have been

derived on the basis of triaxial tests on 'Eastern Scheldt' dense sand (Liu et al. 2004). A confining pressure of 150 kPa is applied to all boundaries of the specimen and kept constant throughout the analysis. Incremental displacements are applied on a rigid platen at the top of the specimen. The left, right and front planes of the specimen can move freely in the normal direction of each plane. The bottom plane of the specimen is constrained in the y-direction. The main material and geometry properties are $E = 79\text{MPa}$, $\nu = 0.29$, $m = 1.795$, $\gamma = 0.155$, $n = 4.36$, $\beta = 0$, $I_{SPH} = 0.6565$, $I_R = 1.0878$, $d_{50} = 0.72$, $k_0 = 68.6$, $R_a = 0.946$, $L = 100\text{mm}$, $B = 50\text{mm}$, $W = 5\text{mm}$.

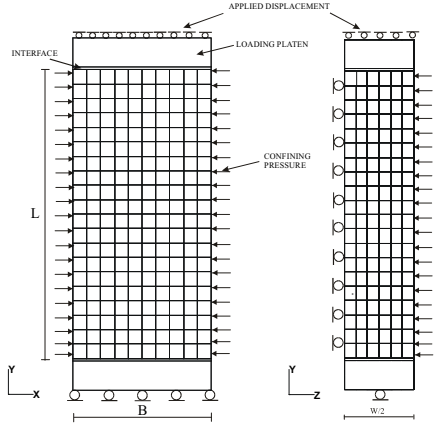


FIG. 1. Schematic of 3D specimen geometry and loading conditions

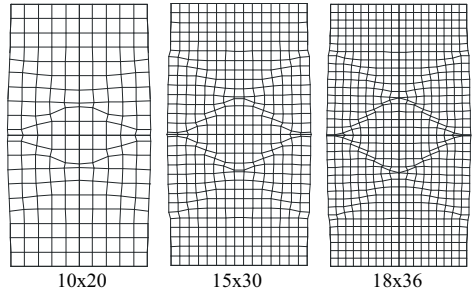


FIG. 2. Deformation patterns of the three meshes

In order to verify mesh insensitivity of the model, three finite element meshes with densities of 10x20, 15x30, 18x36 elements respectively are examined. The three deformed meshes, at the same level of vertical displacement, are compared in Fig. 2. The corresponding contours of effective plastic strain are shown in Fig. 3. It is obvious that the localization is captured correctly and the thickness of the localization zone converges to a finite bandwidth without dependency on mesh refinement, Fig. 3.

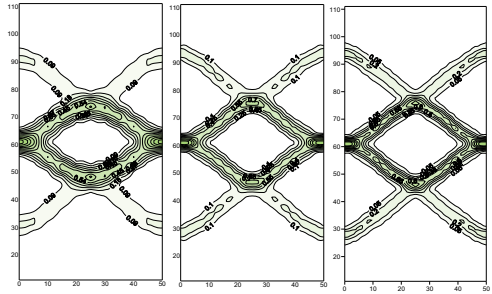


FIG. 3. Contour plots of the effective plastic strain in the four meshes

Example 2: Geotechnical slope failure simulation

A typical slope failure problem under plane strain conditions is selected for demonstration of the model potential. The geometry and the boundary conditions are shown in Fig. 4. A normally consolidated clay is chosen. Two material simulations are compared, a dry (single phase) case and a fully saturated. The main material properties are $E = 20\text{MPa}$, $\nu = 0.2$, $m = 1.8$, $\gamma = 0.0044$, $\beta = 0$, $n = 2.54$, $k_w = 1e-08\,\text{m/s}$.

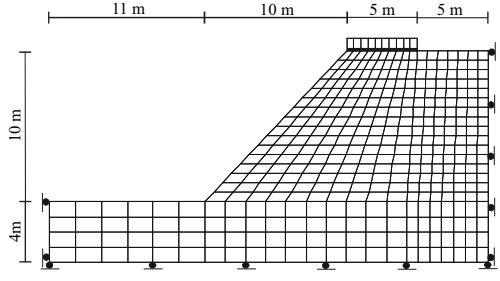


FIG. 4 Schematic of finite element mesh of the slope

The load is applied by means of increasing vertical displacements on a rigid plate resting on its crest. Cohesionless interface elements have been introduced under the rigid plate.

In Fig. 5 and 6, at a vertical plate displacement of 430 mm, the distributions of effective plastic strains and the plastic rotations are compared for the dry and the fully saturated cases.

It is evident that the effective plastic strains and the plastic rotations for the saturated case are higher than the dry one. On the other hand, the thickness of the plastic rotation zone is thicker for the dry case. In both cases, the zone of effective plastic strains is embedded within the zone of plastic rotations.

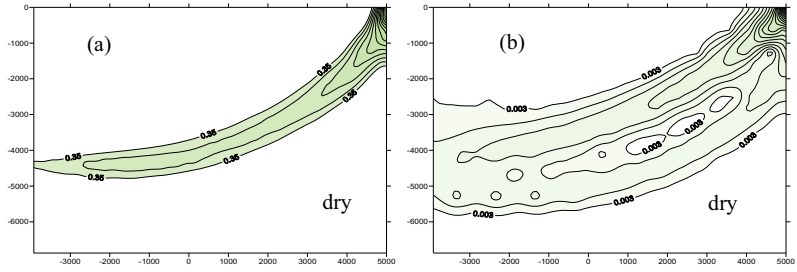


FIG. 5 Contour of (a) total effective plastic strains and (b) total grain rotations

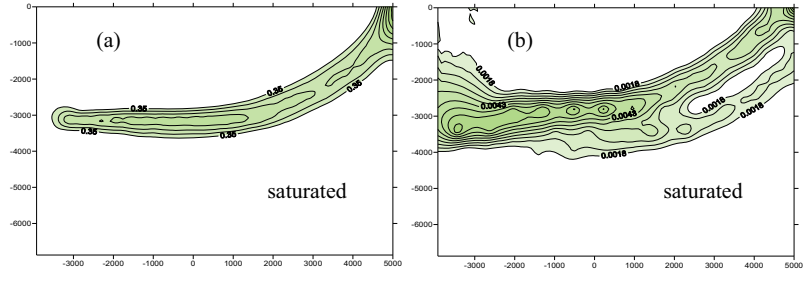


FIG. 6 Contour of (a) total effective plastic strains and (b) total grain rotations

CONCLUSIONS

The developed formulation provides an easy means for extension of most J2 and/or J3 plasticity models to micropolar continua. The numerical results show that formation of the Desai hierarchical concept on the basis of a micropolar continuum theory introduces the necessary regularization aspects for utilization of the model in studies of post peak response.

REFERENCES

Abu-Rub, R.K., Voyiadjis, G.Z. (2004). "Analytical and experimental determination of the material intrinsic length scale of strain gradient plasticity theory from micro- and nano- indentation experiment." *Int. J. Plasticity*, Vol. 6: 1139-1182

de Borst, R. (1991). "Simulation of strain localization: a reappraisal of the micropolar continuum." *Engineering Computations*, Vol. 8**:**317-332.

Desai, C.S. (1980). "A general basis for yield, failure and potential functions in plasticity." *International Journal for Numerical and Analytical Methods in Geomechanics*, Vol. 4: 361-375.

Liu, X., Cheng, X.H., Scarpas, A. and Blaauwendraad, J. (2004). "Numerical modelling of non-linear response of soil, Part 1: Constitutive Model." *International Journal of Solids and Structures*, Vol. 42(7): 1849-1881.

Application of Fuzzy Sets to Geological Strength Index (GSI) System Used in Rock Slope

Yong-Jie Zhang[1], Wen-Gui Cao[2], and Ming-Hua Zhao[3]

[1]Ph.D candidate, Geotechnical Engineering Institute, Hunan University, Changsha, China, 410082; yjiezhang309@yahoo.cn
[2]Professor, Geotechnical Engineering Institute, Hunan University, Changsha, China, 410082
[3]Professor, Geotechnical Engineering Institute, Hunan University, Changsha, China, 410082

ABSTRACT: The stability assessment of slopes is difficult because characterization of rock masses and determination of their strength involve many uncertainties due to their complex nature. The fuzzy set theory is one of the tools to handle such uncertainties. And the difficulty can be overcome by using the Hoek-Brown empirical failure criterion in conjunction with the Geological Strength Index Classification System and fuzzy sets to express the uncertain parameters. For the stability assessment of slopes, a methodology has been presented in the study to process the fuzzy uncertainties in a slope reliability analysis. Simplified Bishop's method and interval theory were used to calculate the safety factor intervals with α-level intervals. The slope failure possibility was obtained by non-probabilistic fuzzy reliability analysis method and the possibility theory. In addition, a numerical example of slope instabilities in heavily jointed rock masses was analyzed and the result was evaluated to demonstrate and to check the performance of this approach. Its failure possibility is zero, which matches well with the result 0.12% of Monte Carlo method.

INTRODUCTION

According to Goodman (1995), when the materials are natural rock, the only thing known with certainty is that this material will never be known with certainty. In recent years, some methodologies in artificial neural networks, fuzzy systems, and evolutionary computation have been successfully combined, and new techniques called soft computing or computational intelligence have been developed. These techniques are attracting more attention in several research fields because they tolerate a wide range of uncertainty (Jin and Jiang, 1999). Some applications of fuzzy logic related to rock mechanics, geotechnics and engineering geology were performed (e.g. Juang et al., 1998; Dodagoudar and Venkatachalam, 2000; Nawari and Liang, 2000; Sonmez et al., 2003; Rubio et al., 2004; Seol et al., 2008). Generally, the purpose of utilizing the fuzzy logic method in these studies is to minimize the uncertainties originating from ignorance and variations.

For slope stability assessment, information on the shear strength parameters are quite limited, and their distributions type of the uncertain variable are difficult to determine. This situation makes the application of classical estimation procedure extremely difficult. Under such conditions of limited information it appears reasonable to make use of fuzzy set theory. The variability of slope material and other uncertainties associated with slope stability led to the development of possibilistic approaches based on conceptual models that parallel those used widely for deterministic studies. If the form of the uncertainty happens to arise because of imprecision, ambiguity or vagueness, then the variable is probably fuzzy and can be represented by a possibility distribution or membership function. The main objective of the paper is to incorporate the fuzzy uncertainty in shear strength parameters of slope and its fuzzy reliability analysis.

FUZZY THEORY IN APPLICATION OF GSI TO ROCK PARAMETERS

The standard method for assessing the strength of a geotechnical material is to recover representative samples and test them in the laboratory. In the case of a closely jointed rock mass it is clearly not possible to recover a sample that is large enough to represent the joint system. In order to overcome this difficulty in laboratory determination of the shear strength of jointed rock masses, the empirical Hoek-Brown failure criterion (Hoek et al., 1997) is commonly used in conjunction with the geological strength index (GSI) classification system based upon the visual impression on the rock mass structure.

The GSI seems a more practical parameter to estimate the strength of jointed rock masses from field observations with rock mass classification. But rock mass classification requires time consuming procedures and has some limitations as discussed by Sonmez et al. (1999, 2003) in detail. However, due to the complex nature of the rock masses, the rock mass classification systems always include some uncertainties, which result in difficulty in determination of the rock mass parameters and their rating used by the systems as definite values. As Hoek (1998) indicates that although some geologists go to extraordinary lengths to try to determine an ‘exact’ value of GSI, geology does not lend itself to such a precision and it is simply not realistic to assign a single value. The fuzzy set theory is one of the tools to handle such types of uncertainties. The study done by Sonmez (2003) is an attempt to provide an approach utilizing the fuzzy set theory for determining GSI ratings to be used by the empirical failure criterion. The original GSI system is modified with fuzzy sets and a Mamdani fuzzy algorithm is constructed employing 23 ‘‘if–then’’ rules for evaluating discontinuity parameters and their ratings considered in the GSI system. The suggested GSI chart considering fuzzy sets is shown in Fig. 1. It considers the effect of structure rating (SR), calculated by the volumetric joint count (J_v), and surface condition rating (SCR), calculated by the rating of roughness (J_r), weathering (J_w) and infilling (J_f). Then the triangular membership functions of GSI values can be gained through Fig.1 and the method proposed by Sonmez (2003).

According to the fuzzy theory (Zadeh, 1978), the fuzzy GSI can be changed into a group of α-level intervals. By replacing fuzzy numbers with intervals, the analysis with uncertain parameters reduces to a series of interval analyses. Then the triangular fuzzy membership functions of shear strength parameters c and φ shown as

$\tilde{c} = (c^{\mathrm{L}}, c^{\mathrm{M}}, c^{\mathrm{R}})$ and $\tilde{\varphi} = (\varphi^{\mathrm{L}}, \varphi^{\mathrm{M}}, \varphi^{\mathrm{R}})$ can be calculated in conjunction with Hoek-Brown critical (Hoek et al., 1997) and interval theory (Alefelda and Mayer, 2000). c^{L}, c^{M} and c^{R} are respectively the left value, middle value and right value of the triangle fuzzy number $\tilde{c}$, the same as $\tilde{\varphi}$. For example, the triangle fuzzy number $\tilde{c}$ and its α-level interval can be shown in Fig. 2.

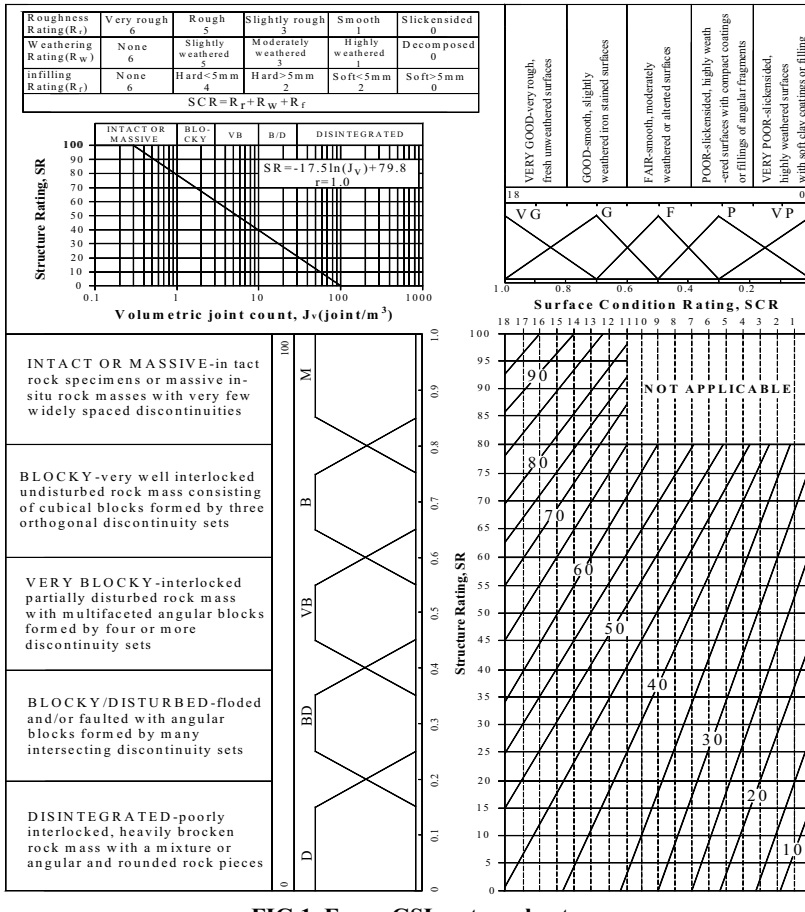


FIG.1. Fuzzy GSI system chart.

FUZZY RELIABILITY ANALYSIS OF SLOPE STABILITY

There are different techniques for solving stability problems depending on which assumption is used to make the problem determinate. The greatest uncertainties in stability problems arise in the selection of the pore pressure and strength parameters.

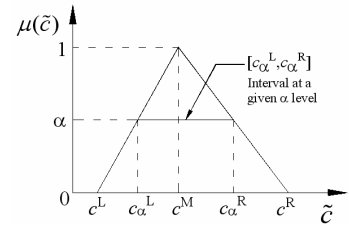


FIG.2. Triangular membership functions of parameter *c*

The error associated with the rigorous method of analysis, amounting to about 5% difference in computed factor of safety for the relatively better techniques, is small compared to that arising from the selection of strength parameters. In the present study, Bishop's simplified method has been used to analyze the stability of rock slope. The uncertainties in the rock parameters can be incorporated in the analysis of safety factor by considering them as fuzzy variables. In the present study, the fuzzy uncertainties of parameters c, φ and γ are considered. The triangle fuzzy number $\tilde{c}$ and $\tilde{\varphi}$ can be determined by the method proposed before, and $\tilde{\gamma}$ can be gained by its mean value and coefficient of variation.

The main idea of using fuzzy sets is to express the uncertain rock parameters as triangle fuzzy numbers into a group of α-level intervals. By replacing triangle fuzzy numbers with intervals, the analysis can be done by a series of interval analyses. Juang et al. (1998) presented the analysis method to calculate the fuzzy set of safety factor. The process can be shown as below:

1. Change the triangle fuzzy numbers $\tilde{c}$, $\tilde{\varphi}$ and $\tilde{\gamma}$ into interval numbers $[c_\alpha^L, c_\alpha^R]$, $[\varphi_\alpha^L, \varphi_\alpha^R]$ and $[\gamma_\alpha^L, \gamma_\alpha^R]$, where $\alpha = 0,\ 0.1,\ 0.2,\ \cdots,\ 1.0$. Then make the three interval numbers into eight musters, such as $\{c_\alpha^L, \varphi_\alpha^L, \gamma_\alpha^L\}$, $\{c_\alpha^L, \varphi_\alpha^L, \gamma_\alpha^R\}$, $\cdots$, $\{c_\alpha^R, \varphi_\alpha^R, \gamma_\alpha^R\}$.

2. Make use of Bishop's simplified method and each muster to calculate the safety factor of slope, eight factors can be gained. Regard the maximal value as F_α^R, the minimal value as F_α^L, and the interval number $[F_\alpha^L, F_\alpha^R]$ is the result of slope safety factor with α-level.

3. Calculate the slope safety factors of eleven different levels from 0 to 1.0, the triangle membership functions $\tilde{F}$ can be got.

In order to evaluate the slope stability from the triangle fuzzy number $\tilde{F}$, the stability of slope is classified into four classes with the analysis method proposed by Juang et al. (1998). Method was also used by Sonmez (2003). This method can propose the qualitative results and the classification grade but not the quantitative result. So the non- probabilistic fuzzy reliability measuring method is introduced to evaluate the triangle fuzzy number $\tilde{F}$, which can provide the failure possibility and stable inevitability.

For the acceptable safety factor F_{ac}, which usually is a certain value, the performance function can be shown as below:

$$\tilde{Z} = g(\tilde{c}, \tilde{\varphi}, \tilde{\gamma}) = \tilde{F} - F_{ca} \tag{1}$$

When the triangle fuzzy number $\tilde{F}$ is changed into interval number $[F_\alpha^L, F_\alpha^R]$ with α-level, the performance function can be changed into standard form according the interval theory. It is shown as below:

$$\tilde{Z}_\alpha = [Z_\alpha^L, Z_\alpha^R] = g(\tilde{c}_\alpha, \tilde{\varphi}_\alpha, \tilde{\gamma}_\alpha) = [F_\alpha^L, F_\alpha^R] - F_{ca} \tag{2}$$

Then, the fuzzy reliability index $\eta_{F\alpha}$ can be got by non-probabilistic reliability theory (Tao, 2007). It is shown as below:

$$\eta_{F\alpha} = Z_{\alpha 0} / Z'_{\alpha} \tag{3}$$

Where $Z_{\alpha 0}$ and Z' are respectively the mean and deviation of the interval value $[Z_{\alpha}^{L}, Z_{\alpha}^{R}]$. When the α-level changes from 0 to 1.0, eleven fuzzy reliability indexes will be got. In order to evaluate the stability of slope from the fuzzy reliability indexes with different α-levels, Cremona and Gao (1997) proposed the possibilistic reliability theory. And the failure possibility π_f and stable inevitability N_r can be shown as below:

$$\pi_f = \mathrm{Poss}(\eta_{F\alpha} \le 1) = \alpha\big|_{\eta_{F\alpha}=1} \qquad \alpha \in [0,1],\ \eta_{F\alpha} \in R \tag{4}$$

$$N_r = \mathrm{Ness}(\eta_{F\alpha} > 1) = 1 - \pi_f \tag{5}$$

Finally, the reliability of slope stability can be evaluated in conjunction with the stable inevitability N_r and the safety standard proposed according to the engineering situation.

CASE STUDY

The site of this slope stability investigation is located in Hunan province of China. The rock is sandstone, which is strongly weathered. The height is 35 m, slope angle is 60 °. According to the engineering geology and the method proposed, the fuzzy GSI is (29, 36, 45). And the triangle fuzzy numbers $\tilde{c}$, $\tilde{\varphi}$ and $\tilde{\gamma}$ can be calculated, they are (95, 106, 119) kPa, (30, 33, 37) °, (24.2, 25.5, 26.6) kN/m^3. If the acceptable safety factor F_{ac} is equal to 1.4, then the fuzzy reliability index $\eta_{F\alpha}$ can be got, which is shown as Fig.3. And the stable inevitability N_r can be gained by the fuzzy reliability analysis method, which is zero. That is to say slope cannot be unstable with F_{ac}=1.4. The slope was also analyzed by the Monte Carlo method. The failure possibility is 0.12%. It shows that the method proposed is reliable.

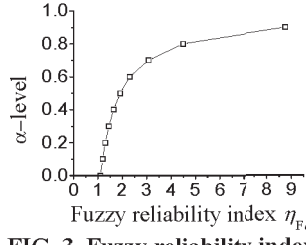


FIG. 3. Fuzzy reliability index

CONCLUSIONS

In this study, the fuzzy set theory is applied to the GSI System by following the fuzzy algorithm. The resulting GSI fuzzy set provides more information than does a single, fixed GSI value as obtained from quantitative GSI chart which is particularly helpful for engineers with little practice on rock masses, and prevents to obtain a wide range of GSI values when the use is made to the original chart. The fuzzy reliability analysis method proposed can be used to evaluate the stability of slope in conjunction with non-probabilistic reliability theory and the fuzzy strength parameters got by the GSI fuzzy set and Hoek-Brown critical. It is noted that the

method is required in the interpretation of the factor of safety in fuzzy sets, and fuzzy set theory may be a useful tool for rock engineers and engineering geologists who study complex rock mass conditions. The fuzzy reliability analysis method seems to be good tools to minimize the uncertainties encountered during the rock engineering and engineering geology projects, because the fuzzy systems have a sufficient flexibility for specific cases.

ACKNOWLEDGEMENT

The writers thank the unnamed reviewers for their comments. Adoption of their comments made the paper clearer and more useful.

REFERENCES

Alefelda, G. and Mayer, G. (2000). “Interval analysis: theory and applications.” *J. Comput. Appl. Math.*, 121(1-2), 421-464.

Cremona, C. and Gao, Y. (1997). “The possibilistic reliability theory: theoretical aspects and applications.” *Struct. Safe.* 19(2), 173-201.

Dodagoudar, G.R and Venkatachalam, G. (2000). “Reliability analysis of slopes using fuzzy sets theory.” *Comput. Geotech*., 27(2), 101-115.

Goodman, R. E. (1995). ‘‘The 35th Rankine Lecture–Block theory and its application.’’ *Ge´technique*, London, 45(3), 381-423.

Hoek, E. and Brown, E.T. (1997). “Practical estimates of rock mass strength.” *Int. J. Rock Mech. Min. Sci*., 34 (8), 1165-1186.

Hoek, E. (1998). “Reliability of the Hoek–Brown estimates of rock mass properties and their impact on design.” *Int. J. Rock Mech. Min. Sci*., 35(1), 63-68.

Juang, C.H., Jhi, Y.Y. and Lee, D.H. (1998). “Stability analysis of existing slopes considering uncertainty.” *Eng. Geol.*, 49(2), 111-122.

Nawari, N.O. and Liang, R. (2000). “Fuzzy-based approach for determination of characteristic values of measured geotechnical parameters.” *Can. Geotech. J.*, 37(5), 1131-1140.

Rubio, E., Hall, J.W. and Anderson, M. G.. (2004). “Uncertainty analysis in a slope hydrology and stability model using probabilistic and imprecise information.” *Comput. Geotech*., 31(7), 529-536.

Sonmez, H. and Ulusay, R. (1999). “Modifications to the geological strength index (GSI) and their applicability to stability of slopes.” *Int. J. Rock Mech. Min. Sci*., 36 (6), 743-760.

Sonmez, H., Gokceoglu, C. and Ulusay, R. (2003). “An application of fuzzy sets to the Geological Strength Index (GSI) system used in rock engineering.” *Eng. Appl. Artif. Intell.*, 16(3), 251-269.

Seol, H., Jeong, S., Cho, C. and You, K. (2008). “Shear load transfer for rock-socketed drilled shafts based on borehole roughness and geological strength index (GSI).” *Int. J. Rock Mech. Min. Sci*., 45(6), 848-861.

Tao, J., Chen, J.J. and Xu, Y.L. (2007). “A semi-analytic method for calculating non-probabilistic reliability index based on interval models.” *Appl. Math. Model.*, 31(7), 1362-1370.

Zadeh, L.A. (1978). “Fuzzy sets as a basis for a theory of possibility.” *Fuzzy Sets Syst.*, 1(1), 3-28.

Measurement of Soil Air Suction Change During Freezing-Thawing Process

Yan Liu[1], Xinbao Yu[2] and Xiong (Bill) Yu[3*]

[1] Graduate Assistant, Department of Civil Engineering Department, Case Western Reserve University, 10900 Euclid Ave Bingham 217, Cleveland, OH 44106, USA, e-mail: y.liu@case.edu, 330-475-5792
[2] Graduate Assistant, Department of Civil Engineering Department, Case Western Reserve University, 10900 Euclid Ave Bingham 203, Cleveland, OH 44106, USA, e-mail: xinbao.yu@case.edu
[3*]Assistant Professor, Department of Civil Engineering Department, Case Western Reserve University, 10900 Euclid Ave Bingham 210, Cleveland, OH 44106, USA, e-mail: xxy21@case.edu, 216-368-6247, corresponding author

ABSTRACT: This paper introduces a new instrument and experimental procedure that estimates the change of air suction in soils during the freeze-thaw process. The experimental procedures include a nondestructive measurement by Time Domain Reflectometry (TDR) sensor, which captures the freezing-thawing status. The change of air suction causes change of soil volume, which is estimated from the volume change and soil deformation modulus. The experimental data indicates there is graduate decrease in the magnitude of the negative air suction, which resulted in volume expansion in soils. The observed bulk volume change is the combined effects of the volume contraction due to ice melting and the volume expansion due to the reduction in the negative air suction. The magntiude of air suction reduction estimated is achieved by fusion the information from both mechanical and electromagnetic measurment.

INTRODUCTION

The change of air suction in freezing granular materials such as soils and concrete has been observed in many model or field study. Air suction is commonly measured by use of porous ceramic materials, due to the ability of such material to allow water to infiltrate while prevent air from infiltration (Fredlund and Rahardjo 1993). In frozen soils ceramic materials can be damaged during the volume expansion by ice crystallization process. Other technologies include thermal conductivity method (Shuai and Fredlund 2000), Time Domain Reflectometry (Topp et al. 1980), tensiometer (Ridley and Burland 1993), granular matrix sensor (Bertolino 2002) and filter paper (Harrison and Blight 1998). The air suction can also be estimated from methods such as dew point meter; the applicability of this method to freezing soil, however, is limited due to its principle of operation. This paper introduces an experimental method that estimates the change of soil air suction during the freezing-thawing process. The principles described in this paper outline the potential to develop

a non-destructive technology to determine the change of air suction in soils during the freezing-thawing process.

BACKGROUND

Negative Air Suction in Porous Media

The special characteristics of porous materials are the existence of pores of different sizes and distributions. Interactions exist among solids, water and air at their interfaces. These interactions generate various magnitudes of microscopic force/pressures acting on the soil skeleton. The vector summation of these forces should be in balance with the external applied forces (Fig. 1).

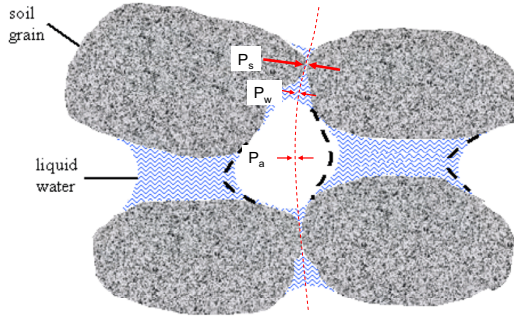


FIG. 1. Schematic of interactions in a soil skeleton

These pressures are expressed as a macroscopic pressure (or equivalent pressure) using the concept of stress. Using the effective stress principles for unsaturated soils, there is,

$$\sigma = \sigma' + (1-x)u_a + xu_w \tag{1}$$

where σ is the total stress, σ' is the effective stress, u_a and u_w and the pore air pressure and pore water pressure respectively, x is the percentage of cross section by water, which is related to the degree of saturation but affected by soil structure (Bishop et al. 1969).

The air pressure is generally expressed as a negative value for cohesive soils to account for the fact that a net suction force occurs inside the pore spaces, resulting from the unbalanced surface tension between soil solids, air and water. Air suction has been measured as high as thousands of kilopascal in highly cohesive soils. The magnitude of air suction is also decided by the degree of saturation in a given soil, which is described by the soil-water characteristic curves.

During the freezing-thawing process, the magnitude of air suction changes. It has been observed that during the freezing process, the increases of the air suction can cause water migration in soil skeleton. The accumulation of water can lead to the formation of ice lenses in frozen soils. However, it has not been possible to directly measure the change of air suction during the freezing-thawing process. This paper presents a method that estimate the magnitude of air suction change at different extent of freezing-thawing status. This method includes a guided electromagnetic wave

technology, called Time Domain Reflectometry, to measure the degree of freezing-thawing status. Details of this technology and experimental design are provided in the subsequent context of this paper.

Time Domain Reflectometry

TDR is an established technology for soil water content measurement. A typical TDR system generally includes a TDR device (pulse generator and sampler), a connection cable, and a measurement probe. The measurement probe is surrounded by materials whose properties are to be measured. TDR works by sending a fast rising step pulse or impulse to the measurement sensor and measuring the reflections due to the change of system geometry or material dielectric permittivity. The ability of TDR for water content lies in the large contrast between the dielectric constant of water (around 81) and that of the air (1) or soil solids (the dielectric constant for dry solids is between 2-7) (Yu and Yu, 2006).

Fig. 2 shows a typical measured TDR signal. Dielectric constant (denoted by Ka in this paper) and electrical conductivity (denoted EC_b in this paper) can be obtained from direct analysis of the time domain TDR signal. Dielectric constant is related to the speed of electromagnetic wave in soils and electrical conductivity is related to the rate of attenuation of electromagnetic wave propagation. The dielectric constant is calculated by Eq. (2).

$$K_a = \left(\frac{L_a}{L_p} \right)^2 \tag{2}$$

where L_a is the apparent length determined from the reflections on a TDR signal, L_p is the length of the probe embedded in the material.

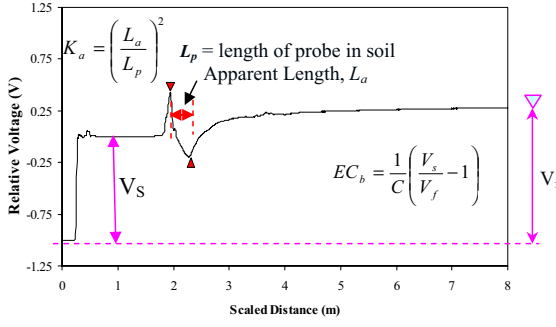


FIG. 2. Typical TDR Output Signal

There are several empirical equations to relate soil water content to TDR measured soil dielectric constant. The Siddiqui and Drnevich equation (Eq. 2) is unique in that it accounts for the effects of soil density and soil type.

$$w = \frac{1}{b}\left(\frac{\rho_w}{\rho_d}\sqrt{K_a} - a \right) \tag{3}$$

where ρ_d is the dry density of soil, ρ_w is the density of water, a and b are soil-dependent calibration constants.

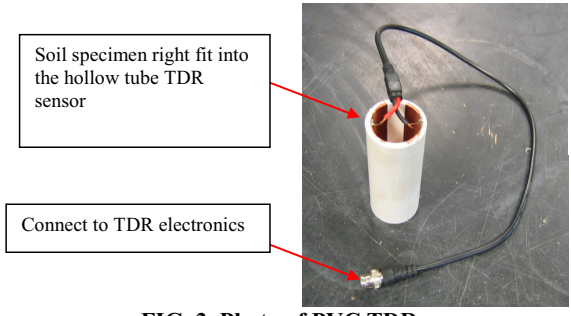


FIG. 3. Photo of PVC TDR sensor

An innovative TDR tube sensor was fabricated to nondestructively measure the change of free water content during the freezing/thawing process (Yu et al. 2008). The underlying principles are that during the freezing/thawing process, the transition between water in liquid and solid (ice) status causes significant change of their dielectric constant (81 for liquid water and 3 for ice). The TDR waveguide was mounted in a PVC tube (Fig. 3). The PVC tube has a diameter which is very close to the specimen prepared. It demonstrated high sensitivity to follow the freeze-thaw process as will be shown in the subsequent context of this paper.

THEORETICAL BASIS FOR AIR SUCTION ESTIMATION

Applying the effective stress principle (Eq. (1)) for frozen soil in the thawing stage, there is,

$$\sigma = \sigma' + (1 - x)u_a + (x - x_1)u_w + x_1 u_{ice} \tag{4}$$

where x_1 is the relative volume of ice in soil skeleton (ranges from 0 to x). u_{ice} is the pressure carried by ice components. The other terms are defined as previously.

The pressure acting on the solid components, i.e, soil solids and ice, can be represented by an equivalent stress, let

$$\overline{\sigma'} = \sigma' + x_1 u_{ice} \tag{5}$$

Equation (1) can be rewritten as,

$$\sigma = \overline{\sigma'} + (1 - x)u_a + (x - x_1)u_w \tag{6}$$

The change of the volume of soil skeleton is caused by the change of the effective stress. During the melting process, the total stress and the pore water pressure can be assumed to be unchanged. The change of effective stress can then be expressed as

$$\Delta\sigma' = \Delta\sigma - \Delta((1 - x)u_a) - \Delta((x - x_1)u_w) \approx -\Delta((1 - x)u_a) \tag{7}$$

where the terms are as defined in the previous equations.

As thaw progresses, the degree of saturation increases. In addition, the magnitude of pore air pressure decreases. The total effect is the reduction in the soil effective stress, which causes the volume expansion. As the amount of volume change is small, the deformation can be assumed in the elastic stage, i.e., there is

$$\Delta\sigma' = E\varepsilon_2 \tag{8}$$

where E is the deformation modulus of soil

Combining Eqs (7) and (8), there is,

$$-\Delta((1-x)u_a) = E\varepsilon_s \tag{9}$$

Or

$$\Delta u_a = -\frac{E\varepsilon_s}{1-x} \tag{10}$$

Eq. (10) provides a way to estimate the relative change of the pore air pressure during the thaw process. This involves measuring the deformation modulus E, volume expansion due to pore air pressure reduction and the corresponding degree of thaw.

EXPERIMENTAL DESIGN

A CL clay collected in Cleveland local construction site was used in the experiment. Nine specimens were prepared at the optimal water content (17%) and compacted using a Harvard miniature compactor. These specimens were compacted in three layers, each layer with 42g of soils. The compaction control aims to develop soil samples with high consistency and similar densities.

After the soil specimens are prepared, they were first frozen in a freezer and then thawed at room temperature. Table 1 summarizes the physical properties and testing program conducted on each specimen. Destructive compressive strength test were performed on soil specimens S1, S2, S3, S6 and S7 at different thaw stages. S4 was used for TDR monitoring of freezing-thawing status, and S5 was used for the measurement of axial deformation during the thaw process.

Table 1. Physical properties of soil specimens and testing program

Specimen No.	Mass (g)	Water content(%)	Function
S1	117.01	17	Compression test at 0 min
S2	118.14	17	Compression test at 13 min
S3	117.68	17	Compression test at 26 min
S4	117.67	17	TDR test
S5	116.81	17	Volume test
S6	116.56	17	Compression test at 39 min
S7	117.63	17	Compression test at 52 min
S8	117.63	17	Back up
S9	115.23	17	reference sample

EXPERIMETAL DATA AND ANALYSES

Monitoring of Degree of Freeze-Thaw by TDR

Figures 4 and 5 show us signals during the freeze-thaw cycle using the developed TDR tube sensor. The signal changes as time increases. The trend of change in these signals indicates this sensor can record the progresses of freeze/thaw process with high sensitivity. The signals in Figure 4 also indicate it takes around 100 minutes for samples to be completely frozen. While Figure 5 shows it takes around 60 minutes for samples to completely thaw. The difference might be due to the difference in the

thermal conductivities of specimen during the freezing/thawing stages. The degree of freezing or thawing can be estimated from the TDR signals via an analyses algorithm, which is described by Yu et al. (2008) and is not repeated here.

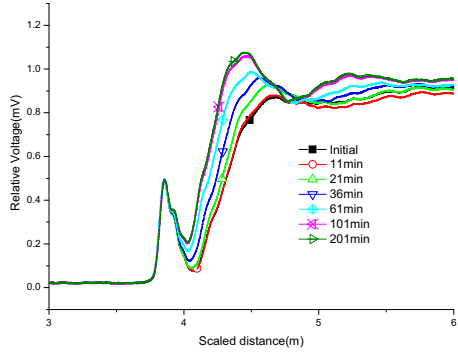


FIG. 4. TDR waveforms at different freezing time.

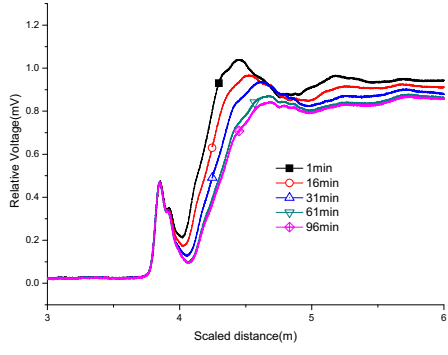


FIG. 5 TDR waveforms at different thawing time.

Volume Change during the Thawing Process

Figure 6 is the measured volumetric strain during the thaw process. The positive sign stands for volume expansion. It can be seen that the volume decrease first and increase next. Since the total volume change can be viewed as being composed of two major components, i.e., 1) the volume change due to the phase change of ice into water, ε_1. As water has larger density than ice, the volume reduces as ice melts; 2) the volume change due to the reduction of the negative air pressure, ε_2. This results in a net decrease of the effective stress on soil skeleton and thus causes the volume expansion. The mathematic representation of the terms can be written as following:

$$\varepsilon_v = \varepsilon_1 + \varepsilon_2 \tag{11}$$

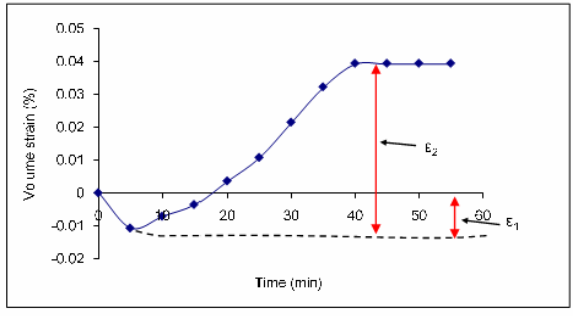


FIG. 6. Components of volumetric strain during thaw process

Estimation of Air Suction Change During the Thawing Process

The magnitude of air suction change at different thaw status can be estimated by applying Eq. (10). When applying this relationship, the strain should only include ε_2 as shown in Fig. 6 and Eq. (11). The deformation modules can be obtained from the stress-strain curve from the unconfined compression test. Figure 7 shows the strain of volume expansion due to air suction reduction as well as the estimated change of air suction for the thawing soil specimen. Similar data are plotted for experimental results on specimens with different moisture contents.

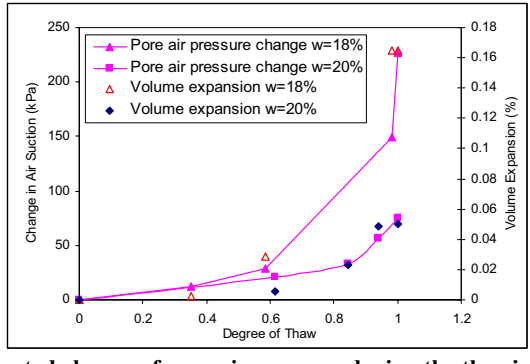


FIG. 7. Estimated change of pore air pressure during the thawing process for specimens of different water contents

Figure 7 shows that there are gradual drop in the magnitude of the air suction pressure as the thawing progresses. Such change is small at the beginning of the thawing process. However, there is a stage (corresponding to around 60-80% degree of thawing) where there is a significant drop in the magnitude of pore air pressure. This is possibly due to the formation of complete percolation path for the air.

It needs to point out, the estimated values of air suction pressure is the net change of soil air suction. The exact values of air suction pressure are dependent upon the air suction in the complete thawing status, i.e.,

$$u_{a,thaw} = u_{a,ini} - \Delta u_{a,t} \quad (12)$$

Where $u_{a,thaw}$ is the air suction pressure at certain thaw status, $u_{a,ini}$ is the air suction pressure when soil is completely thaw, Δu is the change of the air suction pressure as the thaw status changes.

CONCLUSIONS

This paper introduces experimental design that measures the change of soil air suction during the freezing-thawing process. The change of air suction is related to the deformation modulus and the volumetric strain caused by the reduction of the magnitude of air suction. The total volumetric strain of soil while thawing is found to include two components. One corresponds to the phase change of ice into water. The other corresponds to the reduction of the magnitude of air suction. An innovative TDR sensor can be used to non-destructively measure the degree of freezing-thawing. Combining these experimental procedures and techniques, the change of air suction during the freezing-thawing process can be estimated, which is found to fall within reasonable range. With further integration of non-destructive technologies for mechanical properties (such as modulus) determination, it might be possible to develop a technology that measures the change of air suction of freezing-thawing soil specimens non-destructively.

REFERENCES

Bertolino A. (2002).Monitoring the field soil matrix potential using mercury tensiometer and granular matrix sensors, Proceedings of 3rd Int. Conf on Unsaturated Soils, pp335-338.

Fredlund, D.G. and Rahardjo, H. (1993). Soil Mechanics for Unsaturated Soils. ISBN: 978-0- 471-85008-3. Hardcover. 544 pages. August 1993.

Harrison B A and Blight G E. (1998). The effect of filter paper and psychrometer calibration techniques on soil suction measurement. Proc 2nd intconf on unsaturated soils. Beijing: International Academic Publisher, pp362-367.

Ridley A M and Burland J B. (1993). "A new instrument for the measurement of soil moisture suction". *Geotechnique*, 43(2), pp321-324.

Shuai F and Fredlund D. G. (2000). "Use of new thermal conductivity sensor to measure soil suction". *Advances in Unsaturated Geotechnics*. Denver Colorado, 2000. pp1-12.

Topp, G.C., Davis, J.L. and Annan, A.P., 1980. Electromagnetic determination of soil water content: Measurement in coaxial transmission lines. Water Resour. Res., 16: pp579-582.

Yu, X.B., Liu, N., Gonzalez, J. and Yu. X. (2008). New Instrument and Analyses Method for Accurate Freeze-thaw Measurement, *Proceedings of Transportation Research Board Annual Conference,* Washington DC.

Investigation of the Performance of Flexible Airport Pavements under Moving Aircraft Wheel Loads with Wander using Finite Element Analysis

Dona Johnson[1] and Beena Sukumaran[2], A.M. ASCE

[1] Mechanical Engineer, Naval Air Warfare Center Aircraft Division, Lakehurst, NJ-08733, USA; PH: (732) 323-2221; FAX: (732) 323-4781; email: dona.johnson@navy.mil
[2] Associate Professor, Civil Engineering, Rowan University, Glassboro, NJ-08028, USA; PH: (856) 256-5324; FAX: (856)256-5242; e-mail: sukumaran@rowan.edu

ABSTRACT: The introduction of larger and heavier aircraft with more complex wheel configurations is making the current design methods inadequate for airfield pavements. In addition, airport pavements experience significant wander. However, the effect of wander on airport pavement performance has not been evaluated. In previous studies, the stress interactions between each tire of a triple-dual-tandem (TDT) axle used on B-777 and A380 aircraft cannot be captured using a two-dimensional model. In addition, many of these studies have assumed a linear-elastic material behavior of the pavement layers. The purpose of this study is to conduct a three-dimensional finite element analysis to quantify and evaluate the effects of wander and aircraft wheel configurations on the mechanical response of the pavement layers. The flexible pavement system that is modeled in this study is comprised of a medium and low strength subgrade. The stress-strain response of the base, subbase, and subgrade layers are simulated using an elasto-plastic model and the asphalt layer is modeled separately as a viscoelastic and elasto-plastic material. The model parameters are validated using results from laboratory and field tests. The results of the study show how flexible airport pavements are affected when wander and complex gear configurations are considered. Correlations between deformations from a single wheel and 4- and 6- wheel configurations are also studied to understand the effect of gear configuration on flexible airport pavements. Where possible, the results from the analysis are also compared against full scale results available from the National Airport Pavement Test Facility (NAPTF).

INTRODUCTION

The introduction of larger and heavier aircraft with more complex wheel configurations is making the current design methods inadequate for airfield pavements. In addition, airport pavements experience significant wander. However, the effect of wander on airport pavement performance has not been evaluated. In addition, the stress interactions between each tire of a triple-dual-tandem (TDT) axle

used on B-777 and A380 aircraft is a three dimensional problem and cannot be captured using the two-dimensional model that most design methods are based upon. Some design methods use a single "equivalent" wheel load to estimate the effects of larger wheel group. This design method has many apparent inadequacies and is no longer relevant to airport pavement design. Due to the increasing number of wheels being used on modern aircraft, equating larger multi-wheel gear configuration to a single wheel becomes exponentially inappropriate. This technique fails to recognize that larger wheel configurations can span large sections of pavement and can result in a non-traditional rutting pattern (Hayhoe, et al. 1993). Also previous studies and current airport pavement design standards have assumed a linear-elastic material behavior of the pavement layers (FAA 2004). Linear elastic material models are not capable of predicting failure conditions or permanent damage to the pavements.

This research counteracted these problems with current computational design models by using a three-dimensional environment to perform mechanical testing. With three dimensional testing there is no need for equivalent wheel loading, instead full loading on a whole gear will be used. This study tests and compares using other material properties besides linear elastic such as plasticity models. Further exploration of the effect of complex gear loading configurations on the pavement systems and the feasibility of using moving wheel load analysis in designing the pavement structure is also be examined.

MATERIAL VERIFICATION

Material properties used in the Finite Element Model are critical to the accuracy of the model performance and behavior. The extended Drucker-Prager models, which were used in this study, are typically used for modeling granular materials, such as soil and rock, and exhibit pressure-dependent yield. It also allows for volume change with inelastic behavior with a flow rule defining the inelastic straining, allowing simultaneous inelastic dilation and inelastic shearing (HKS 2006). Considerable effort during this study was spent on material verification and determination of suitable material models and properties for the various pavement materials that comprise the pavement system using test data available from the FAA (FAA 2006). The California Bearing Ratio (CBR) test was used to calibrate the model's material properties for the subbase and base. The subbase and base have an assumed elastic modulus and the CBR test is used to find the corresponding friction and dilation angles. Viscoelastic and Drucker Prager material properties of the asphalt layer were calibrated with the results of the CBR tests. These simulations were used to identify the correct instantaneous elastic modulus and shift factor needed to allow the results to fit full-scale test data for viscoelasticity. They are also used to find the plasticity model parameters, which are a combination of elastic modulus, friction and dilation angle, and cohesion that will best fit the FAA Static Punch Test conducted March 2001 at the National Airport Pavement Test Facility (NAPTF).

FIG. 1 shows the cross section for the pavement (Low strength subgrade LFC section) used in this study for material verification and for further analysis. The section is also identical to a cross-section of pavement tested at the National Airport Pavement Test Facility (NAPTF) for full scale testing.



FIG. 1. LFC Cross Section.

Table 1 shows the final Drucker Prager material properties that were obtained from the verification studies for each layer that will be used throughout the studies. More details of the verification studies can be found in previous publications (Johnson 2008).

Table 1. Final Drucker Prager Material Properties

Material	Young's Modulus (MN/m^2)	Friction Angle	Dilation Angle	Cohesion (kN/m^2)	Density (kN/m^3)	Poisson's ratio
P-401	3447	20	5	4.32	25	0.3
P-209	276	50	5	0.72	25	0.3
P-154	138	45	5	0.92	23.8	0.35
Low strength subgrade	20.7	0.01	0.067	4.6	14.8	0.45

WANDER MODELS

This section discusses the effects of wander and wheel configuration on flexible pavement structure. One and four wheels are tested with and without wander. The results from a four wheel gear configuration with and without wander are presented here. The wander pattern mimics the standard distribution that the FAA uses in testing (Hayhoe and Garg 2002); however instead of 66 runs down and back, this model only uses eight due to time and memory constraints (Johnson 2008).

The overall finite element model dimensions used in the study are 30 feet by 40 feet by 6 feet deep. The model contains 12880 brick elements (C3D8R) and 1840 infinite (CIN3D8) elements, and 17343 nodes. The elements in the loaded center section of the model have dimensions of 10.5 inches long by 6 inches wide. FIG. 2 shows the deformation in the asphalt layer after 8 cycles of loading for a 4-wheel gear configuration. The dotted line is for wander after 8 cycles of the abbreviated wander pattern. It can be seen that the surface deflection of the asphalt layer after 8 cycles of

loading is reduced when wander takes place as compared to trafficking with no wander.

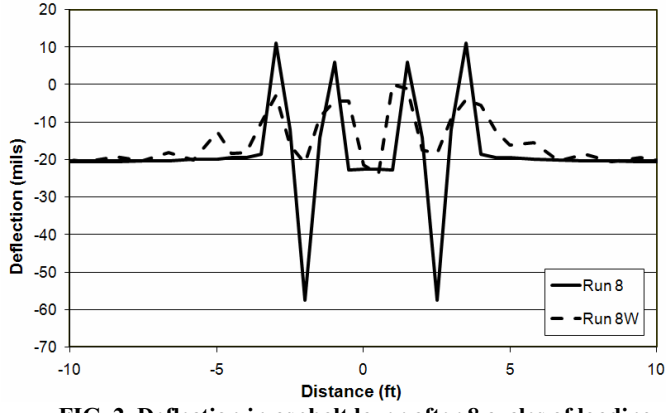


FIG. 2. Deflection in asphalt layer after 8 cycles of loading.

FIG. 3 displays the vertical plastic strain in the subgrade layer under four wheels with and without wander. The assumption for this study is that compressive strains are negative. The dotted line represents the results for four wheels with wander after 8 cycles of the abbreviated wander pattern and the solid lines represent the plastic strain in the subgrade after 8 cycles of loading with no wander. Four wheels with wander causes 29% more permanent strain in the subgrade.

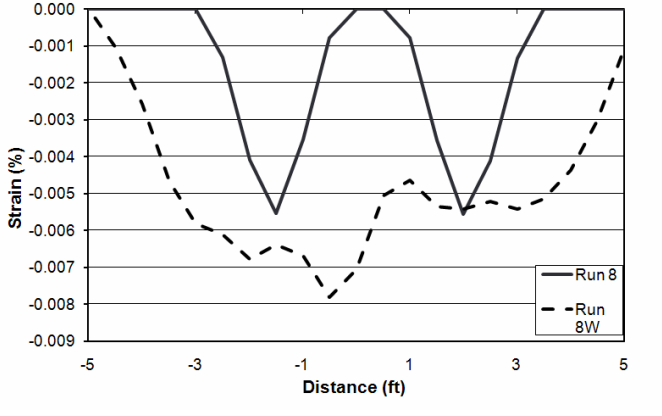


FIG. 3. Vertical Plastic Strain in Subgrade using Four Wheel with and without Wander.

FIG. 4 shows the vertical plastic strain in the subgrade under four wheels without wander. Plastic strain decreases with each run and can be estimated with a linear equation. Though the magnitude of plastic strain in the subgrade is low, the rate of decrease of vertical plastic strain in the subgrade is linear and implies that the plastic strain accumulation in the subgrade will continue to decrease at the same rate with each subsequent run.

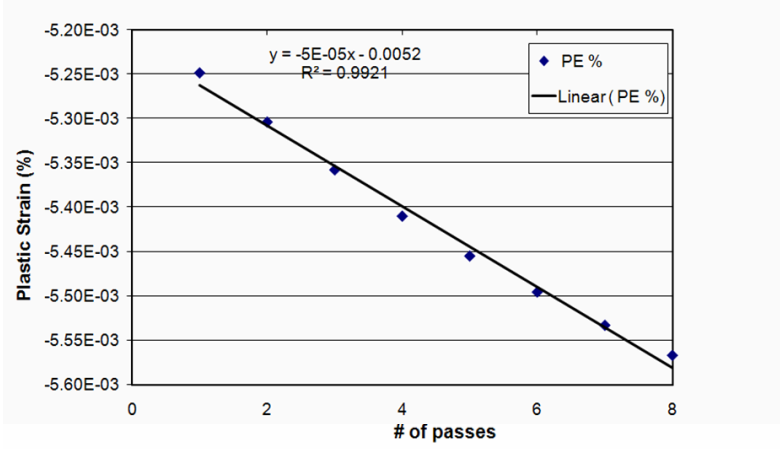


FIG. 4. Vertical Plastic Strain Accumulation in Subgrade without wander.

FIG. 5 shows the vertical plastic strain in the low strength subgrade of LFC pavement under four wheels with wander. The plastic strain decreases with each run can be described by a log function that tapers off with each run. This implies that wander causes higher magnitudes of vertical permanent strain in the subgrade but the rate of plastic strain accumulation with each subsequent cycle of loading diminishes.

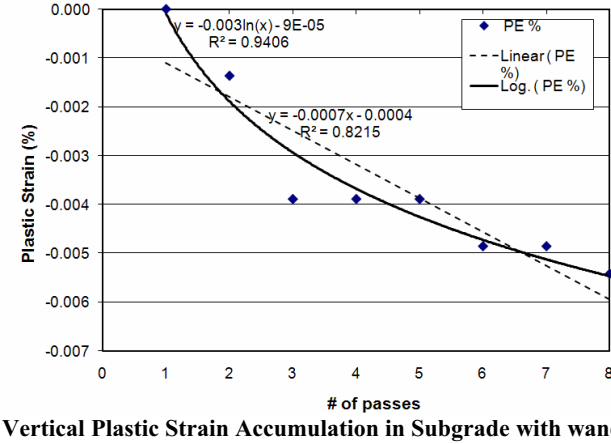


FIG. 5. Vertical Plastic Strain Accumulation in Subgrade with wander.

CONCLUSIONS

Based on the study of the four wheel gear configuration under quasi-static loading, there are several conclusions that can be drawn. Deflection and upheaval in the asphalt is greater without wander than with wander. In the subgrade, wander causes more stress to be transmitted which leads to a greater amount of vertical plastic strain. Wander also allows for greater vertical stress and plastic strain to be imparted to the subgrade. Rutting and upheaval show decaying attenuation rate. Each run has a diminishing increase in rutting and upheaval. These results indicate that pavement is showing signs of consolidation. If rutting and upheaval rates were accelerating, then the pavement would be showing signs of structural failure. As permanent deformation increases, the amount of increase of elastic strain becomes smaller. This is why a decay function, such as a log function, describes the rate of elastic strain increase. There is a clear difference with plastic strain; wander allows for higher magnitude of plastic strain to be imparted to the subgrade but the rate of increase of plastic strain with each pass of the wheel is reduced. This is important when determining the life of the pavement with wander because even though surface rutting might be reduced due to wander for initial cycles of loading, the greater plastic strains induced in the underlying layers might induce shear failure and reduces the life of the pavement.

ACKNOWLEDGEMENTS/DISCLAIMER

The work described in this paper was supported by the FAA Airport Technology Research and Development Branch, Manager, Dr. Satish K. Agrawal. The contents of the paper reflect the views of the authors who are responsible for the facts and accuracy of the data presented within. The contents do not necessarily reflect the official views and policies of the FAA. The paper does not constitute a standard, specification, or regulation.

REFERENCES

Federal Aviation Administration, (2004) “Airport Pavement Design and Evaluation,” FAA Advisory Circular 150/5320-6D.

Federal Aviation Administration, (2006) “Material Properties Database Spreadsheets” http://www.airtech.tc.faa.gov/NAPTF/

Hayhoe, G., McQueen, R and Guo, E. (1993) “Airport Pavement Test Machine Design and Cost Study,” FAA Air Traffic Activity, 30 Sep 93, 286 pages.

Hayhoe, G. and Garg, N. (2002) “Subgrade Strains Measured in Full-scale Traffic Tests with Four- and Six-wheel Landing Gears.” FAA Airport Technology Transfer Conference.

HKS, (2006), ABAQUS Theory and Users Manual – Version 6.6, *Hibbit, Karlsson & Sorenson, Inc.*, Pawtucket, Rhode Island.

Johnson, D (2008), Investigation of the Performance of Flexible Pavement Systems under Moving Loads using Finite Element Analyses, Master’s thesis, Rowan University.

Characteristics of Pore Pressure and Volume Change during Undrained Loading of Unsaturated Compacted Granite Soil

Chan-Kee Kim[1], Woong-Ki Hwang[2], Yongkyu Choi[3], Minhee Lee[4] and Tae-Hyung Kim[5]

[1] Professor, Daejin University, Korea; ckkim@daejin.ac.kr
[2] Student, Korea Maritime University, 1 Dongsam-Dong Yeoungdo-Gu, Busan, Korea; gold-a1142@nate.com
[3] Professor, Kyungsung University, 314-79 Daeyeon-Dong, Nam-Gu, Busan, Korea; ykchoi@ks.ac.kr
[4] President, G-TEC Inc., 4F, Dongil B/D, 24-7, Namcheon 1-Dong, Suyeong-Gu, Busan, Korea; minheehunt@hanmail.net
[5] Assistant Professor, Korea Maritime University, 1 Dongsam-Dong Yeoungdo-Gu, Busan, Korea; kth67399@hhu.ac.kr

ABSTRACT: A series of triaxial compression tests were performed on samples of compacted granite soils in a modified triaxial cell that can separately control pore air pressure (u_a) and pore water pressure (u_w) in order to examine the characteristics of pore pressure, volume change and stress-strain behavior under undrained loading condition. Unsaturated granite soil samples were prepared by compaction in a mould. These samples were tested at different suction and different confining stresses. The volume change of an unsaturated soil during shearing undrained is much sensitive to the confining pressure compared to the initial water content, and the matric suction. The volume expands during shearing, and the volumetric strain is much larger at the smaller confining pressure and at the higher matric suction. The variation of the internal frictional angle according to the initial water content and the matric suction is negligible, but the effective cohesion increases according to matric suction.

INTRODUCTION

In general, an unsaturated soil generates force that is necessary to absorb water by capillary effect or osmotic suction. Due to this force, the unsaturated soil behaves differently from a saturated soil. This force is defined as total suction. The total suction is divided into the matric suction that is difference between pore air pressure and pore water pressure, and osmotic suction. The osmotic suction occurs usually at special area and special soil, and its value is usually smaller than the matric suction. Meanwhile, the matrix suction is developed by an attractive force between water molecules at contact area between water and air and plays an important role in controlling the shear strength and consequently the stability of many steep slopes.

Thus, the theory of effective stress for saturated soils may not be applicable to such an unsaturated soil.

The state of effective stress of an unsaturated soil can be defined using two sets of independent stress state variables that are the net stress state term, (σ_n-u_a) and suction term, (u_a-u_w). This study aimed at investigating the characteristics of pore pressure, volume change and stress-strain behavior of an unsaturated weathered granite soil. A series of triaxial tests with undrained loading condition were conducted to achieve these objects. The tests were performed with different degree of saturation, confining pressure and suction values.

LITERATURE REVIEW

Since the theory of effective stress for an unsaturated soil proposed by Bishop (1959), many researchers have studied on an unsaturated soil. For example, Bishop and Donald (1961) investigated the shear strength of an unsaturated clayey soil. Jenning and Burland (1962) presented that the stress state variables can be divided into the net average stress and suction. Fredlund et al. (1978) proposed the equation of shear strength of an unsaturated soil in terms of two sets of stress variables. Later, he carried out several researches with his coworker, Morgenstern (1976, 1977). Rahardjo et al. (1990, 1995) investigated the characteristics of pore water pressure and volume change of an unsaturated soil in both drained and undrained conditions. Miller and Nelson (1993) published the results of the study on the characteristics of shear strength and relationship between suction and stress state.

The equation of shear strength for an unsaturated soil proposed by Fredlund et al. (1978) is defined as follows.

$$\tau = c + (\sigma - u_a)\tan\varphi' + (u_a - u_w)\tan\varphi^b \qquad (1)$$

where c = effective cohesion; σ–u_a = the net normal stress; ϕ= internal frictional angle; u_a-u_w = matric suction; ϕ^b= angle that indicates the increase of the effective cohesion due to the matric suction. Equation (1) indicates that the shear strength of an unsaturated soil increases as the net normal stress or the matric suction increase. The relationship between σ τ and S is shown in figure 1. This figure shows that one failure surface is formed as the matric suction increases. The increase of cohesion due to increases of matric suction is defined as follows.

$$c = c' + (u_a - u_w)\tan\varphi^b \qquad (2)$$

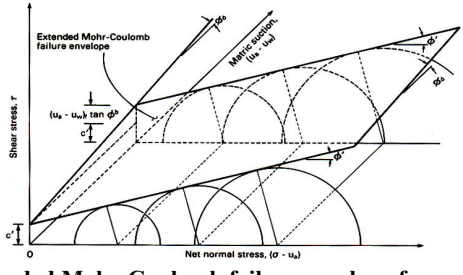


FIG. 1. Extended Mohr-Coulomb failure envelope for unsaturated soils

EXPERIMENT

Material and Specimen

The weathered residual soil used in this study had been sampled at areas around Pocheon Kyungkido, Korea. The soil was air dried in a room temperature, and then filtered through the sieve #4. The basic material properties are shown in Table 1. Three sets of specimens that have the initial moisture content of 11.6 %(OMC), 6.5% (Dry side), 18.5 %(Wet side), and dry density of 1.7(g/cm^3) which is 92% of the maximum dry density were prepared. The specimens have dimensions 100mm height and 50mm diameter.

Table 1 Material properties on the Pocheon granite soil

d_{max}	O.M.C	LL	PL	#200	GS	Li(%)	USCS
1.85	11.6	NP	NP	17.15	2.67	2.80	SM

Matric Suction

Matric suction of a soil can be measured by means of several methods such as Filter Paper method, Thermocouple Psychrometers method, and Thermal Matric Potential Sensors method etc. Of them is Tensiometer method, which is able to measure in-situ using a fine porous ceramic sensing tip. However, since pore water pressure in an unsaturated soil is negative, it is almost impossible to measure the pore water pressure in the condition of high suction. In this case, a high air entry ceramic disk, or a membrane should be used. The other method is to use a pressure plate apparatus, which adopted the axis translation method developed by Hilf (1956).

In this study, a pressure plate apparatus with a high air entry membrane and a porous ceramic stone was used. The high air entry membrane and the porous ceramic stone allow nothing but water to flow through. Experiments were performed based on the reference, ASTM D 2325.

Triaxial Consolidated Undrained Compression Test

Triaxial tests for unsaturated soils were carried out using the modified triaxial compression apparatus that can control suction value. The suction was applied by means of axis-translation technique to avoid cavitations. In this technique, the air pressure (u_a) and backwater pressure (u_w) were applied on the soil sample. The difference between the air pressure and the backwater pressure applied on the sample is taken as the applied suction ($u_a - u_w$). In the study, the air pressure was applied to the top of the sample whereas the backwater pressure was applied to bottom of the soil sample. The suction applied is not to exceed the air entry value of the high air entry ceramic disc at the cell.

A series of undrained triaxial tests with 3 different confining pressure (1, 2, 4 kgf/cm^2), and 3 different suction values (0.5, 1.9, 2.0 kgf/cm^2) were performed. The rate of strain set to be 0.1%/min. The detail of the test procedure is as follows.

A specimen is first consolidated with applying constant suction pressure. After having done the consolidation, the specimen is subjected to deviator stress. If the initial moisture content of the specimen is, during this stage, different from the matric suction, the deviator stress is applied after the specimen has reached the equilibrium state. In order to confirm whether or not the equilibrium state has been reached, the moisture content with respect to time is monitored. The minimum time that requires

the specimen to be stable is then evaluated. The specimen is subjected to the deviator stress after time that is three times as long as the minimum time.

RESULTS AND DISCUSSION

Stress-Strain Behavior

Deviator stresses and volume changes with respect to axial strain for each case are shown in figure 2. As indicated, the deviator stresses appear to decrease as the initial water contents increase.

The initial tangent seems to be a little stiff for the case that the initial water content is OMC than the wet side. In addition, the maximum deviator stress occurs at small strain. The deviator stress for the initial water content being dry side is less sensitive to the matric suction than that in wet side. That might be because of the attractive force between water molecules at contact area. The volumetric stain appears to be hardly affected by the initial water content. For the smaller confining pressure, the volume expands during shearing, while the volume dilates for the larger confining pressure at about 10% of axial strain. In case or the same confining pressure, similar phenomenon may occur at the larger matric suction.

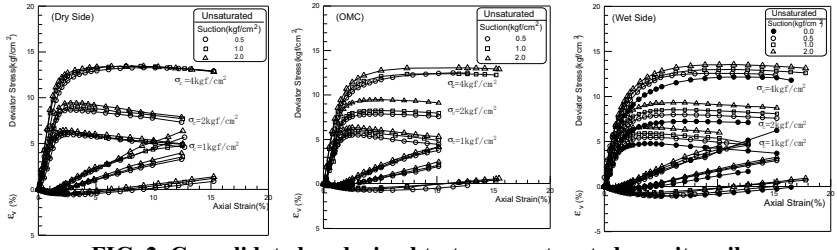


FIG. 2. Consolidated undrained test on unsaturated granite soil

Effective Cohesion

Figure 3 plots the test results in the space of net normal stress, matric suction, and shear stress. According to this figure, as the matric suction increases it forms a failure surface in the space. This is the Mohr-Coulomb failure surface at constant matric suction. There seems to be small changes in internal frictional angle appears to be almost constant according to the matric suction, while effective cohesion seems to increase. The increases of the effective cohesion for each case are ϕ^b=3°(dry side), 8° (OMC), and 9°(wet side).

Figure 4 shows the relationships between the matric suction and the cohesion. In this figure, the solid line represents a linear regression, and the dotted line represents a polynomial regression. As we can see, the cohesion for dry side of the initial water content appears to be 0.98 (linear regression), and 0.96 (polynomial regression). In the other two cases, we can hardly see difference between the linear and the polynomial regression. Thus, we may conclude that it is really not matter which regression analysis is chosen, when evaluates a slope that indicates increase of the effective cohesion due to increase of the matric suction.

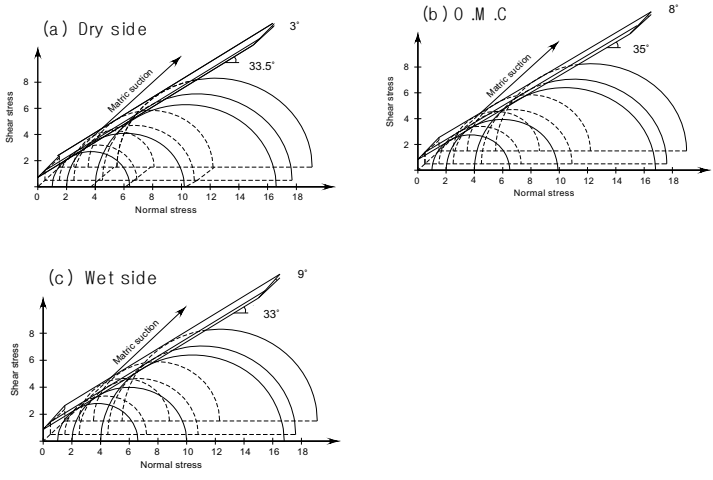


FIG. 3. Extended Mohr-Coulomb failure envelope for consolidated undrained test on the unsaturated Pocheon granite soil

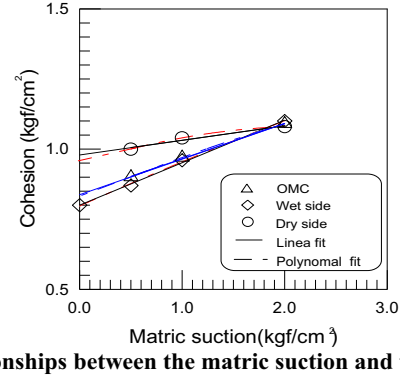


FIG. 4. Relationships between the matric suction and the cohesion for consolidated undrained tests

Pore Air Pressure

Since the volume of an unsaturated soil varies during shearing undrained, and the void is filled with air and water, it may be important to bring attention to the mechanical characteristics of pore air pressure and water pressure. The changes in pore air pressure with respect to axial strain with different initial water contents, confining pressures, and matric suctions are shown in figure 5. When the confining pressure is 1 kgf/cm^2, the pore air pressure appears to be positive values at the only beginning part of the axial strain. When the confining pressure is 4 kgf/cm^2, the values of the pore air pressure become positive during almost entire test. And they

appear to be higher as the matric suctions increase, and the initial water content of the wet side is larger.

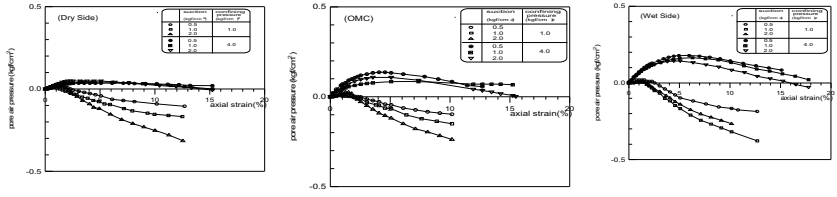


FIG. 5. Variation of pore air pressure with respect to axial strain with different initial water contents, confining pressures, and matric suctions for consolidated undrained tests

Pore Water Pressure

The changes in pore water pressure with respect to axial strain with different initial water contents, confining pressures, and matric suctions are shown in figure 6. The pore water pressure appears to be higher at the confining pressure of 1 kgf/cm^2 than the confining pressure of 4 kgf/cm^2. In case of the same confining pressure, the higher the matric suction the larger the pore water pressure. For instance, for the matric suction of 0.5 kgf/cm^2, the pore water pressure appears to be negative after certain amount of axial strain.

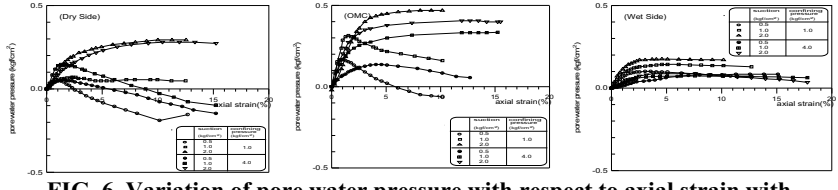


FIG. 6. Variation of pore water pressure with respect to axial strain with different initial water contents, confining pressures, and matric suctions for consolidated undrained tests

CONCLUSIONS

In order to investigate the characteristics of pore pressure, volume change, and stress-strain behavior according to an initial water content of an unsaturated soil, a series of consolidated undrained experiments were conducted. Based on the investigations, we obtained the following results.

The volume change of an unsaturated soil during shearing undrained is much sensitive to the confining pressure compared to the initial water content, and the matric suction.

The matric suction has more influence to the deviator stress, when initial water content is wet side. In most case, the volume expands during shearing. The volumetric strain is much larger at the smaller confining pressure, and at the higher matric suction.

The change of the internal frictional angle according to the initial water content and the matric suction is negligible. However, the effective cohesion appears to increase.

REFERENCES

Bishop, A. W. (1959). "The principle of effective stress." Technisk Ukeblad, 106(99): 859-863

Bishop, A. W. and Donald, I. B. (1961). "The experimental of partly saturated soil in the triaxial apparatus." *Proceeding of the 5th int. conference on soil mechanics and foundation engineering,* 1: 13-21

Fredlund, D. G. and Morgenstern, N. R. (1976). "Constitutive Relations for Volume Change in Unsaturated Soils." *Canadian J. Geotechnical*, 13:261-276

Fredlund, D. G. and Morgenstern, N. R. (1977). "Stress State Variables for Unsaturated Soils." *Pro. ASCE*, 103(5):447-466

Fredlund, D.G., N.R. Morgenstern, and R.A. Widger (1978) The shear strength of unsaturated soils. Canadian Geotechnical Journal. 15(3):313-321

Hilf, J. W. (1956). "An investigation of pore water pressure in compacted cohesive soils." US Bureau of Reclamation, Tech. Mem. 654, Denver, US Bureau of reclamation.

Jenning, J. E. and Burland J. B. (1962). "Limitation to the use of effective stress in partly saturated soils." *Geotechnique*, 12(2):125-144

Ladd, R. S. (1978). "Preparing Test Specimens Using Under compaction." *Geotechnical Testing Journal, GTJODJ*, 1(1): 16-23

Miller, D. J. and Nelson, J.D. (1993). "Osmotic Suction as a Valid Stress State Variable in Unsaturated Soil Mechanics." Unsaturated Soils, *Geotechnical Special Publication* No.30: 64-76

Nelson, J. D. and Drumright, E. E. (1995). "The Shear Strength of Unsaturated Tailings Sand." Unsaturated Soils, 1: 45-50

Rahardjo, H. (1990). "The Study Undrained and Drained Behavior of Unsaturated Soil." Ph. D. dissertation, univ. Saskatchewan, Canada.

Rahardjo, H. and Fredlund, D.G. (1995). "Pore Pressure and Volume Change Behavior During Undrained and Drained Loadings of an Unsaturated Soil." *Proceedings of the First International Conference on Unsaturated Soils*: 165-170

Sonic Wave Testing Technique in Lamellar Rock Mass

Qingfa Chen[1], Keping Zhou[2], and Feng Gao[3]

[1] Ph.D. Student, School of Resources and Safety Engineering, Central South University, Changsha 410083, People's Republic of China; Lecturer, College of resources and environment, Guangxi University, Nanning 530004, People's Republic of China; chenqf79@gxu.edu.cn
[2] Professor, School of Resources and Safety Engineering, Central South University, Changsha 410083, People's Republic of China; kpzhou@263.net
[3] Ph.D. Student, School of Resources and Safety Engineering, Central South University, Changsha 410083, People's Republic of China; gf81412@126.com

ABSTRACT: Sonic wave testing technique is the most commonly used one for ascertaining the loosening zone of roadway surrounding rock, but it has a great limitation in lamellar rock mass. For overcoming the limitation, the problems of sonic wave testing boreholes arrangement mode were studied. Firstly, the theoretical bases of the testing boreholes arrangement in inclined lamellar rock mass were analyzed on the basis of the mechanical characteristics and the propagation rule of sonic wave in layered rock mass. Secondly, three principles of sonic wave testing boreholes arrangement were summarized from numerous testing experiences on field. Then, new arrangement modes in four representative lamellar rock mass (dip angle was respectively 0°, 15°, 45° and 90°) were proposed. The testing results from the engineering example with the gently inclined lamellar rock mass showed the improved arrangement mode could determine the scope of the loosening zone quickly.

INTRODUCTION

The scope of the loosening zone in roadway surrounding rock is an important basis for stability evaluation and support design (Huo et al. 1994). There are many mehods to ascertain the scope of the loosening zone, such as sonic wave testing mehod, seismic wave method, GPR method and so on, and the sonic wave testing method is the most commonly used one. The single-borehole testing method in sonic wave testing method has been widely applied in underground rock engineering by its simplicity in the testing process and less work load than the double-borehole testing method. Fig.1 shows the conventional testing boreholes arrangement mode. If the singel-borehole testing method along the conventional mode to ascertain the scope of the loosening zone in lamellar rock mass, the change of the relationship curves (V_p-L) between p-wave velocity (V_p) and borehole depth (L) would present the irregular feature due to weak interlayers. Only by the curves, the scope of the loosening zone

could not be ascertained difficultly.

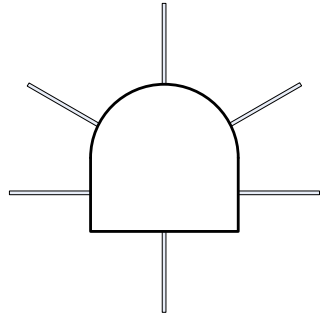


FIG. 1. Conventional testing boreholes arrangement mode.

THEORETICAL BASES OF TESTING BOREHOLE ARRANGEMENT

Theoretical Foundation of Sonic Wave Detection Technique

If rock mass is regarded as the elastic body, unit motion equations can be list as (Chen 1990)

$$\begin{cases} \dfrac{\partial \sigma_{xx}}{\partial x} + \dfrac{\partial \sigma_{yx}}{\partial y} + \dfrac{\partial \sigma_{zx}}{\partial z} = \rho \dfrac{\partial^2 u}{\partial t^2} \\ \dfrac{\partial \sigma_{xy}}{\partial x} + \dfrac{\partial \sigma_{yy}}{\partial y} + \dfrac{\partial \sigma_{zy}}{\partial z} = \rho \dfrac{\partial^2 v}{\partial t^2} \\ \dfrac{\partial \sigma_{zx}}{\partial x} + \dfrac{\partial \sigma_{zy}}{\partial y} + \dfrac{\partial \sigma_{zz}}{\partial z} = \rho \dfrac{\partial^2 w}{\partial t^2} \end{cases} \tag{1}$$

According to the Hooke law, the relationship formula of stress and strain is expressed as

$$\begin{cases} \sigma_{xx} = \lambda\Delta + 2\mu\varepsilon_{xx} \\ \sigma_{yy} = \lambda\Delta + 2\mu\varepsilon_{yy} \\ \sigma_{zz} = \lambda\Delta + 2\mu\varepsilon_{zz} \\ \sigma_{xy} = \mu\varepsilon_{xy} \\ \sigma_{yz} = \mu\varepsilon_{yz} \\ \sigma_{zx} = \mu\varepsilon_{zx} \end{cases} \tag{2}$$

Where ρ is density of medium, u , v and w are the displacement in the direction of x, y and z, $\Delta = \varepsilon_{xx} + \varepsilon_{yy} + \varepsilon_{zz}$ is volumetric strain, λ and μ are Lame coefficient.

From Eq. (1) and Eq. (2), the following equation can be derived as follows:

$$\rho \frac{\partial^2 \Delta}{\partial t^2} = (\lambda + 2\mu)\nabla^2 \Delta \tag{3}$$

Where ∇^2 is Laplace operator.

If a point in rock mass is regarded as the vibration source of wave, change law of Δ with t is given by the following formula:

$$\Delta = \Delta_0 \sin \omega t \tag{4}$$

From Eq. (3) and Eq. (4), the following equation can be derived as

$$V_p = \sqrt{\frac{\lambda + 2\mu}{\rho}} \tag{5}$$

Lame coefficient is an expression about rock elastic modulus E and Poisson coefficient v, namely:

$$\lambda = \frac{Ev}{(1+v)(1-2v)} \tag{6}$$

$$\mu = \frac{E}{2(1+2v)} \tag{7}$$

P-wave formula velocity can be derived.

$$V_p = \sqrt{\frac{E(1-v)}{\rho(1+v)(1-2v)}} \tag{8}$$

From Eq. (8), the sonic wave velocity is closely related to the medium nature. The nature also is theoretical foundation of sonic wave detection technique.

Mechanical Properties of Inclined Lamellar Rock Mass

The inclined lamellar rock mass belongs to the transversely isotropic medium. According to Lekhnilski transversely isotropic medium theory (Lekhniskii 1981), the elasticity modulus meets the formula as follows:

$$\frac{1}{E_\theta} = \frac{\cos^4 \theta}{E_h} + \frac{\sin^4 \theta}{E_v} + \left[\frac{1}{G_v} - \frac{2\upsilon_h}{E_v}\right] \sin^2 \theta \cos^2 \theta \tag{9}$$

Where E_θ is the elastic modulus at θ angle from the rock strata direction, E_h is elastic modulus at parallel direction, E_v is elastic modulus at vertical direction, G_v is shear modulus at vertical direction, υ_h is Poisson's ratio at parallel direction.

From Eq. (9), the elastic modulus of rock mass has the maximum value in the direction parallel to bedding plane and the minimum value in the direction perpendicular to bedding plane. Moreover, the value of elastic modulus decreases with the increase of bedding plane dip angle, which was showed as the line A in Fig.2. Eq. (9) only considered the influence of anisotropy without taking the impacts of bedding plane and micro-joints into account. The studies by Abbas (1998), Zeng (2001) and Nasseri (2003) showed that the minimum value of elastic modulus in lamellar rock mass appeared at the angle of 40°~60°, which was showed as line B in Fig.2. So, line A was just a special case.

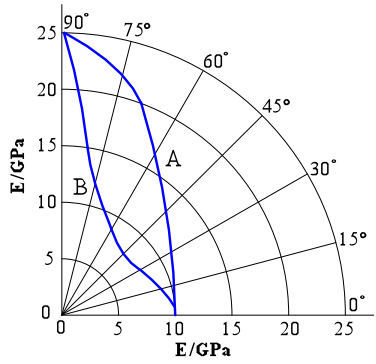


Fig.2 The relationship between elastic modulus and the dip angle of rock strata

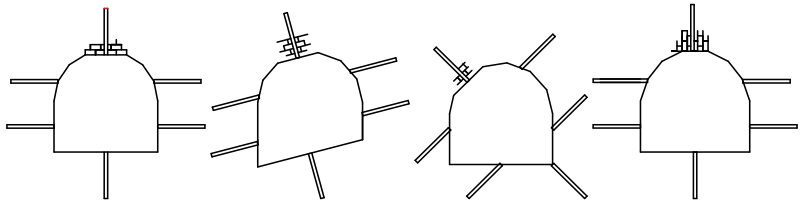
Sonic Wave Propagation Rule in Lamellar Rock Mass

The bedding planes and the filling materials between the strata in lamellar rock mass resulted in the differences of sonic impedance of rock mass, which made the sonic wave spread with directivity (Zhao et al. 2005). When p-wave propagates at angle of α across bedding planes, reflection and refraction appeared. Besides transversal guided wave function and longitudinal resisted wave function of bedding planes increase the propagation time, p-wave velocity attenuated quickly. The more the numbers of the rock strata were, the faster p-wave velocity attenuated. When α was equivalent to $0°$, sonic wave spread parallel to the bedding planes. If boreholes were arranged in a rock stratum and parallel to bedding plane, p-wave velocity change was controlled by the properties of the rock strata. When α was equivalent to $90°$, the sonic wave spreads perpendicular to the bedding planes, and p-wave velocity change affected by bedding planes had a periodic regularity. When α was other angle, the testing data was affected badly by the bedding planes and weak fillings between the interlayers. Combined with the mechanical properties of lamellar rock mass, the corresponding boreholes (intersecting aslant with the rock strata) arrangement mode was not desirable.

PRINCIPLES OF SONIC WAVE TESTING BOREHOLE ARRANGEMENT

The principles of sonic wave testing boreholes arrangement in inclined lamellar rock mass with the different dip angle were proposed through summarizing numerous testing experiences on field. The Principles mostly included: no less than two rows of testing boreholes in the wall height range were arranged in a rock stratum and parallel to the direction of rock strata in roadway walls; on the midline of the surfaces of the roof and the floor, testing boreholes were arranged perpendicular to the bedding planes; the controlling depth of the testing boreholes should be larger than the scope of the loosening zone. Fig.3 showed the testing boreholes arrangement modes for four representative lamellar rock mass. The corresponding dip angle was respectively 0°,

15°, 45° and 90°.



(a)0° **(b)15°** **(c)45°** **(d)90°**

Fig.3. The testing boreholes arrangement modes for the lamellar rock mass

ENGINEERING EXAMPLE

Engineering Background

The ore body No.7 is main one in a certain gypsum with gently inclined lamellar rock mass. Its bedding structure is especially developing. The dip angle of rock strata is about 16°. The thickness is between 20cm~80cm, and 25cm takes the majority. Between the strata there is a weak interlayer formed by sedimentation, which is usually soft shale, clay shale, and other debris etc. The roadway surrounding rock belongs to transversely isotropic medium. Since the mine was exploited, the road heading method along the rock strata direction has been adopted. The phenomena such as separation, fracture and falling of the roof were often happened in the past due to the big section size of roadway. In order to determine the support parameters of surrounding rock in gently inclined lamellar rock mass, the mine took a research on the sonic wave testing of the loosening zone of the roadway surrounding rock.

Analysis of Sonic Wave Testing Result

A RSM-SY5 non-metallic ultrasonic tester developed by Wuhan Rock & Soil Institute of Chinese Academy of Sciences was used in this testing. Single-borehole testing method was adopted on the basis of the improved mode. The testing results of the lower left testing borehole and floor testing borehole in certain roadway 3 # section were analyzed. Fig.4 showed the V_p-L curves.

In Fig.4, the V_p-L curve of lower left testing borehole had an area where V_p value was increased obviously with the improved mode, which made that the scope (about 2.2m) of the loosening zone in roadway wall easily was determined. While the V_p-L curve of floor testing borehole presented more disciplinal, and the V_p value appeared the interval decrease phenomenon reflecting the sonic wave impedance effect of structural planes and weak interlayers. If these abnormally lower V_p value was left out, the scope (about 1.7m) of the loosening zone in floor could be determined rapidly too. Generally, due to the structural effect of rock mass, the scope of the loosening zone in floor was smaller than that in the roadway wall. The results showed new arrangement

mode could determine the scope of the loosening zone in the gently inclined lamellar rock mass quickly.

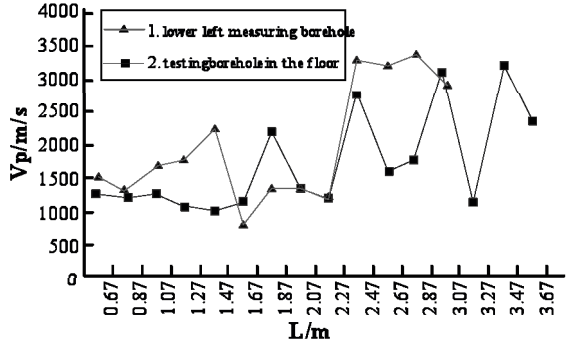


Fig.4. The V_p-L curve of lower left testing borehole and floor testing borehole

COMPARATIVE ANALYSIS WITH CONVENTIONAL TESTING BOREHOLES ARRANGEMENT MODE

In order to analyze the reasonableness of the improved mode, a horizontal testing borehole was arranged nearby lower left testing borehole of 3# section with the conventional moce. Fig.5 showed the V_p-L curve. From this picture, because of the adverse effects caused by bedding planes and weak interlayers with unequal thickness, the V_p value had no an obvious change rule with L. So, it was difficult to determine the scope of the loosening zone. The phenomenon explained that the sonic wave testing borehole arrangement mode had great impact on the testing data.

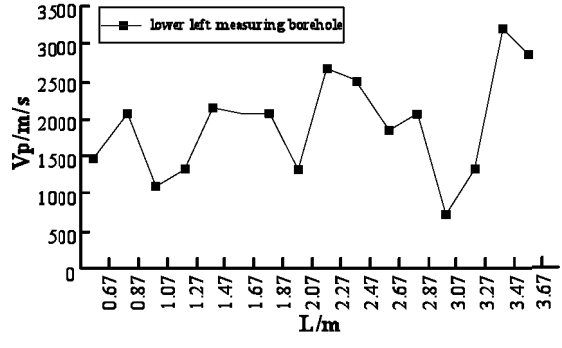


Fig.5. The Vp-L curve of lower left testing borehole using conventional mode

CONCLUSIONS

The traditional arrangement mode of sonic wave testing boreholes in the lamellar rock mass would make the *Vp-L* curves obtained present disorderliness change due to the negative effect of the bedding planes and weak interlayers. It was difficult to determine the scope of the loosening zone of surrounding rock quickly.

The theoretical bases of the testing boreholes arrangement in lamellar rock mass were analyzed on the basis of the mechanical characteristics and the propagation rule of sonic wave in lamellar rock mass. Three principles of sonic wave testing boreholes arrangement were summarized: the testing boreholes in two sides were parallel to the strata; the testing boreholes in the roof and floor perpendicular to the strata; the controlling depth of the testing boreholes should be larger than the scope of the loosening zone. Based on the theoretical bases and the principles, some new arrangement modes in inclined lamellar rock mass with the different dip angle were proposed. The engineering example showed that the new mode had a better applicability, which could quickly determine the scope of the loosening zone.

ACKNOWLEDGMENTS

The authors appreciate the support of National Key Project of Scientific and Technical Supporting Programs Funded by Ministry of Science & Technology of China (No. 2006BAB02A02) and Guangxi University Research Foundation (No. X061068).

REFERENCES

Huo, Z., Gu S., Han, Q. (1994). "Research on measuring cracked range of roadway surrounding rock." *J. XI'AN Mining Institute*, (1): 18-21.

Chen C. (1990). "Engineering rock mass acoustic detection technique." *China Railway Press,* Beijing.

Lekhniskii, S.G. (1981)."Theory of elasticity of an anisotropic body." *Mir Publisher*, Moscow.

Abbas A.F., Al H.T. (1998). "Effect of planar structures on the anisotropy of Ranyah sandstone." *Engineering Geology,* (50): 49-57.

Zeng J., Shao X., Hu X. (2001). "Study on the measuring of rock mass anisotropy." *Study on Hydropower Project*, (2): 8-20.

Nasseri, M.H.B., Rao, K.S., Ramamurthy, T. (2003). "Anisotropic strength and deformational behavior of Himalayan schists." *Rock Mechanics and Mining Sciences*, (40): 3-23.

Zhao M., Xu R.(2005). "The present situation and prospect of the acoustic properties research in rock." *J. Chongqing Jiaotong Institute*, Vol. 19(2): 79-98.

The Pumping Test Data Analyses of Andesite Rock Blocks Aquifer with varied Hydraulic Boundaries by Generalized Radial Flow Model

Wen-Chieh Cheng[1] and James -C. Ni[2]

[1]Ph.D. Candidate, College of Engineering, National Taipei University of Technology, 1, Sec. 3, Chung-hsiao E. Rd., Taipei, 10608, Taiwan; s2428030@ntut.edu.tw
[2]Associate Professor, Dep. of Civil Engineering, National Taipei University of Technology, 1, Sec. 3, Chung-hsiao E. Rd., Taipei, 10608, Taiwan; ckni@ntut.edu.tw

ABSTRACT: The aquifer which includes abundant groundwater resources usually exists at toe of foothill where soil profile at the study area consists of soft silty clay, andesite rock blocks with gravelly sand, and bedrock. A series of constant-rate pumping tests were conducted in the aquifer between two impermeable layers to understand its hydrogeology characteristics. Pumping well is located inside of diaphragm wall, and observation wells are scattered inside and outside of it which was completed before these field experiments. In analytical analyses, diaphragm wall is modeled as impermeable boundary and hillside is assumed as constant recharge boundary. The problem that naturally arises when analyzing data from pumping tests is how to select an appropriate geometry for the particular aquifer system into which flow occurs. This study employs the generalized radial flow (GRF) model to analyze constant-rate pumping test data of the andesite rock blocks-based aquifer and to identify its fractional-flow dimensions further assessing aquifer parameters. This study concludes that the GRF model cannot analyzes the drawdown response if pumping encountered perpendicular boundaries, and the fractional-flow dimension is not unique while other boundaries applied.

BACKGROUND

Sedimentary geological formation usually exhibits transversely anisotropy or heterogeneity due to the sedimentary processes. The fractal theory is widely used to describe the flow geometry especially for complicated aquifer system such as rock blocks aquifer or crystalline fissure rock aquifer. Barker (1988) was proposed the concept of fractional-flow dimension and then developed the generalized radial flow (GRF) model. The GRF model not only can represent the characteristics of the fractured rock aquifer, but also can describe flow cross-sectional area varying with radial flow distance.

Leveinen et al. (1998) performed numerous pumping tests in Finland to characterize fractured aquifer system, and fractional-flow dimensions (1 ─ 1.2 and 1.5) were evaluated by regression analyses of straight-line slopes and type-curve matching. Kuusela-Lahtinen et al. (2003) carried out constant pressure injection test to identify characteristics of the low-conductivity crystalline rock site; however, significant non-uniqueness in many cases in distinguishing fractional-flow dimensions n=2, 2.5 and 3 from each other owing to experimental difficulties in achieving ideal test conditions in the beginning of field experiment. Thus, the Andesite rock blocks-based aquifer discussed herein can be analyzed by the GRF model to represent its hydrogeology characteristics, and then the well configuration can be calibrated so as to reach the optimal deployment and to decrease uplift force beneath the silty clay deposit.

CONCEPT OF THE GRF MODEL

The assumptions of the GRF model can be found in related references (Barker 1988), and the following symbols are defined as they appear. The correlation between throughflow area and distance from source is given by Eq. 1 and Eq. 2 through overall mathematical development, in which r represents radial distance from centre of source measured in the aquifer system, A_n is throughflow area, Γ is gamma function, b is cross-line of flow and n is flow dimension. 1) For one-dimensional linear flow (n=1), throughflow area varies according to $A_n \propto r^0$ being constantly with flow distance from source. 2) For two-dimensional radial flow (n=2), throughflow area varies according to $A_n \propto r^1$, representing that throughflow area increases linearly with flow distance from source. 3) For three-dimensional spherical flow (n=3), throughflow area varies according to $A_n \propto r^2$, indicating that throughflow area increases quadratically with flow distance from source.

$$A_n(r) = b^{3-n}\alpha_n r^{n-1} \tag{1}$$

$$\alpha_n = \frac{2\pi^{0.5n}}{\Gamma\left(\frac{n}{2}\right)} \tag{2}$$

The observation-well responses H(r,p) in Laplace domain can be expressed as Eq. 3, in which Q represents volumetric pumping rate, p is Laplace parameter, r_w is radius of pumping well, C_w is wellbore storage, S_k is skin coefficient and $K_\upsilon(x)$ is υ order modified Bessel function of second kind. λ can be represented as Eq. 4. The correlation between υ and flow dimension n is υ=1-0.5×n. υ can be defined as the slope of logarithmic time vs. logarithmic drawdown. Thus, the Stehfest (1970) algorithm can be applied to establish the type-curve (see Figure 1) through Eq. (3) so as to identify the flow dimension.

$$H(r,p)=\frac{Qr^{v}K_{v}(r\lambda)}{pr_{w}^{v}\left\{C_{w}p\left[K_{v}(r_{w}\lambda)+S_{k}r_{w}\lambda K_{v-1}(r_{w}\lambda)\right]+Kb^{3-n}\alpha_{n}r_{w}^{n-1}\lambda K_{v-1}(r_{w}\lambda)\right\}} \quad (3)$$

$$\lambda=\sqrt{\frac{pS_{s}}{K}} \quad (4)$$

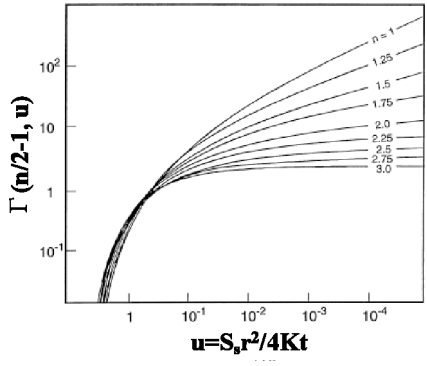


FIG. 1. GRF type-curve (incomplete gamma function) (after Leveinen 1998)

REGIONAL GEOLOGY, HYDROGEOLOGY REPRESENTATION

Geological Formation

In the northern Taiwan, most of mountains around the Taipei basin were covered by volcanic lave flow about two million years ago (Ho 1994). After tremendous volcano eruptions, Taipei basin went through several scenarios such as ground subsidence, stream privacy, barrier lake generation, and so on, to form the recent appearances progressively (Ho 1994). The study area is located at toe of the Ta-Tun volcanic foothills, and is surrounded by volcanoes except for its west side (see Figure 2). The geological formation consists of silty clay (GL. -4.7～-26.3 m), andesite rock blocks with gravelly sand (GL. -26.3～-52.7 m) and bedrock (below GL.-52.7 m). The contractor was requested to concern about the safety during underground excavation because high uplift force acted beneath the clayey deposit, therefore, the aquifer characteristics should be assessed accurately so as to deploy the well points effectively. Through previous field investigations (Cheng and Ni 2008), the aquifer properties, including horizontal hydraulic conductivity K_h, porosity and specific yield (e.g. effective porosity), are 1.45×10^{-2} cm/sec, 29.1%, 28.0%, respectively.

Well Configuration, Monitoring Instruments, Field Experiments

The layout of pumping wells and observation wells is shown in Figure 3(a) and the observation-well responses are indicated from Figure 3(b) to Figure 3(h). The screen of pumping wells are 9.5～16.0 m in length located in the rock blocks aquifer, and the pumping rate and well capability are 214～335 l/min, 5～10 Hp, respectively. The electrical piezometer was installed at each well point to monitor the drawdown response during these field experiments. Figure 3(b) and Figure 3(c) indicate that the large drawdown at P11, P12 and P14 can be referred to the difficulty in recharging came from outside the diaphragm wall further to result in slow recovery. The response-curve of P1, P2 and P3 exhibit high slope consistency presenting the constant boundary existed outside the diaphragm wall provides immediate recharge to preserve the water-level in these well points. There are two scenarios can be seen as Figure 3(d); 1) with the barrier effect, P16 has smaller drawdown than that of the other observation wells, 2) the recharge difficult flows through the barrier, into the interior of diaphragm wall, to result in slow recovery at P11, P12, P13 and P14. According to the comparisons between Figure 3(f) and Figure 3(g), the horizontal barrier is the key factor to bring about the different scale of drawdown and to delay the trigger time of steady-state response as well.

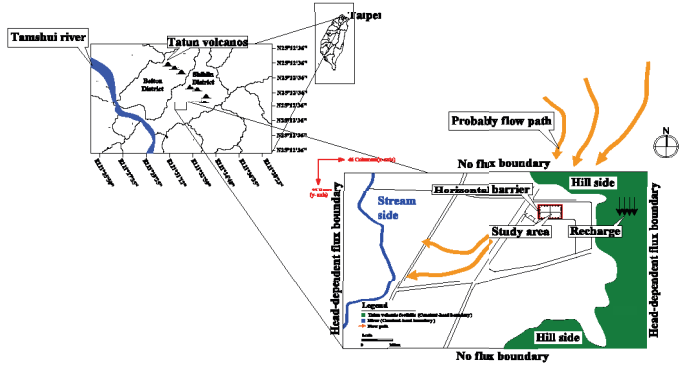


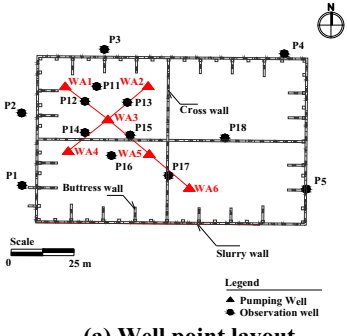
FIG. 2. Topographical lineaments; the probably flow path lied in the NE-SW direction through the testing readings analyzing of field experiments

HYDROGEOLOGY REPRESENTATION

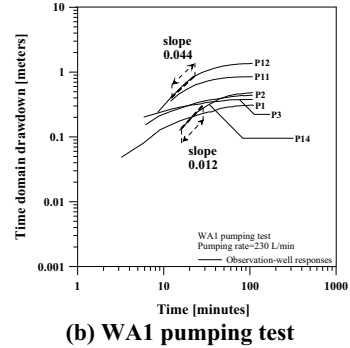
The flow dimension at each well point was identified by linear regression analysis or type-curve matching. Table 1 expresses the results of flow dimension identification and aquifer properties assessment. Only P1, P2 and P3 responses as shown in Figure 3(b) were employed to identify the flow geometry due to continuous slope at large-time,

nevertheless, the scarce data measured before the stabilization from P12 and P14 suggest log-log straight line with regression slope of 0.044 and 0.012, respectively (e.g., n=1.91 and 1.98). The readings made before the start of stabilization at P11, P13 and P14 suggest double logarithmic straight line with regression slope of 0.047 and 0.011 as well as 0.010, respectively (e.g., n=1.91, 1.98 and 1.98) (see Figure 3(c)). The readings of P15 and P16 recorded by the minute suggest log-log straight line between 15～42 and 10～35 min with 0.054 and 0.050 regression slopes (e.g., n=1.89 and n=1.9) (see Figure 3(d)). Furthermore, the readings of P14 and P16 measured by the minute before the stabilization suggest log-log straight line between 50 and 150 minutes with 0.005 and 0.003 regression slopes, respectively (see Figure 3(e)). For the duration of WA5 pumping test, the readings of P16 and P17 recorded by the minute before the stabilization suggest log-log straight line between 20～65 and 60～120 minutes with 0.007 and 0.004 regression slopes (e.g., n=1.986 and 1.992). Last but not least, the readings at P17 and P18 measured before the stabilization recommend the flow geometry of 1.83 and 1.99, respectively (e.g., regression slopes=0.084 and 0.006), during WA6 pumping test.

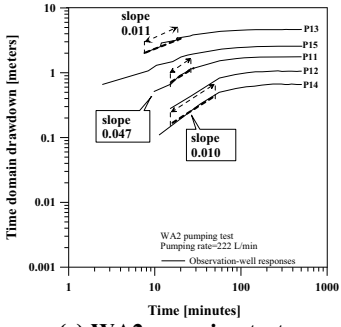
The readings at P4 as shown in Figure 3(f) exhibit suddenly “jump” at long-term response to verify that P4 is not on the flow path of recharge. Through the discussion, it can be quite confident that the strike of recharge in the andesite rock blocks-based aquifer is in NE-SW direction (see Figure 2) further to re-explain why the early steady-state occurring for P1, P2 and P3. Besides, the more complicated water-level responses will arise if encountered perpendicular no-flow boundaries.



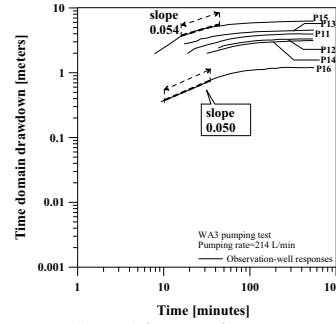
(a) Well point layout



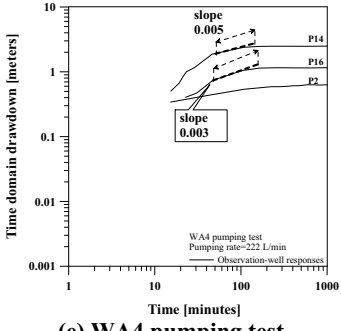
(b) WA1 pumping test



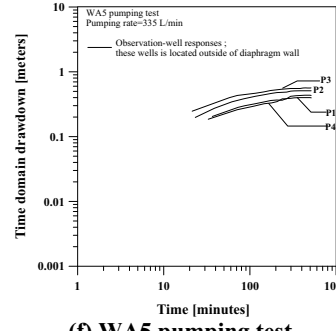
(c) WA2 pumping test



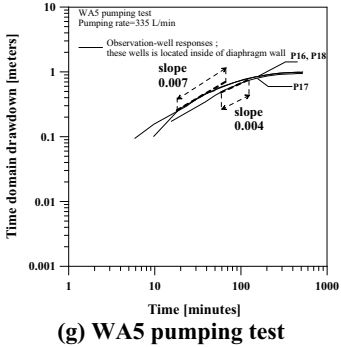
(d) WA3 pumping test



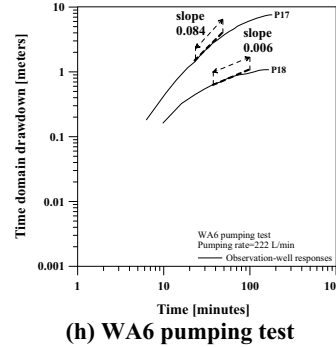
(e) WA4 pumping test



(f) WA5 pumping test



(g) WA5 pumping test



(h) WA6 pumping test

FIG. 3. The observation-well responses with corresponding well deployment

Table 1. The fractional-flow dimensions with corresponding aquifer parameters

Test	Well	Dimensionless distance, ρ	Generalized transmissivity Kb^{3-n}	Hydraulic diffusivity K/S_s	Hydraulic conductivity K (m/min)	Generalized storativity $S_s b^{3-n}$	Specific storage S_s (m^{-1})	Flow dimension *n*
WA1	P1	2.04	3.62×10^{-2}	5.99	5.82×10^{-3}	6.04×10^{-3}	9.72×10^{-4}	2.4
			2.38×10^{-2}	5.37	5.20×10^{-3}	4.44×10^{-3}	9.68×10^{-4}	2.5
			1.72×10^{-2}	5.36	5.10×10^{-3}	3.22×10^{-3}	9.52×10^{-4}	2.6
			1.14×10^{-2}	4.85	4.57×10^{-3}	2.35×10^{-3}	9.43×10^{-4}	2.7
			8.17×10^{-3}	4.75	4.44×10^{-3}	1.72×10^{-3}	9.36×10^{-4}	2.8
			5.40×10^{-3}	4.34	3.98×10^{-3}	1.25×10^{-3}	9.19×10^{-4}	2.9
			2.72×10^{-3}	2.94	2.72×10^{-3}	9.23×10^{-4}	9.23×10^{-4}	3.0
			7.91×10^{-4}	2.93	2.67×10^{-3}	2.70×10^{-4}	9.12×10^{-4}	3.4
			1.23×10^{-4}	2.84	2.57×10^{-3}	4.32×10^{-5}	9.07×10^{-4}	4.0
WA4	P2	1.11	2.02×10^{-2}	38.19	4.41×10^{-3}	5.29×10^{-4}	1.15×10^{-4}	2.5
			1.45×10^{-2}	39.23	4.29×10^{-3}	3.70×10^{-4}	1.09×10^{-4}	2.6
			8.21×10^{-3}	29.94	3.29×10^{-3}	2.74×10^{-4}	1.10×10^{-4}	2.7
			5.73×10^{-3}	30.97	3.12×10^{-3}	1.85×10^{-4}	1.01×10^{-4}	2.8
			3.60×10^{-3}	25.81	2.66×10^{-3}	1.40×10^{-4}	1.03×10^{-4}	2.9
			2.26×10^{-3}	21.68	2.26×10^{-3}	1.04×10^{-4}	1.04×10^{-4}	3.0
			6.22×10^{-4}	20.65	2.10×10^{-3}	3.01×10^{-5}	1.02×10^{-4}	3.4
WA5	P3	2.24	2.81×10^{-2}	12.39	4.53×10^{-3}	2.27×10^{-3}	3.65×10^{-4}	2.4
			1.66×10^{-2}	10.32	3.62×10^{-3}	1.61×10^{-3}	3.51×10^{-4}	2.5
			9.07×10^{-3}	7.43	2.68×10^{-3}	1.22×10^{-3}	3.61×10^{-4}	2.6
			5.70×10^{-3}	7.33	2.29×10^{-3}	7.78×10^{-4}	3.12×10^{-4}	2.7
			2.87×10^{-3}	6.19	1.56×10^{-3}	4.63×10^{-4}	2.52×10^{-4}	2.8
			1.80×10^{-3}	5.99	1.33×10^{-3}	3.01×10^{-4}	2.22×10^{-4}	2.9
			9.06×10^{-4}	5.68	9.06×10^{-4}	1.59×10^{-4}	1.59×10^{-4}	3.0
			2.23×10^{-5}	2.99	4.68×10^{-4}	7.44×10^{-6}	1.56×10^{-4}	4.0

CONCLUDING REMARKS

This study employs the GRF model to analyze a series of constant-rate pumping tests data, and the flow dimension can be identified with type-curve matching or linear regression analyses further to assess aquifer properties accurately. This study concludes that the GRF model cannot apply to identify the flow dimension if pumped with perpendicular no-flow boundaries, and it is not unique when encountered with other hydraulic boundaries. Through hydrogeology representation, the andesite aquifer's flow geometry is ranging between 2.4 and 4.0, which means the sources located in finite radial distance away from the study area further resulting in early steady-state drawdown response occurred. Meanwhile, the delivery capacity gradually decreases with the flow dimension increasing due to preserve the drawdown under a specified radial distance.

REFERENCES

Barker, J.A. (1988). "A generalized radial-flow model for pumping tests in fractured rock." *Water Resources Research*, 24(10): 1796–1804.

Cheng, Wen-Chieh, and Ni James -C. (2008). "Groundwater hydraulic analyses of

confined andesite deposits in Tien-Mou area under constant rate pumping." *Journal of Chinese Soil and Water Conservation*, 39(1): 453–462. (in Mandarin)

Ho, C.S. (1994). "An introduction to the geology of Taiwan explanatory text of the geologic map of Taiwan." Central Geological Survey, Ministry of Economic Affairs, Taipei. (in Mandarin)

Kuusela-Lahtinen, A., Niemi, A., and Luukkonen, A. (2003). "Flow dimension as an indicator of hydraulic behavior in site characterization of fractured rock." *Ground Water*, 41(3): 333–341.

Leveinen, J., Rönkä, E., Tikkanen, J., Karro, E. (1998). "Fractional Flow Dimensions and Hydraulic Properties of a Fracture-Zone Aquifer, Leppa¨virta, Finland." *Hydrogeology Journal*, 6(3): 327–340.

Stehfest, H. (1970). "Numerical inversion of Laplace transforms." *Communications of the Association for Computing Machinery*, 13: 47–39.

Constitutive Model of Soil-Structure Interface under Constant Stress Increment Ratio Stress Paths

Ai-Zhao Zhou[1], Ting-Hao Lu[2], and Zhuang-Ping Gao[3]

[1]Key Laboratory for Geomechanics and Embankment Engineering of Ministry of Education, Nanjing City, China; Geotechnical Research Institute, Hohai University, Nanjing City, China; zhouaizhao@126.com
[2]Geotechnical Research Institute, Hohai University, Nanjing City, China; lutinghao@hhu.edu.cn
[3]Geotechnical Research Institute, Hohai University, Nanjing City, China; gaozhp@hhu.edu.cn

ABSTRACT: The soil-structure interaction attaches great importance to the stability of embankment and retaining wall in expressway engineering. Based on the simple shear test results of sand-concrete interface under the constant stress increment ratio stress paths (CSIRSP), a nonlinear elastic coupling constitutive model is proposed on purpose for describing the interface deformation behavior, including strain softening and normal dilatancy, as well as the effect of stress paths. In the model, the relation curves of shear stress and tangential strain are fitted by a piecewise function composed by hyperbolic function and hyperbolic secant function, while the relation curves of normal strain and tangential strain are fitted by another piecewise function composed by quadratic function and hyperbolic secant function. Finally, the predictions of the model have been compared with experimental results, and results show the model is reasonable and practical.

INTRODUCTION

Many soil-structure interaction questions exist in expressway engineering, such as soil-pile interaction in rigid pile composite foundation, soil-retaining wall interaction, and so on. All these attach great importance to the deformation and stability of embankment and retaining wall. However, the behavior of soil-structure interface plays a major role in the definition of soil-structure interaction. Consequently, the serviceability of a wide range of structures in expressway engineering is dependent on the interface behavior, and its mechanics study is one of the most intractable problems in geosciences.

In order to understand the basic mechanisms and simulate the interaction between soil and structure, many studies have been carried out and various soil-structure constitution models have been present (Desai et al., 1985; Boulon-and-Nova ,-1990; Lu and Bao, 2000; Gennaro and Frank, 2002;-Luan-and-Wu ,-2004;-Wang et al., 2007; Zhou and Lu, 2008). The entire model proposed above are based on the routine simple shear tests, in which the normal stress are constant during the shearing.

Nevertheless, the loading path which the normal stress and the tangential stress increase synchronously exist in practical engineering, for example, the soil-pile interaction during the roadbed filling process, the soil-retaining wall interaction during the soil backfilling process behind the wall. According to these kind of questions, we designed a loading path as constant stress increment ratio stress paths(CSIRSP), in which the ratio value of the shear stress increment to the normal stress increment is constant, and the ratio value is regarded as a parameter η ($\eta=\Delta\tau/\Delta\sigma$). Moreover, we conducted a series of simple shear tests of sand-concrete interface under CSIRSP (Zhou and Lu, 2008).

This paper is devoted to establish a 2D nonlinear elastic coupling constitutive model based on the test results of sand-concrete interface under CSIRSP, which can simulate the interface deformation behavior of strain softening and normal dilatancy, and reflect the effect of stress paths.

MODEL DESCRIPTION

In the proposed model, the incremental strain and stress relationship of interface is described by:

$$\{d\varepsilon\}=\begin{Bmatrix} d\varepsilon_n \\ d\gamma \end{Bmatrix}=\begin{bmatrix} C_{11} & C_{12} \\ C_{21} & C_{22} \end{bmatrix}\begin{Bmatrix} d\sigma_n \\ d\tau \end{Bmatrix}=[C]\{d\sigma\} \tag{1}$$

in which $d\varepsilon_n$ and $d\gamma$ are the incremental normal and tangential strains, while $d\sigma_n$ and $d\tau$ are the incremental normal and shear stresses, respectively. In simple shear tests, the value of $d\gamma$ is independent of $d\sigma_n$, so we can take C_{21} as zero. The rest variables including C_{11}, C_{12} and C_{22} are defined by the relationship of stress-strain curve.

Characters of Tangential Strain

During the shearing, the interface displays the behavior of strain softening, in order to consider the effect of stress path, the relationship between α (stress ratio, $\alpha=\tau/\sigma_n=\tau/(\sigma_0+\tau/\eta)$,$\sigma_0$ is the initial normal stress.) and γ is discussed. The typical α~γ curve is shown in fig.1, where α_f is the peak value of stress ratio, α_r is the residual stress ratio, γ_1 is the strain responding to the peak stress ratio.

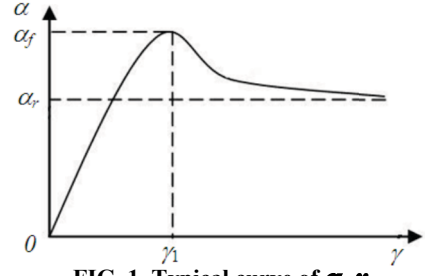


FIG. 1. Typical curve of α~γ.

Piecewise function composed by hyperbolic function and hyperbolic secant function is applied to deal with the curve, and its expression is as follow:

$$\alpha=\begin{cases} \dfrac{\gamma}{a+b\gamma} & 0\le\gamma\le\gamma_1 \\ \alpha_r+(\alpha_f-\alpha_r)\sec h\left[S_1(\gamma-\gamma_2)\right] & \gamma>\gamma_1 \end{cases} \tag{2}$$

in which a and b are the parameters of hyperbolic model, and S_1 is a parameter of the

model governing the shape of the curve in softening segment, which can deduced following a procedure of optimization by successive adjustments. Referring to Duncan-Zhang hyperbolic model, parameter a is defined by: $a=\sigma_0/[Kp_a(\sigma_0/p_a)^n]$, and the K and n are test parameters.

Assume the material follows Mohr-Coulomb failure criterion, and the failure strength is independent on the loading path, we can get that the interface failure when the loading path intersect with the strength envelope. Further, the stress corresponding to the damage state can be obtained by the equation as follow:

$$\begin{cases}\tau = c + \sigma\tan\varphi \\ \tau = (\sigma - \sigma_0)\eta\end{cases} \tag{3}$$

Solve Eq. (3), we can get:

$$\sigma_f = \frac{c+\sigma_0\eta}{\eta-\tan\varphi}, \qquad \tau_f = \frac{c+\sigma_0\tan\varphi}{\eta-\tan\varphi}\eta \tag{4}$$

In order to make the curve continue at the position of $\gamma=\gamma_1$, and consider the Eq. (4), follow relation can be got:

$$\alpha = \frac{\gamma_1}{a+b\gamma_1} = \alpha_f = \frac{\tau_f}{\sigma_f} = \frac{\eta(c+\sigma_0\tan\varphi)}{c+\sigma_0\eta} \tag{5}$$

from Eq. (5), we have:

$$b = \frac{c+\sigma_0\eta}{\eta(c+\sigma_0\tan\varphi)} - \frac{a}{\gamma_1} \tag{6}$$

There are some relations can be found from the test, which are expressed as follow:

$$\alpha_r = \tan\varphi', \quad \gamma_1 = e_1 + f_1\lg(\sigma_f/p_a) = e_1 + f_1\lg\left[(c+\sigma_0\eta)/((\eta-\tan\varphi)p_a)\right]$$

in which φ' is the friction angle of the interface corresponding to the ultimate state, e_1 and f_1 are the fitting parameters, p_a is reference pressure, and can be taken as the atmospheric pressure. Further, differentiating Eq. (2) and comparing with Eq. (1), we can get:

$$C_{22} = \frac{d\gamma}{d\tau} = \begin{cases} \dfrac{a\eta^2\sigma_0}{[\eta\sigma_0+(1-b\eta)\tau]^2} & 0 \le \gamma \le \gamma_1 \\ -\dfrac{\cosh[S_1(\gamma-\gamma_1)]\cdot\coth[S_1(\gamma-\gamma_1)]}{S_1(\alpha_f-\alpha_r)}\cdot\dfrac{\eta-\tan\varphi}{c+\sigma_0\eta} & \gamma > \gamma_1 \end{cases} \tag{7}$$

Analysis above shows that 8 parameters required describing the relation of shear stress and tangential strain. These 8 parameters are K, n, c, φ φ', e_1, f_1 and S_1.

Characters of Normal Compression

The typical relationship between ε_n and γ of interface under CSIRSP is shown in Fig.2. The normal strain ε_n is composed by two parts: one is the normal compression ε_{nc} which is caused by the increment of

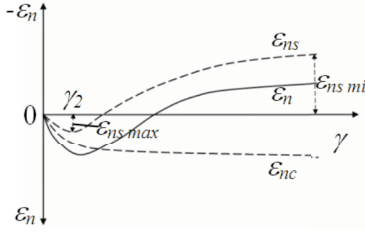


FIG. 2. Typical curve of ε_n~γ.

normal stress, and the other is the normal dilatancy ε_{ns} which is caused by the increment of shear stress.

With the assumption that no coupling effect of normal compression and tangential shear exsit, the relation of ε_{nc} and σ_n in simple shear test can be considered equal to the relation in oedometric compression test. Experimental evidence show that the oedometric compression curve can be fit by exponential function, and described as: $\varepsilon_{nc}= t_1(1-e^{-t2\sigma n})$, Further, differentiating the function and comparing with Eq. (1), we can get:

$$C_{11} = t_1 t_2 e^{-t_2 \sigma_n} \tag{8}$$

where t_1 and t_2 are test parameters obtained by oedometric compression test.

Characters of Normal Dilatancy

Based on the schematic sketch shown in Fig.2, normal dilatancy ε_{ns} can be separated from ε_n and its expression is $\varepsilon_{ns}=\varepsilon_n-\varepsilon_{nc}$. The relation curve of normal strain and tangential strain also can be fitted in subsection by quadratic function and hyperbolic secant function. The functions are given as follow:

$$\varepsilon_{ns} = \begin{cases} m\gamma + n\gamma^2 & 0 \le \gamma \le \gamma_2 \\ \varepsilon_{ns\min} + (\varepsilon_{ns\max} - \varepsilon_{ns\min}) \sec h\left[S_2(\gamma - \gamma_2)\right] & \gamma > \gamma_2 \end{cases} \tag{9}$$

where γ_2 is the strain responding to the maximum normal compression, m and n are the parameters of parabola model, ε_{nsmax} is the maximum normal compression of ε_{ns}, ε_{nsmin} is the minimum normal compression of ε_{ns}, and S_2 is a parameter of the model governing the shape of the curve in dilation segment and it can be derived by the procedure like S_1 described in the previous section. According to the parabola equation character, we have: $m=2\varepsilon_{nsmax}/\gamma_2$, $n=-\varepsilon_{nsmax}/\gamma_2^2$. Generally, γ_2 and ε_{nsmax} occurred in the initial stage in which the incremental of normal stress is limited. Fitting the relation of $\gamma_2 \sim \lg(\sigma_0/p_a)$ and $\varepsilon_{nsmax} \sim (\sigma_0/p_a)$, we get the relation :

$$\gamma_2 = e_2 + f_2 \lg(\sigma_0 / p_a), \quad \varepsilon_{ns\max} = e_3 + f_3(\sigma_0 / p_a)$$

where e_2, e_3, f_2 and f_3 are fitting parameters. While the ε_{nsmin} occurred in the failure stage, and experimental evidence shows that the relationship between ε_{nsmin} and (σ_f/p_a) can be approximating fitted by straight line, and the expression is:

$$\varepsilon_{ns\min} = e_4 + f_4(\sigma_f / p_a) = e_4 + f_4\left[\left(c + \sigma_0\eta\right)/\left((\eta - \tan\varphi)p_a\right)\right]$$

where e_4 and f_4 are fitting parameters. Further, differentiating Eq. (9) , we can get:

$$d\varepsilon_{ns} = \begin{cases} (m + 2n\gamma)d\gamma & 0 \le \gamma \le \gamma_2 \\ -\dfrac{S_2(\varepsilon_{ns\max} - \varepsilon_{ns\min})}{\cosh\left[S_2(\gamma - \gamma_2)\right] \cdot \coth\left[S_2(\gamma - \gamma_2)\right]} d\gamma & \gamma > \gamma_2 \end{cases} \tag{10}$$

Considering the Eq. (11), we have Eq.(12-14).

$$d\varepsilon_{ns} = \frac{\partial \varepsilon_{ns}}{\partial \tau} d\tau = \frac{\partial \varepsilon_{ns}}{\partial \gamma} \frac{\partial \gamma}{\partial \tau} d\tau \tag{11}$$

$$C_{12} = \frac{(m + 2n\gamma)}{a\eta^2 \sigma_0 \left[(\eta\sigma_0 + (1 - b\eta)\tau)\right]^2} \qquad 0 \le \gamma \le \gamma_2 \tag{12}$$

$$C_{12} = -\frac{S_2(\varepsilon_{ns\max} - \varepsilon_{ns\min})(\eta\sigma_0 + \tau)^2}{a\eta^2\sigma_0 \cosh\left[S_2(\gamma - \gamma_1)\right] \cdot \coth\left[S_2(\gamma - \gamma_1)\right]\left[(\eta\sigma_0 + \tau)/(\eta\sigma_0 + (1 - b\eta)\tau)\right]^2} \quad \gamma_2 < \gamma \le \gamma_1 \quad (13)$$

$$C_{12} = \frac{S_1 S_2(\varepsilon_{ns\max} - \varepsilon_{ns\min})(\alpha_f - \alpha_r)(c + \sigma_0\eta)}{(\eta - \tan\varphi)\cosh\left[S_2(\gamma - \gamma_1)\right]\coth\left[S_2(\gamma - \gamma_1)\right]\cosh\left[S_1(\gamma - \gamma_2)\right]\coth\left[S_1(\gamma - \gamma_2)\right]} \quad \gamma > \gamma_1 \quad (14)$$

There are 7 parameters more required to duplicate the relation of normal dilatancy and tangential shear stress which are e_2, e_3, e_4, f_2, f_3, f_4 and S_2. All the parameters can be defined by simple shear experimental tests.

Hereto, nonlinear elastic coupling constitutive model was completely defined to describe the soil-structure interface deformation behavior of strain softening and dilatancy under CSIRSP, and all parameters can be derived from experimental tests.

MODEL VERIFICATION

The interface orthogonal tests (σ_0= 50,100,200,400kPa, η= 1.0, 2.0, 4.0, φ) between coarse sand and rough steel are conducted to verify the validity of the proposed model. The sample shape is cylinder type with the size of 300mm in diameter and 40mm in height. The sample compactness is controlled in 0.8. Table1 shows the physical properties parameters of test sand. The model parameters are derived according to the test results, and are listed in Table2. The predicted results (η= 1.0 and 4.0) are show in Fig.3 together with the experimental results. It can be seen that the model is able to reproduce the behavior of soil-structure interface under different CSIRSP.

Table1. Physical Properties Parameters of Test Sand

name	D_{50}/mm	C_u	C_c	G_s	e_{max}	e_{min}
coarse sand	0.70	10.22	1.82	2.62	0.72	0.40

Table2. Values of the Constitutive Parameters Used for the Numerical Study

t_1	t_2	K	n	c /kPa	φ/°	ϕ/°	S_1	S_2
0.056	-0.04	41.69	0.45	0	35.4	33.1	10.27	6.28
e_1	e_2	e_3	e_4	f_1	f_2	f_3	f_4	
0.223	0.029	0.072	-1.68	0.396	0.025	0.015	0.168	

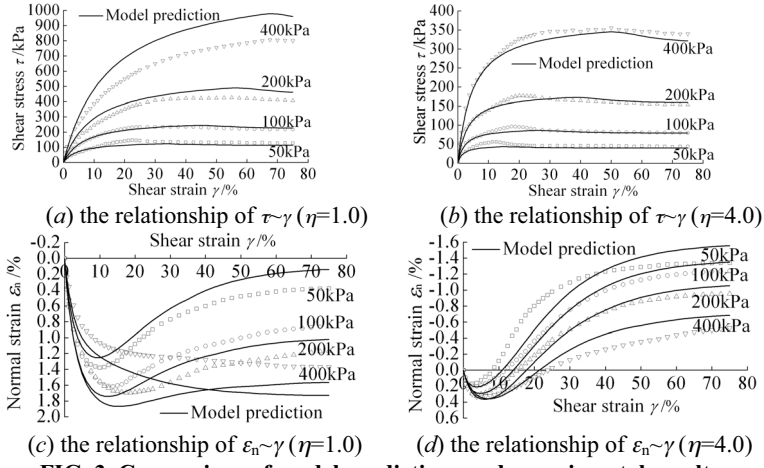
CONCLUSIONS

This paper has proposed nonlinear elastic coupling constitutive model for soil-structure interface between soil and rough structure. The main features of the model are as follow:

(1) The presented model can describe the deformation character of strain softening and dilatancy, as well as the effect of CSIRSP.

(2) Hyperbolic function and hyperbolic secant function were adopted to piecewise fit the curve of shear stress to shear strain. The dilatancy curves were also fitted by quadratic function and hyperbolic secant function in segment. Hyperbolic secant function can well reproduce the curve in segment of softening and dilatancy.

(3) The parameters of the model have clear physical meanings and can be identified rather easily following a series of procedure according to the test results.



(*a*) the relationship of τ~γ (η=1.0) (*b*) the relationship of τ~γ (η=4.0)

(*c*) the relationship of ε_n~γ (η=1.0) (*d*) the relationship of ε_n~γ (η=4.0)

FIG. 3. Comparison of model predictions and experimental results

REFERENCES

Boulon M., Nova R. (1990). Modelling of soil -structure interface behavior: a comparison between elastoplastic and rate type laws. *Computers and Geotechnics*, 9:21 26.

Desai C.S., Drumm E.C., Zaman M.M.(1985). "Cyclic testing and modeling of interface." *Journal of Geotechnical engineering, ASCE*, 111(6):793–815.

Gennaro V.D., Frank R.(2002). " Elasto-plastic analysis of the interface behavior between granular media and structure." *Computers and Geotechnics*, 29:547–572.

Lu T.H., Bao F.B.(2000). "A coupled constitutive model for interface thin-layer element". *Hydraulic Engineering*, 2:71–75.

Luan M.T., Wu Y.J. (2004). A nonlinear elasto -perfectly plastic model of interface element for soil -structure interaction and its applications. *Rock and Soil Mechanics*, Vol. 25(4):507-513.

Wang W., Lu T.H., Sun,B.X.(2007). "Mathematical model of shear stress-strain relationship of soil-concrete interface during shear fracture." *Key Engineering Materials*, (348-349): 881-884

Zhou A.Z., Lu T.H. (2008). "Elasto-plastic constitutive model of interface under generalized potential theory." *Chinese Journal of Geotechnical Engineering*, Vol. 30 (10): 1532-1536.

Zhou A.Z., Lu T.H., WU S.L.(2008). "Mechanical characteristics analysis of soil-structure interface by simple shear test under constant stress increment ratio stress paths." *Advances in Science and Technology of Water Resources*, Vol. 28 (5): 32-35.

A Dynamic Damage Statistical Constitutive Model of Rock Considering Strain Rate under Uniaxial Loading Conditions

Heng Zhao[1], Wen-Gui Cao[2] and Ling Zhang[3]

[1]Ph.D, College of Civil Engineering, Hunan University, Changsha, China, 410082; tridept@163.com
[2]Professor, College of Civil Engineering, Hunan University, Changsha, China, 410082
[3]Ph.D candidate, College of Civil Engineering, Hunan University, Changsha, China, 410082

ABSTRACT: Considering the dynamic deformation characteristics of rock and introducing the Kelvin model which consists of a viscous element and a paralleled elastoplastic element, a mechanical analysis model for rock under uniaxial loads is developed. This new model can take the influence of loading speed (or strain rate) and the dynamic behavior of rock into account. Based on that, with consideration of the influence of strain rate and volume change, a damage statistical constitutive model with the property of visco-elastoplastic is proposed by the statistical damage theory. Moreover, a method to determine the model parameters is presented. Finally, the proposed model is used to a practical problem, whose theoretical results are illustrated and compared to those of experiments. It is shown that the proposed constitutive model is effective to describe the characteristics of strength and elastic modulus of rock increasing with the increase of strain rate, and to simulate the dynamic deformation process of rock in uniaxial stress state.

INTRODUCTION

Currently, many efforts have been done to study the dynamic mechanical behavior of rock using light gas gun (Seamen *et al*.,1976) and spilt Hopkinson pressure device (SHPB) (Kolsky 1949), and the deformation mechanism of rock under the dynamic load has been recognized. Most experimental results describe the influence of loading speed or strain rate on dynamic properties of rock. However, the knowledge about the constitutive model of rock regarding the mechanical behavior in dynamic loading conditions appears to be absent, and there are only two types of models used to simulate the dynamic deformation process of rock: one is the dynamic constitutive model considering energy transition (Xin *et al.*, 1996). But this model has many

parameters to determine and the calculation process is complex. The other one is established on the regression analysis of the dynamic stress-strain relationship from the experiments (Li *et al*., 2001; Gao *et al*., 2000). This empirical model only can describe the stress-strain characteristics under a specific loading speed or a specific strain rate condition, and it is apparently inappropriate in the case of rock under different loading speed or strain rate.

The purpose of this paper is to developed a new model for rock under uniaxial loads by employing the Kelvin model to describe the deformation behavior under dynamic loads and the damage statistical theory (Krajcinovic *et al*.,1982) to treat the damage process and failure characteristic of rock. Moreover, the method to determine the model parameters is going to be presented and the effects of voids or volume changes on the dynamic behavior of rock are going to be discussed.

VISCO-ELASTOPLASTIC CONSTITUTIVE MODEL FOR UNIAXIAL LOADING CONDITIONS

Since the mechanical model of rock is the key to develop a method to simulate the dynamic deformation process of rock with taking the influence of loading speed or strain rate into account, an analytical model for the rock in uniaxial stress states is proposed based on the Kelvin model. As shown in FIG. 1, this analytical model is the parallel connection of a viscous element used to describe the effect of loading speed and strain rate and an elastoplastic element used to characterize the linear and nonlinear properties. The expressions of the stress and strain of the presented model are shown as follows:

$$\begin{cases} \sigma_1 = \sigma_{ep1} + \sigma_{v1} \\ \varepsilon_1 = \varepsilon_{ep1} = \varepsilon_{v1} \end{cases} \tag{1}$$

where σ_1 and ε_1 are the axial stress and strain of rock, respectively. σ_{ep1} and ε_{ep1} represent the axial stress and strain of the elastoplastic element, respectively. σ_{v1} is the axial stress of viscous element and ε_{v1} the corresponding axial strain. The constitutive relationship between σ_{v1} and ε_{v1} can be expressed as (Chen *et al*., 1998):

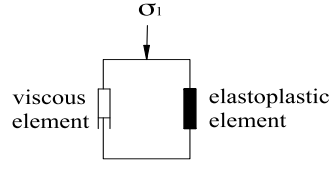


FIG. 1. Simplified analytical mode of rock deformation

$$\sigma_{v1} = \eta \, \mathrm{d}\varepsilon_{v1}/\mathrm{d}t \tag{2}$$

in which η is the viscosity coefficient; $\mathrm{d}\varepsilon_{v1}/\mathrm{d}t$ is the strain rate describing the loading speed of rock in uniaxial stress conditions. From Eq. (1), the development of dynamic constitutive model of rock under the uniaxial compression is dependent on the determination of the relationship between σ_{ep1} and ε_{ep1} of elastoplastic element.

Damage Constitutive Model of Elastoplastic Element

According to the damage statistical theory and the work did by Cao *et al*. (2007), the elastoplastic element of rock is supposed to divided into three parts: voids, an undamaged or intact part and a damaged part. The load is assumed to be only supported by the undamaged part, and the following equation is then given as

$$\sigma_{ep1} = (1-n)\sigma_{ep1}'(1-D) \tag{3}$$

where σ_{ep1} is the macroscopic stress (applied stress); σ'_{ep1} is the microscopic stress (net stress); D is the damage variable; and n is the void ratio which consists of the initial voids and the new growing voids and describes the tendency of voids changes during dynamic loading process, which can be determined by (Cao *et al*., 2007):

$$n = (n_0 - \varepsilon_v)/(1-\varepsilon_v) \tag{4}$$

in which, $\varepsilon_v=\varepsilon_1+\varepsilon_2+\varepsilon_3$. In the uniaxial loading case, $\varepsilon_2=\varepsilon_3$, so $\varepsilon_v=\varepsilon_1+2\varepsilon_3$.

Determination of Microscopic Stress σ'_{ep1}

As σ'_{ep1} is considered as the microscopic stress acting on the undamaged part of the elastic plastic body, it is assumed to be following the Hooke's law:

$$\sigma'_{epi} = E\varepsilon'_{epi} + \mu(\sigma'_{epj} + \sigma'_{epk}) \tag{5}$$

where i, j, k=(1, 2, 3), (2, 1, 3), (3, 1, 2). ε'_{epi} is the microscopic strain; E and μ are the elastic modulus and Poisson's ratio, respectively. By using the strain equivalence hypothesis (Krajcinovic *et al*., 1982) and equation (1), it obtains

$$\varepsilon'_{ep1} = \varepsilon_{ep1} = \varepsilon_1 \tag{6}$$

Since $\sigma'_{ep2}= \sigma'_{ep3}=0$, following relationship is obtained from Eqs. (5) and (6):

$$\varepsilon_2 = \varepsilon'_{ep2} = -\mu\varepsilon_1; \quad \varepsilon_3 = \varepsilon'_{ep3} = -\mu\varepsilon_1 \tag{7}$$

Substituting Eqs. (4)-(7) into Eq. (3), σ_{ep1} can be given as

$$\sigma_{ep1} = \frac{E\varepsilon_1(1-n_0)(1-D)}{1-(1-2\mu)\varepsilon_1} \tag{8}$$

Damage Evolution Equation of Elastoplastic Element

The damage variable D, which is important to develop the constitutive model with Eq. (8), can be determined by the damage statistical theory (Tang *et al*., 1998, and Cao *et al*. ,1998), in which the strength and distribution function of the mesoscopic elements should be determined.

(1) Determination of mesoscopic element strength

According to the Drucker-Prager criterion, the general strength form of mesoscopic element is expressed as

$$F = \alpha_0 I_1 + \sqrt{J_2} - k_0 \tag{9}$$

where I_1 is the first stress invariant; J_2 the second deviatoric stress invariant; α_0 and k_0

are material constants. In the uniaxial stress states, the above parameters can be calculated by follows:

$$I_1 = \sigma'_{ep1} \tag{10}$$

$$\sqrt{J_2} = \sqrt{3}\sigma'_{ep1} / 3 \tag{11}$$

$$\alpha_0 = \sin\varphi / \sqrt{9 + 3\sin^2\varphi} \tag{12}$$

$$k_0 = 3c \cdot \cos\varphi / \sqrt{9 + 3\sin^2\varphi} \tag{13}$$

where c denotes the cohesion; φ the internal friction angle.

Substituting Eqs. (10)-(13) into (9) gets

$$F = (\sqrt{3}/3 - \alpha_0) E\varepsilon_1 - k_0 \tag{14}$$

(2) Evolution equation of elastoplastic element

Assuming strength of mesoscopic elements observes Weibull distribution function, the evolution equation of the elastoplastic element is:

$$D = 1 - \exp[-(F/F_0)^m] \tag{15}$$

Visco-elastoplastic Constitutive Model under the Uniaxial Loads

Substituting Eq. (15) into Eq. (8) produces

$$\sigma_{ep1} = \frac{(1-n_0)E\varepsilon_1\left\{1-\exp[-(F/F_0)^m]\right\}}{1-(1-2\mu)\varepsilon_1} \tag{16}$$

Substituting Eqs. (2), (16) into Eq. (1), the visco-elastoplastic damage statistical constitutive equation describing the dynamic deformation process under the uniaxial compression for rock is obtained as follow:

$$\sigma_1 = \frac{(1-n_0)E\varepsilon_1\left\{1-\exp[-(F/F_0)^m]\right\}}{1-(1-2\mu)\varepsilon_1} + \eta\frac{\mathrm{d}\varepsilon_1}{\mathrm{d}t} \tag{17}$$

DETERMINATION OF MODEL PARAMETERS

m, F_0 and η are the three calculation parameters in Eq. (17) and can be determined by extremum theory as a complete stress-strain curve of rock under the dynamic loads has a peak point. The tangent slope of the peak point is 0, so following equation is existed:

$$\left(\mathrm{d}\sigma_1/\mathrm{d}\varepsilon_1\right)\Big|_{\sigma_1=\sigma_{dc},\,\varepsilon_1=\varepsilon_{dc}} = 0 \tag{18}$$

where σ_{dc} and ε_{dc} are the axial stress and strain at the peak point in the σ_1-ε_1 curve.

Supposing that $\mathrm{d}\varepsilon_1/\mathrm{d}t$ is a constant, substituting $\sigma_1=\sigma_{dc}$ and $\varepsilon_1=\varepsilon_{dc}$ into Eq. (17), and combining this result with Eq. (18) yields

$$m = \frac{F_{\mathrm{dc}} L_1^{\mathrm{dc}}}{A L_2^{\mathrm{dc}} (1 - D_{\mathrm{dc}}) \ln(1 - D_{\mathrm{dc}})} \tag{19}$$

$$F_0 = \frac{F_{\mathrm{dc}}}{[-\ln(1 - D_{\mathrm{dc}})]^{1/m}} \tag{20}$$

$$\eta = \left(\sigma_{\mathrm{dc}} - \sigma_{\mathrm{ep1}}^{\mathrm{dc}}\right)\left(\mathrm{d}\varepsilon_1 / \mathrm{d}t\right)^{-1} \tag{21}$$

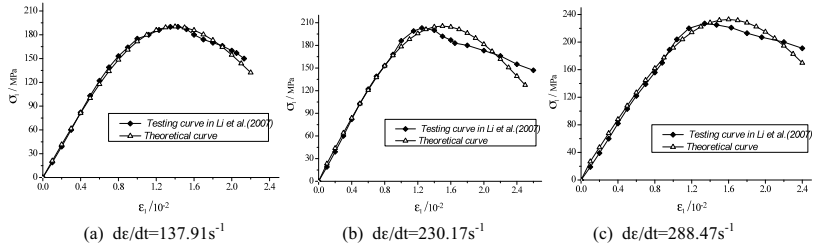
in which, $L_1^{\mathrm{dc}} = \dfrac{E(1-n_0)(1-D_{\mathrm{dc}})}{\left[1-(1-2\mu)\varepsilon_{\mathrm{dc}}\right]^2}$; $L_2^{\mathrm{dc}} = -\dfrac{E\varepsilon_{\mathrm{dc}}(1-n_0)}{1-(1-2\mu)\varepsilon_{\mathrm{dc}}}$; $F_{\mathrm{dc}} = A\varepsilon_{\mathrm{dc}} - k_0$;

$D_{\mathrm{dc}} = 1 - \dfrac{\left(\sigma_{\mathrm{dc}} - \eta \dfrac{\mathrm{d}\varepsilon_1}{\mathrm{d}t}\right)\left[1-(1-2\mu)\varepsilon_{\mathrm{dc}}\right]}{E\varepsilon_{\mathrm{dc}}(1-n_0)}$; $\sigma_{\mathrm{ep1}}^{\mathrm{dc}} = \dfrac{E\varepsilon_{\mathrm{dc}}(1-n_0)(1-D_{\mathrm{dc}})}{1-(1-2\mu)\varepsilon_{\mathrm{dc}}}$.

Note that the peak values σ_{dc} and $\varepsilon_{\mathrm{dc}}$ in specific strain rate can be obtained according to the test data.

APPLICATION AND VERIFICATION

The practical example conducted by Li *et al.*(2007) is introduced to verify the rationality of the presented dynamic damage statistical constitutive model of rock and its method to determine model parameters. The mechanical parameters such as the elastic modulus E, the poisson's ratio μ, the internal friction angle φ, and the cohesion c are obtained from the experimental curves, they are 35.34GPa, 0.25, 30.52˚, 23.15MPa, respectively. The theoretical and experimental stress–strain curves are illustrated in FIG. 2. It is shown that the calculated results are found to agree satisfactory with the experimental data.



(a) dε/dt=137.91s^{-1} (b) dε/dt=230.17s^{-1} (c) dε/dt=288.47s^{-1}

FIG . 2. Comparison between experimental and theoretical curves

CONCLUSIONS

(1) A dynamic damage statistical constitutive model of rock with the property of visco-elastoplastic is proposed in uniaxial loading conditions, in which the effect of

strain rate and volume change can be correctly accounted for, and the method of determining its parameters is also presented.

(2) It is shown that with the increase of loading speed or strain rate, both the strength and elastic modulus of rock increase gradually.

(3) When the presented model is introduced to analyze a practical example, the calculated results tally closely with the experimental data.

ACKNOWLEDGMENTS

The authors gratefully acknowledge Li and his colleagues providing the experimental data in this paper. This work was partially supported by the National Natural Science Foundation of China under contract No. 50378036.

REFERENCES

Seamen L, Curran D. R., Shockey D. A.(1976). Computitonal models for ductile and brittle fracture. *Applied Physics Letters*, 47(11):4814-4826.

KOLSKY H. (1949).An investigation of the mechanical properties of materials at very high rates of loading. *Proceedings of the Physical Society*, 62(11):676-700.

Xin Li-tian, He Xiang,Su Min(1996). The mechnical properties of rocks under strong impact loading. *Chinese Journal of Geotechnical Engineering*, (6): 61-68.

Li Ning, Chen Wen-ling, Zhang Ping(2001). Deformation properties of jointed rock mass under dynamic cyclic loading. *Chinese Journal of Rock Mechanics and Engineering*, 20(1): 74-78.

Gao Wen-xue, Yang Jun, Huang Feng-lei(2000). The constitutive relation of rock under strong impact loading. *Journal of Beijing Institute of Technology*, 20(2): 165-170.

Krajcinovic D., Silva M. A. G.(1982). Statistical aspects of the continuous damage theory.*Int. J. Solids Structures,* 18(7),551-562.

Chen Qing-xuan, Wang Wei-xiang, Sun Ye, et al(1998). Rock mechanics and analysis of tectonic stress field.*Beijing: Geological Publishing House*.

Cao Wen-gui, Li Xiang, Liu Feng(2007). Discussion on strain softening damage onstitutive model for fissured rock mass. *Chinese Journal of Rock Mechanics and Engineering*, 26(12): 2488-2494.

Tang Chun-an. and Kou S. Q. Crack propagation and coalescence in brittle materials under compression. *Engineering Fracture Mechanics,* 1998, 61, 311-324.

Cao Wen-gui, Fang Zu-lie, Tang Xue-jun(1998). Study of statistical constitutive model for soft and damage rocks. *Chinese Journal of Rock Mechanics and Engineering*, 17(6):628-633.

Li Gang,Chen Zheng-han, Xie Yun, Zhu Wen-hua(2007). Test research on dynamic characteristics of Three Gorges granite under high strain rate. *Rock and soil mechanics*, 28(9):1833-1840.

The Application of PFWD in Sub-grade Compactness Test

Peng Wang[1] and Chengchao Gua[1]

[1] School of Water Conservancy and Environment Engineering, Zhengzhou University, Mail: Wenhua road 97#,Zhengzhou,PR China,450002;PH (86)0371 638-87062; e-mail: wp@ha.edu.cn

ABSTRACT: Controlling compactness can increase sub-grade capability of resisting deformation and improve the pavement structure strength and stiffness. Portable Falling Weight Deflector (PFWD) has many advantages than the traditional method of testing sub-grade strength. The paper introduces the PFWD technical indexes and researches the PFWD performance in the sub-grade test. The paper research relations between deflector by PFWD test and compactness on the four sub-grade type，include low liquid limit clay soil and difference proportion cement stabilized soil. The result proves the better linearity relativity between deflector by PFWD test and compactness. The correlation formula between the back-calculate modulus and compactness is educed. Sub-grade compactness can be effectively controlled by PFWD rapid test. The paper provides the new test method and foundation for rapidly and objectively testing compactness. It is practical and theoretical significance for enriching the actual guide regulation。

INTRODUCTION

There are seventy percents up to ninety percents due to the sub-grade deformation in the deformation of the highway structure. So it is important to improve the anti-deformation properties for improving the whole structure strength and stiffness in construction. These requests are often achieved by controlling the compactness. Literature review indicated that there is an “index” relationship between the compactness and the service life, which makes people pay more attention to the compactness that should be reached or in fact is reached. Up to now, the method of testing compactness is the traditional method of “filling sand in the hole”. Many shortages such as requesting more operators, more human factors, lower efficiency exist in this method.

Portable Falling Weight Deflector (short for PFWD) is a new dynamic testing equipment, which follows the FWD using for testing on the sub-grade and the ground. It can get the dynamic resilience modulus of the sub-grade. The equipment has several advantages such as higher efficiency, less operators, nondestructive and a longer service life as well as the FWD, but it also has the advantages as follows:

small and light, reaching the place which other equipment can't, objective tested data, high precision, easy operation and costing less than other equipments.

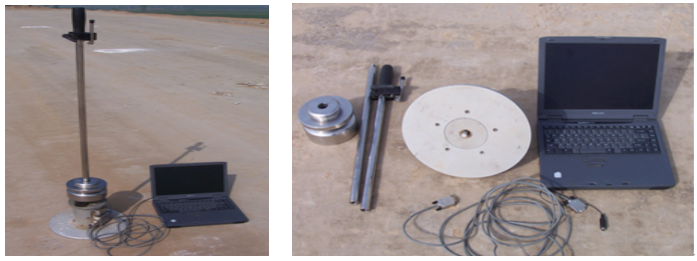


FIG. 1. Portable Falling Weight Deflector

EXPERIMENTAL RESEARCHES ON THE REPEATABILITY OF PFWD

The key of using PFWD testing the resilience modulus of the sub-grade is collecting the data of load and deflection with load sensors and displacement sensors. And the stability of the data is important for the calculation in next step. The same load hammer is used to hammer several times to see whether the loading value and the dynamic value are consistent with. And this experiment is used for testing the stability property of the sensors.

150mm radius of a bearing plate, an 850mm high pole and a 10 kg weigh hammer are used in the repeatability experiment. The PFWD loads on the surface of the sub-grade directly while the experiment is being done. The same high hammer loads on the same point with several times (usually 5-7times), and the value of the load and displacement tested by the displacement sensors. The value of the PFWD repeatability experiment on the sub-grade surface of a highway is listed as table 1 and table 2 in appendix.

Tables 1 and 2 show that: 1) average Standard deviation value of the load sensors are 2.3493 and 2.0891 ,which are small, while the PFWD testing on the sub-grade with 7.5:92.5 cement stabilized soil and on the sub-grade with pure soil. Coefficient Of variation value of the load on the sub-grade with pure soil is between 0.0042 and 0.0472; and Coefficient Of variation value of the load on the sub-grade with cement stabilized soil is between 0.0006 and 0.0321, it is smaller than 0.05. 2) Average Standard deviation value of the deflection sensors on the sub-grade with pure soil and the sub-grade with cement stabilized soil are 41.8525 and 43.1606, which are much smaller than the measurement. Coefficient Of variation value of the deflection on the sub-grade with pure soil is between 0.0223 and 0.0976; and Coefficient Of variation value of the deflection on the sub-grade with cement stabilized soil is between 0.0131 and 0.0960,it is smaller than 0.1. Therefore, the stability of the equipment is excellent.

Table 1. Repeatability experiment with PFWD on the sub-grade with 7.5:92.5 cement stabilized soil

Serial number	load	Standard deviation	Coefficient Of variation	Average deflection	Standard deviation	Coefficient Of variation

1	137.5620	2.2799	0.0166	655.5640	16.6745	0.0254
2	134.2020	2.6450	0.0197	698.7680	37.2329	0.0533
3	139.9060	2.6088	0.0186	612.7250	63.4147	0.1035
4	137.8939	2.3397	0.0170	714.8530	18.6929	0.0261
5	141.0516	0.0911	0.0006	635.6250	17.9974	0.0283
6	140.3246	1.3620	0.0097	714.0020	31.5858	0.0442
7	135.1068	2.3648	0.0175	589.6270	56.6114	0.0960
8	135.1968	2.4419	0.0181	713.6960	27.8120	0.0390
9	142.0000	1.5252	0.0107	748.8500	26.9141	0.0359
10	136.0000	3.2040	0.0236	610.3690	39.4450	0.0650
11	132.7500	3.5340	0.0266	759.9470	17.2650	0.0230
12	136.3577	1.5621	0.0115	685.6230	8.9814	0.0131
13	137.5968	1.4456	0.0105	757.5360	35.6053	0.0470
14	139.1488	2.4563	0.0177	710.3170	117.5410	0.1650
15	138.9465	4.4613	0.0321	642.7500	97.0111	0.1509
16	137.0657	3.3631	0.0245	626.3860	56.8873	0.0783
17	137.8054	2.2531	0.0164	950.5500	64.0586	0.0674
Average Value	137.5832	2.3493	0.0171	695.7169	43.1606	0.0624
Minimum value	132.7500	0.0911	0.0006	589.6270	8.9814	0.0131
Maximum value	142.0000	4.4613	0.0321	950.5500	227.8120	0.0960

Table 2. Repeatability experiment with PFWD on the sub-grade with pure soil

Serial number	load	Standard deviation	Coefficient Of variation	Average deflection	Standard deviation	Coefficient Of variation
1	137.1195	1.2113	0.0088	716.5232	55.2130	0.0771
2	130.5543	3.2583	0.0250	750.8593	52.4868	0.0699
3	136.1175	3.6406	0.0267	737.0182	34.0965	0.0463
4	131.5879	1.6018	0.0122	619.5281	22.8813	0.0369
5	129.5238	1.7997	0.0139	589.4724	63.1935	0.1072
6	123.4581	1.8715	0.0152	1389.6074	103.8793	0.0748
7	132.0557	6.2332	0.0472	565.7864	12.6198	0.0223
8	123.5213	0.5127	0.0042	932.3972	19.9340	0.0214
9	133.4844	0.9885	0.0074	805.0619	38.5634	0.0479
10	126.5810	2.0173	0.0159	715.1465	44.3339	0.0620
11	127.2575	1.5020	0.0118	721.7051	20.1674	0.0279
12	134.2747	0.8593	0.0064	593.4128	22.9318	0.0386
13	131.0632	2.7983	0.0214	673.0286	65.6743	0.0976
14	129.9316	0.9211	0.0071	563.0540	23.1643	0.0411
15	133.7784	2.0048	0.0150	650.9201	28.4077	0.0436
16	128.6799	3.1904	0.0248	788.8808	76.4852	0.0970
17	132.4477	1.1044	0.0083	989.5933	27.4599	0.0277
Average Value	130.6727	2.0891	0.0160	753.0586	41.8525	0.0553
Minimum value	123.4581	0.5127	0.0042	563.0540	12.6198	0.0223
Maximum value	137.1195	6.2332	0.0472	1389.6074	127.4599	0.0976

COMPARATIVE ANALYSES ON THE COMPACTNESS AND THE DEFLECTION TESTED WITH PFWD

The values tested with PFWD and by the method of "filling sand in the hole" during the construction process, which is collected on the sub-grade with pure soil, the sub-grade with cement stabilized soil and the sub-grade with cement and lime stabilized soil, was illustrated in the table and figure in order to find the relationship of compactness and deflection intuitively.

Linear correlation equations as follows:

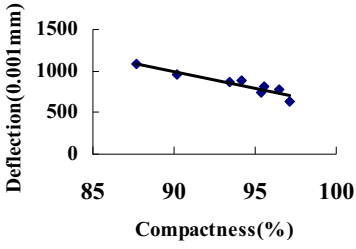
Low liquid limit clay soil: $y=-39.915x+4587.1$ ($n=8$, $R^2=0.8843$) (1)
5:95 cement stabilized soil: $y=-46.257x+5151.8$ ($n=8$, $R^2=0.9650$) (2)
7.5:92.5 cement stabilized soil: $y=-51.704x+5669.6$ ($n=8$, $R^2=0.9099$) (3)
Cement and lime stabilized soil: $y=-23.911x+3114.0$ ($n=8$, $R^2=0.8150$) (4)

In the equation:
y—deflection value tested with PFWD (unit:0.001mm);
x—compactness value tested by the method of "filling sand in the hole" (unit:%).

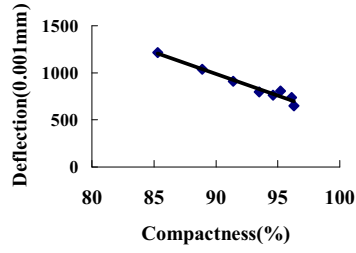
The square of the correlation coefficient is more than 0.8 in the four linear equations, and the values which focus on the sub-grade with 5:95 cement stabilized soil is up to 0.965. It suggests that the deflection value detected by PFWD have a good linear correlation with the field compactness.

Table 3. Correlation of compactness value and deflection value tested on four types of sub-grade

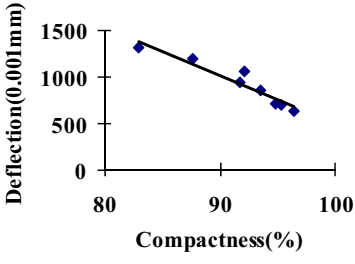
pure soil		5:95 cement stabilized soil		7.5:92.5 cement stabilized soil		10:10:80 cement and lime stabilized soil	
compactness	deflection	compactness	deflection	compactness	deflection	compactness	deflection
87.7	1084.92	85.3	1215.67	82.9	1307.5	84.6	1097.14
90.2	957.2	88.9	1039.33	87.6	1188.5	90.5	987.5
94.2	893.07	91.4	908.25	91.7	938.75	91.3	888.33
95.6	812.54	93.5	798.33	93.5	853.64	93.8	812.15
96.5	771.12	94.6	763.55	94.8	712.33	94.2	848.83
97.1	638.21	96.3	650.67	96.4	634.5	96.1	854.72
95.4	735.31	96.1	739.67	95.3	700.5	95.8	793.5
93.4	864.64	95.2	808.5	92.1	819.0	94.6	913.5



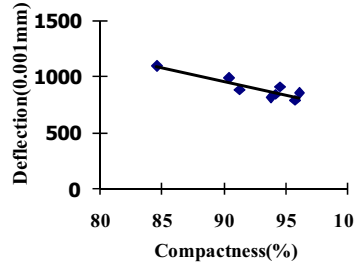
a) sub-grade with pure soil



b) sub-grade with 5:95 cement stabilized soil



c) sub-grade with 7.5:92.5 cement stabilized soil



d) sub-grade with 10:10:80 cement and lime stabilized soil

FIG. 2. The correlation of compactness value and deflection value tested on four types of sub-grade

COMPARATIVE ANALYSES ON THE MODULUS AND COMPACTNESS TESTED WITH PFWD

The modulus of the sub-grade with different compactness was tested with PFWD in the four fields during the pavement construction. The modulus changes with the different compactness were listed in the table 4. The relationship of them was analyzed and a correlation function was found between them.

Table 4. The correlation of compactness value and modulus value back-calculated on four types of sub-grade

pure soil		5:95 cement stabilized soil		7.5:92.5 cement stabilized soil		10:10:80 cement and lime stabilized soil	
compactness	modulus	compactness	modulus	compactness	modulus	compactness	modulus
87.7	35.4	85.3	28	82.9	25.75	84.6	32.29
90.2	40.9	88.9	34.75	87.6	32	90.5	42.00
94.2	43.9	91.4	47.83	91.7	42.5	91.3	43.28

95.6	43.9	93.5	44.75	93.5	41	93.8	42.28
96.5	44.71	94.6	44	94.8	51.5	94.2	45.61
97.1	50	96.3	55.75	96.4	55.5	96.1	47.8
95.4	46.81	96.1	47.83	95.3	55.33	95.8	44.6
93.4	45.87	95.2	45.36	92.1	45.8	94.6	43.2

Correlation equations between modulus and compactness was drawn from analysis the correlation relationship on the figure 3

Low liquid limit clay soil: $y=1.1932x-67.943$ ($n=8$ $R^2=0.8065$) (5)

5:95 cement stabilized soil: $y=1.9618x-138.25$ ($n=8$ $R^2=0.7997$) (6)

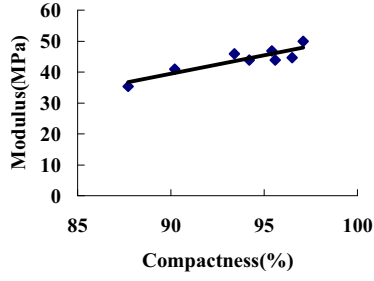
7.5:92.5 cement stabilized soil: $y=2.2559x-164.41$ ($n=8$ $R^2=0.8713$) (7)

Cement and lime stabilized soil: $y=1.0881x-57.925$ ($n=8$ $R^2=0.8042$) (8)

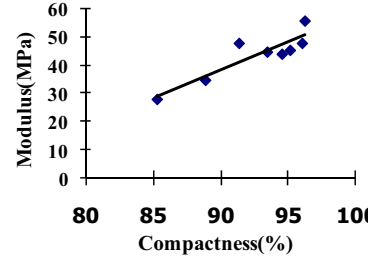
In the equation:

y-the modulus tested with PFWD;

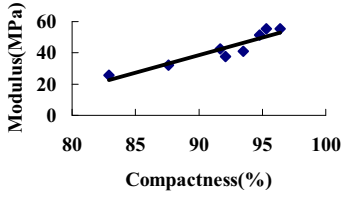
x-the compactness tested by the method of" filling sand in the hole".



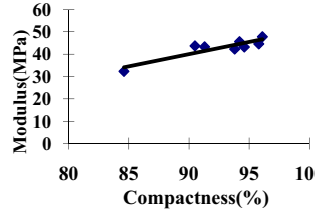
a)sub-grade with pure soil



b)sub-grade with 5:95 cement stabilized soil



c) sub-grade with 7.5:92.5 cement stabilized soil



d) sub-grade with 10:10:80 cement and lime stabilized soil

FIG. 3. The correlation relationship between the modulus and the compactness on the four types of sub-grades

The square of the correlation coefficient is more than 0.79 in the linear equation, so, the modulus and the compactness has a good correlation.

And the correlation tested on the sub-grade with7.5:92.5 cement stabilized soil is the best of all. The square of the correlation coefficient is up to 0.8713.

It is reliable to use the modulus tested by PFWD replacing the compactness tested by filling sand in the hole to evaluate the carrying capacity of the sub-grade and the construction quality.

CONCLUSIONS

Pavement nondestructive testing and material properties back-calculation are very active forefront problem in the world. And the research results are becoming richer and richer. On one side, the pavement design index (resilience modulus) and the pavement construction control index (compactness) aren't consistent each other in the design and construction specifications; on the other side, pavement resilience modulus of conventional detection technology has the shortages such as cumbersome test, long time cost, more operators, high price of device and uneasy to reach the remote place. So the study of new technologies on the pavement construction quality control has very important theoretical and practical significance. The main conclusions were drawn from the study as follows:

1、The relationship between deflection and modulus tested with PFWD and the field compactness is built through the testing by PFWD on sub-grade with pure soil, sub-grade with 5:95 cement stabilized soil, sub-grade with 7.5:92.5 cement stabilized soil and sub-grade with cement and lime stabilized soil. The experimental results suggest that: there is a good linear correlation between compactness and deflection and modulus tested with PFWD.

2、 The compactness could reach the value of 95% if the deflection tested on the sub-grade with pure soil reached the value of 796μm; The compactness could reach the value of 95% if the deflection tested on the sub-grade with 5:95 cement stabilized soil reached the value of 758μm; The compactness could reach the value of 95% if the deflection tested on the sub-grade with 7.5:92.5cement stabilized soil reached the value of 758μm; The compactness could reach the value of 95% if the deflection tested on the sub-grade with cement and lime stabilized soil reached the value of 843μm.

The compactness could reach the value of 95%,if the modulus tested on the sub-grade with pure soil reached the value of 46Mpa; The compactness could reach the value of 95% if the modulus tested on the sub-grade with 5:95 cement stabilized soil reached the value of 49Mpa; The compactness could reach the value of 95% if the modulus tested on the sub-grade with 7.5:92.5cement stabilized soil reached the value of 50Mpa; The compactness could reach the value of 95% if the modulus tested on the sub-grade with cement and lime stabilized soil reached the value of 46Mpa.

From above conclusion, we can obtain the compactness of the whole pavement according the deflection or modulus tested with PFWD. The compactness could reach the value of 95% if the deflection tested on the sub-grade reached the value of 750μm and modulus reached the value of 50 Mpa. We can unify the design control indexes and construction control indexes.

REFERENCES

1.Duan,Dan-Jun,Zha,Xu-Dong,Zhang,Qi-Sen(2004).”Sub-grade resilience modulus measuring by portable falling weighted deflector-meter.” *J. Journal of Traffic and Transportation Engineering.*2004,4(4): 10-12 .

2.Wang,Duan-Yi,Huang Geng, Zhu Yi-Ming(2002)” attempt on Sub-grade strength evaluated by portable falling weighted deflector-meter.” *J. Highway.* 2002,12(9): 108-110.

3.Livneh, M, Livneh, N, Elhadad, E(1997)”Determining a pavement modulus from portable FWD testing” *J.ASTM geotechnical testing journal* .1997, 20(4): 373-382.

4.Fu,Bo(2005).”PFWD application research on the old road rebuilt engineering.” *J. Highways& Automotive Applications.* 2005(4): 52-54.

Research on the Disturbed State Concept for Soft Clay Roadbed

Xiao-Jun Yu[1] and Jian-Yong Shi[2]

[1]Associate professor, post doctoral researcher , Department of Civil Engineering, Yancheng Institute of Technology, Huanghai Road, Yancheng City, China, Tel:0515-8168207; Fax:0515-8168215; flyingfish7101@126.com

[2]Professor, Institute of Geotechnical Engineering, Hohai University, Xikang Road, Nanjing City, China, Tel: 025-83787216; soft-ground@hhu.edu.cn.

ABSTRACT: With the rapid development of the economy in China, more and more highways and railways are being constructed in areas with soft soil. As a result, geotechnical engineers encounter many difficulties in dealing with stability and deformation problems of soft roadbeds. The significance of a disturbed state concept for soft clay is presented. Based on the tests, the preparation method of the soft clay samples with the different degrees of disturbance is illustrated. In addition, an electrical resistivity method is introduced to define and measure the disturbed variable, and a formulation for the development of disturbance is established. Also, an advanced disturbed state concept constitutive model is proposed. Finally, results from triaxial drained triaxial shear tests show that the advanced model can describe the stress-strain characteristics of soft clay.

BACKGROUND

Soft clay is distributed extensively in the costal areas and some inland areas of China. With the rapid development of the economy in China, more and more infrastructures are being constructed in soft soil areas. In this process, geotechnical engineers gain much experience in dealing with stability and deformation-control problems with regard to soft soils. However, due to its complexity, substantial difficulties are still encountered. For instance, a factory built in the Futian economic development zone, Shengzhen, collapsed due to large settlements as much as 400 mm. The A4-A5 section of the Lian-Xu express way near Lianyungang was pre-compacted with sand, gravel and lime-soil compaction piles. During the construction, cracks appeared, and the settlement was larger than expected. On the lefthand side of one of the soft soil sections, cracks, collapse and slides occurred. The largest crack is 8 cm wide, and the longest slide is about 40 cm. Large ecologic losses were the result. These problems occurred because the engineers did not recognize the problems of soft soil. When deformation calculations were made, traditional constitutive models were

used, leading to large differences to the actual deformations. It is difficult to master the deforming mechanism, and therefore difficult to estimate the final settlement, or make reasonable design and construction controls of settlement. The difference between the calculation using traditional constitutive models and the actual settlement depends on various factors. One of the most important is that in the traditional constitutive model the structure disturbance and damage are not considered.

RESEARCH TO DATE

Soil structure is one of the most important factors influencing the mechanical properties of a soil. When constructing a building, the soil often needs some improvement. This disturbs the soils, leading to a change in soil structure and thus stress-strain relationship. Engineering practice shows that disturbance of soils leads to extra settlement of the soil, and increases the settlement of a construction. Surcharge loading also results in some disturbance of soils, causing structure damages and even failure. The traditional constitutive models for soft soils seldom consider the effect of structure disturbance. This might be the reason that the calculated settlement is far from the actual values.

The influence of disturbance on the soil characteristics has been studied for a long time overseas. Recently, there have been several advancements on this topic in China (Sun, 2004; Wang, 2007).

The disturbed state concept (DSC) was first proposed by Desai (1974). It is based on the idea that a deformed material element can be treated as a mixture of two constituent parts. One the relative intact (RI)state and the other fully adjusted (FA) state as reference states. During surcharge loading, the material experiences internal changes in its microstructure due to self-adjustment. As a consequence, the initial RI state transforms continuously to the FA state. A disturbed function is needed to describe the development from RI to FA, i.e. the process of gradual disturbance and complete destruction.

Recently, geotechnical engineers actively explored the feasibility and applicability of DSC model. For example, Desai (1995) used a DSC model to describe the transformation process of a soil from its original structure to secondary one. In China, studies in this field have been carried only in recent years (Wu, 2002; Wang, 2004; Zhou , 2004).

In defining and determining the disturbance variables, some of the conventional tests such as mass - testing, volume testing, pore ratio testing, stress-strain testing and so on are not possible. This is because of lack of appropriate equipment, some are very complicated, while the others are too costly. The disturbance functions also have too many hypotheses or are very complicated in the calculations.

In this paper, first of all a new method of preparing and controlling disturbed samples is presented. Then, an approach called the electrical resistivity structural method is introduced to measure the disturbance variables and build the disturbance function. Finally, a formulation of disturbance development is established based on the triaxial compression tests and stress path tests.

EXPERIMENTAL INVESTIGATION

Background

Electrical resistivity is a basic soil parameter indicating electrical conductivity of soil, and it is one of the intrinsic parameters of soil. The application of electrical resistivity methods in studying the structural transition of a soil mainly depends on measuring the changes in electrical resistivity and the corresponding changes in the structural parameters, i.e. $\overline{F}$、 $\overline{f}$、A. Where $\overline{F}$ is the average formation factor reflecting porosity and pore structure of soil, $\overline{f}$ is the average shape factor describing the shape of particles, A is the anisotropy factor showing directional arrange of particle (Arulanandan and Muraleetharan,1988; Thevananyagam,1993).

Very few previous studies could be found with regard to the application of electrical resistivity method in studying disturbed constitutive model of soft clay. Most are focused on studying the soil structure. For instance, researchers found that the relationship between average formation and porosity can be utilized to estimate the change in porosity of soils with different cohesion and consequently, to probe the structural change of soils. (Arulmol and Arulanandan, 1994; Tumidajski et al., 1996). Based on the analysis of consolidation tests and triaxial shear tests, Yu, 2007 proposed a comprehensive structural parameter, $m=m_c/m_0$ that can be obtained from average formation factor and average shape factor as well as anisotropy factor, where m_c and m_0 are respectively $\overline{F}^2A/f$ of disturbed and undisturbed soils. Then, a structural elasto-plastic creep model was proposed and it fitted quite well to the triaxial drained shear tests on marine soft clay.

The above-mentioned results provide sound background for application of electrical resistivity method to the disturbed state theory.

Description of soil samples and testing procedure

The index properties of the undisturbed soft soil obtained from Lianyungang k14+700~k15+350 section are summarized in Table 1.

Table 1 Index properties of the soft soil

Depth/m	ω/%	ρ / g/cm^3	Gs	e	ω_l/%	ω_p/%	c'/kPa	Φ'/^{0}
4	65.4	1.68	2.64	1.68	82.2	29.0	2.0	13.4
6	73.0	1.63	2.76	1.93	87.6	28.9	3.0	13.4

The disturbed samples are obtained by inserting needles with waterproof and agglutinate-proof coat into undisturbed normative triaxial samples. The layout of inserted needle is shown in figure 1.

To study the feasibility of using mc to define and measure the disturbed variable of a sample, inserted needles, measurement of electrical resistivity and unconfined compression strength test are used. An apparatus called low frequency AC electrical bridge was used to measure the electrical resistivity of soil, which is shown in Fig.2.
To establish the disturbed function, the triaxial drained shear test with simultaneous electrical resistivity test is used.

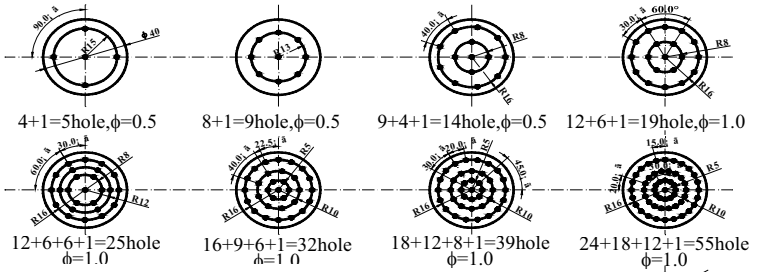


Fig.1 Layout of inserted needles

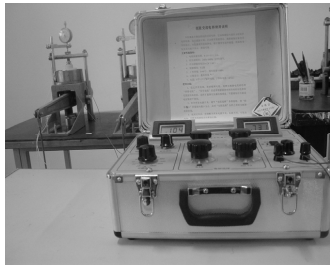


Fig. 2 Testing apparatus

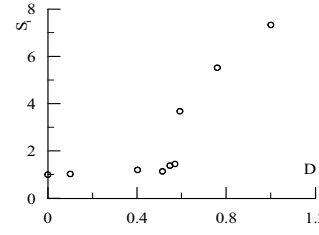


Fig.3 The relation between D and S_i

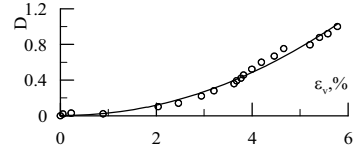


Fig.4a The relation between D and ε_v/25kPa

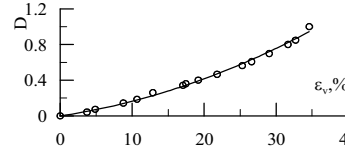


Fig.4b The relation between D and ε_v/50kPa

Testing results and discussion

1. Use m_c to define and measure disturbed variable of a sample.

The proposed form for the disturbed variable is given as :

$$D = (m_0 - m_c) / (m_0 - m_a) \quad (1)$$

Where m_0, m_c and m_a are respectively $\bar{F}^2 A / \bar{f}$ of undisturbed, disturbed and remolded samples. Fig. 3 shows the relationship between D and S_i, with $S_i = q_{u0}/q_{uc}$, where q_{u0} and q_{uc} are unconfined compression strength of undisturbed and disturbed samples respectively. D can be obtained from electrical resistivity. It can be seen that S_i increases with the development of D.

2. Establish disturbed function and disturbed development formulation.

Test results from triaxial drained shear show that there is good relationship between D and volumetric strain. Fig.4 illustrates the correlation of strain and disturbed function. The disturbed function can be expressed:

$$D = a\varepsilon_v^{\ 2} + b\varepsilon_v + c \quad (2)$$

Where D is disturbed variable; ε_v is volumetric strain; a、b、c are parameters of samples. Determination of the parameters a, b and c needs an optimum procedure involving triaxial drained tests and electrical resistivity tests.

Based on the probing needles test and stress path test, disturbed development formulation can be obtained as follows:

$$D=\frac{p_{mo}'-p_{mi}'}{p_{mo}'-p_{ma}'} \quad (3)$$ where p_{mo}'、p_{ma}'、p_{mi}' are shown in fig.5.

3、Constitutive model and model validation

When building a constitutive model for soft clay based on the DSC theory, the disturbed variable D is defined in equation 1 and measured by the means of electrical resistivity method. The disturbed function can be obtained from equation 2 using test results. Consequently, the advanced disturbed state concept constitutive model of soft clay can be deduced.

To investigate the validity of the advanced model, triaxial drained shear simulation tests on a soft soil from Lianyungang were carried out.

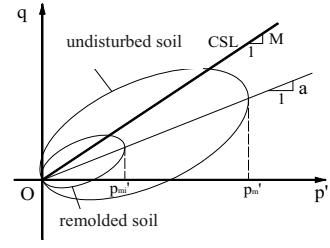


Fig.5 Yield curve for soft clay

The advanced model involves nine soil parameters, as shown in table 2, which can be determined from consolidation tests and triaxial drained tests.

Table 2 model parameters of soft clay from Lianyungang

parameters	e_0	K^i(kPa)	λ	κ	M	α_0	a	b	c
	1.681	522	0.439	0.032	0.77	0.45	0.03	-0.008	0.0066

$\boldsymbol{K^i}$ is the tangent volumetric modulus, and can be obtained from tangent inclination of the original elastic part of curve for volumetric strain and mean (effective) stress. M, λ, κ are basic parameters of S-CLAY1 model suggested by Wheeler et al. (2003). α_0 is rotational hardening variable, $\alpha_0=\eta_0=\frac{3(1-k_0)}{1+2k_0}$, where, η_0 is original stress ratio. The determination of the parameters a, b and c needs an optimum procedure, involving triaxial drained tests and electrical resistivity tests. With the optimized value of a, b, c, triaxial tests with synchronous electrical resistivity measurements on soils can be simulated.

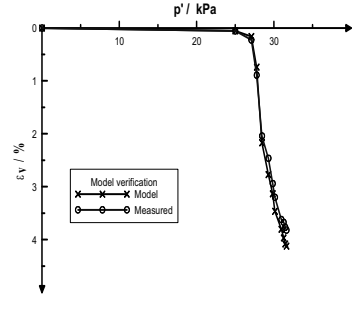


Figure 6 Validation of model

The model expression is given by

$$\varepsilon_v = [1-(0.03\varepsilon_v^2 - 0.008\varepsilon_v + 0.0066)]\times 0.0019p' + (0.03\varepsilon_v^2 - 0.008\varepsilon_v + 0.0066)\times[-1.31\times\ln(10.41 - 3.025\ln p')] \quad (4)$$

Figure 6 shows that the experimental data can be well predicted by the advanced model.

CONCLUSIONS

This paper illustrates the preparation of disturbed soil samples by the means of inserting needles. Electrical resistivity method is introduced to define and measure the disturbed variable. Stress-strain disturbed function is established based on the test results. The advanced disturbed state concept constitutive model of soft clay is proposed, and triaxial drained tests showed that the advanced model can basically reflect the deformation of soft clays and is satisfactory in its application.

ACKNOWLEDGEMENTS

This work was supported by Jiangsu province Science Technology Council (BK2007070). Thank Mr. Geoffrey Gay for his kind help in editing the paper.

REFERENCES

Arulanandan.K, Muraleetharan,K.1988, "Level Ground Soil Liquefaction Analysis Using in Situ Properties", *Journal of Geotechnical Eng.*Vol.114,No.7:753-789

Arulmoli.K, and Kandiah Arulanandan,1994, "review of an electrical method for evaluation of stress ratio required to cause liquefaction and dynamic modulus", *Dynamic Geotechnical Testing[J],* ASTM:118-130

Desai C S. 1974, "A consistent finite element technique for work softening behavior",Proc Int Conf On Computer Methods in Nonlinear Mechanics , University of Texas , Austin , TX

Desai C S. 1995, "Constitutive modeling using the disturbed state concept as microstructure self adjustment concept", *Continuum Models of Materials with Microstructre,* Muhlhaus HB(ed.) ,Chapter 8. Wiley :U K

SHUN Jun, 2004,"Theory of Soil Environment Stability and Deformation Control under Influence of Construction Disturbance", *Journal of Tongji University (Natural Science),* 32(10):1261-1269

Thevananyagam,S.,1993,"Electrical response of two-phase soil:Theory and applications" [J], *Journal of Geotechnical Engineering.,* Vol.119,No.8:1250-1275

Tumidajski and A.S.Schmnacher.et al.,1996, "On the relationship between porosity and electrical resistivity in cementitions systems" [J], *Cement and concrete research*, vol-26,No.4:539-544

WANG Guoxin, 2004, "Study of constitutive model of structural clay based on the disturbed state concept", *ACTA MECHANICA SOLIDA SINICA,* 25(2):191-197

WANG Li-zhong, LI Ling-ling, 2007, "Field disturbance of structured clay and its effect on settlements of soil foundation", *Chinese Journal of Geotechnical Engineering,* 29(5): 693-704

Wheeler, S.J., Näätänen, A., Karstunen, M. & Lojander, M, 2003, "An anisotropic elastoplastic model for soft clays", *Canadian Geotechnical Journal* 40:403-418

Wu Gang, 2002,"Disturbed state constitution models of engineering material(I)—

disturbed state concept and its theory principium", *Chinese Journal of Rock Mechanics and Engineering June,* 21(6):759-765

YU Xiaojun, 2007, "Research on application of electrical resistivity model theory to creep behaviors of marine soft soil", *Chinese Journal of Rock Mechanics and Engineering,* 26(8):1720-1727

ZHOU Cheng, SHEN Zhujiang, 2004, "A hypopla sticity disturbed state model for structured soils", *Chinese Journal of Geotechnical Engineering,* 26(4):435-439

Numerical Simulation of Soil-pile Interaction in Expansive Soils Foundation

Chun-Shun Zhang [1-2], Yong-He Wang[1], Hong-Bin Xiao[3], Zhen-Hui Fan[1]

[1] School of Civil Engineering and Architecture, Central South University, Shaoshan Road, Changsha, 41007, People's Republic of China; email: zhangchunshun@yahoo.com.cn
[2] Geotechnical Engineering Center, Sydney University, Darlington, NSW, 2006, Australia; email: C.Zhang@usyd.edu.au
[3] School of Civil Engineering, Hunan University of Technology, Wenhua Road, Zhuzhou, 410082, People's Republic of China

ABSTRACT: Analytic solution of load-transfer for single pile in expansive soil is completed based on shear-deformation method and superposition principle (Fan et al., 2007). As a complement of the research work, the numerical simulations have been done based on corresponding grogram in this paper. The results are shown as follows: increasing of pile length is able to effectively decrease the upward pile movement, but meanwhile, tensile forces of pile shaft increase as well; pile with small diameter ($d \approx 0.044L$) can effectively reduce the upward pile movements in expansive soils while those piles with the diameter over $0.045L$ contribute little if not in vain; the applied load that act on pile-top for preventing upward pile movement depend on maximum swelling force, varying from different pile length and influenced zone; As irrigation proceeds, both the pile shaft displacement and tensile force increase while the increments of the both keep decreasing at the same interval. Given enough time, soils' swelling tends to be stable and so do the displacements and tensile forces of the pile shaft

INTRODUCTION

Expansive soil interaction with pile is a much more complicated problem than other common clays since the soil deformation and strength changes with water contents. Simple and practical method would be preferred to deal with the problem compared to complicated theory. In previous work (Fan et al., 2007), basic theory and derivation of the pile-soil interaction problem had been established, being simple but accurate. As a complement work, numerical simulations have been done in this paper, resulting of several beneficial conclusions.

Mechanism of Pile-soil Interaction in Expansive Soils

Though the proceeding of the derivation of analytic solution to load-transfer for single pile in expansive soil under its swelling has been presented in detail (Fan et al., 2007), a summary is introduced as followings to provide a background:

Based on the assumption that no sliding occurs at the pile-soil interface given a small relative displacement, the pile-soil interaction in swelling soils are considered to be the superposition of the both cases: pile subjected to applied loads on the top and the pile subjected to the soils swelling force. The corresponding equations for both aspects are derived based on shear deformation method (Xiao, 2005; Wei et al., 1998; Aschenbrener, 1984) and the results are given in Equation 1 and 2, respectively:

$$\begin{cases} P_1(z) = P_p \dfrac{\mathrm{ch}(\beta\theta) + n\mathrm{sh}(\beta\theta)}{\mathrm{ch}\beta + n\mathrm{sh}\beta} \\ w_{p1}(z) = n_b P_p \dfrac{\mathrm{ch}(\beta\theta) + n^{-1}\mathrm{sh}(\beta\theta)}{\mathrm{ch}\beta + n\mathrm{sh}\beta} \end{cases} \tag{1}$$

where $w_{p1}(z)$ and $p_1(z)$ are, respectively, the displacements and axial force(stress) of pile shaft only under pile-top loads:

$$\begin{cases} w_{p2}(z) = \begin{cases} w'_{p2}(z) = \mathrm{C}_1\sin(\alpha z) + \mathrm{C}_2\cos(\alpha z) + s_0(h_0 - z)/h_0, & (0 \le z \le h_0) \\ w''_{p2}(z) = \mathrm{C}_3\sin(\alpha z) + \mathrm{C}_4\cos(\alpha z), & (h_0 \le z \le L) \end{cases} \\ P_2(z) = \begin{cases} P'_2(z) = -E_p A_p[\alpha C_1 \cos(\alpha z) - \alpha C_2 \sin(\alpha z) - s_0/h_0], & (0 \le z \le h_0) \\ P''_2(z) = -E_p A_p \alpha[C_3 \cos(\alpha z) - C_4 \sin(\alpha z)], & (h_0 \le z \le L) \end{cases} \end{cases} \tag{2}$$

where $w_{p2}(z)$ and $p_2(z)$ are, respectively, the displacements and axial force(stress) of pile shaft only under swelling pressure of expansive soils; h_0 denotes influenced depth of expansive soils; L pile length; s_0 soil surface heave; definition of other parameters refer to Fan et al. (2007).

Thus, the combination of both Equations 1 and 2 describe the pile-soil interaction in expansive soils:

$$\begin{cases} w_p(z) = w_{p1}(z) + w_{p2}(z) \\ P(z) = P_1(z) + P_2(z) \end{cases} \tag{3}$$

According to the work by Fan et al. (2007), only the following basic parameters are needed in analyzing the pile behavior in swelling soils: pile-top loads, shaft length, shaft diameter, elastic modulus of pile, shear modulus of the soil close to the shaft and to the pile-tip, wetting time, soil surface heave and influence depth of swelling soils. Simple programs are thereby compiled with regards to different situation of pile and soils parameters.

NUMERICAL ANALYSIS OF PILE IN EXPANSIVE SOILS UNDER DIFFERENT SITUATION

Note all figures below are ruled as: upward displacements>0; downward displacements<0; axial tensile force>0, axial compressed force<0.

Effect of Pile Length

The parameters for the calculating model are like follows: pile diameter d = 0.2m, pile length are 4m, 5.2m, 5.8m, 7m and 10m,respectively, viz. ratios of pile length to pile diameter are 20:1, 26:1, 29:1, 35:1 and 50:1, respectively. Influenced depth h_0 = 4m, upward topsoil movement s_0 = 0.02m and no loads on pile-top. The calculated displacement and axial force along the pile shaft are seen in Fig.1 and Fig.2, respectively

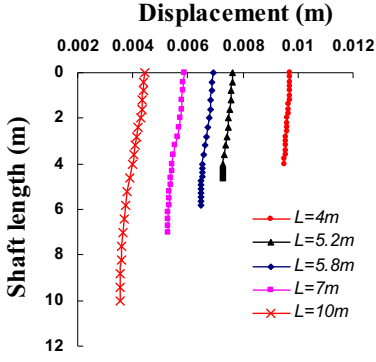


FIG. 1. Relation between axial displacement and pile length

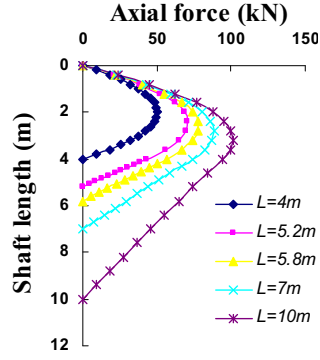


FIG. 2. Relation between pile axial forces and pile length

It is shown in Fig 1 with the increase of the shaft length, the displacements of the shaft decrease sharply. Given the same depth, the longer the shaft, the smaller the displacement of the shaft will be. This proves the availability of reducing the pile upward displacement by embedding the shaft at deeper subgrade. However, the embedded depth of pile is not suggested to be unlimited since it would be a waste of budget. Actually, the embedded depth should obey to exceed some critical depth. In our simulation in Fig.1, for the pile with 10m length (2.5 times of influenced depth), the pile-top upward displacement is 4.5mm, being 1/5 of the surface soil heave of 2cm. Even for the soil heave up to 10 cm, the pile-top upward displacement is 2cm which is still small enough in safety scale. It is close to the findings by Poulos and Davis (1980) that the critical embedded depth for pile shaft into subgrade is recommended to be, at least, 3 times of the expansive influence zone. The axial forces of the shaft would increase as the shaft length increase and the increments keep rising from the pile-top to the tip where the biggest increments occur. Meanwhile, for free pile without applied load, the maximum axial force stay around the middle of the shaft.

Effect of Pile Diameter

The parameters for the calculating model are like follows: pile length L = 10m， pile diameter are 0.2m (0.02L), 0.28m(0.028L), 0.44m(0.044L), 0.6m(0.06L) and 1m(0.1L), respectively. Influenced depth h_0 = 4m, upward topsoil movement s_0 = 0.02m and no loads on pile-top. The calculated displacement and axial force along the pile shaft are seen in Fig.3 and Fig.4, respectively.

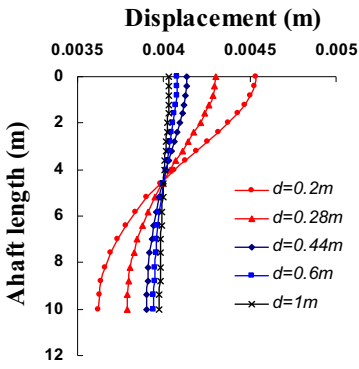


FIG.3. Relation between axial displacement and pile length

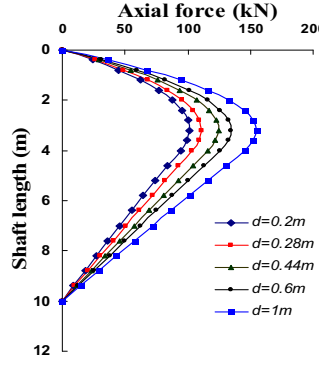


FIG.4. Relation between pile axial forces and pile length

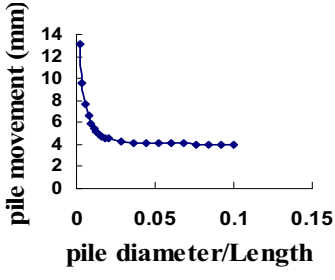


FIG. 5. Effect of pile diameter on pile movement

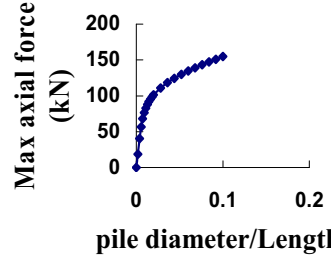


FIG. 6. Effect of pile diameter on maximum pile force

Fig 3 presents that the shaft displacements with various diameters intersect in a neutral point (the section where upward force is equal to downward force). It is clear seen increasing pile diameter could be helpful in reducing pile-top upward displacements. The diameters' effects on pile-top upward movements are also plotted in Fig 5 which suggests an approximate steady trend occurs once the diameter exceeds a critical value. In this simulation results (Fig. 5), the pile-top upward displacements only reduce by 10% from increasing $d = 0.045L$ to $d = 0.1L$, which means $d = 0.045L$ is around the critical diameter and the diameters exceeding $0.045L$ have little effect on reducing the pile-top displacements. This critical value is close to $0.03L$ proposed by Poulos and Davis (1980). As for axial force situation, it can be seen in Fig. 4 that increasing pile diameters could increase pile axial force and the biggest increments occur around the middle part of the shaft, then the increments decrease along the top and the tip of the pile till to be zero at the two ends of the shaft; On the other hand, increasing the diameter causes maximum axial shaft force to increase, which is

presented in Fig 6.

Effect of the Loads on Pile-top

The parameters for the calculating model are like follows: pile length L = 6m, pile diameter d = 0.2m, Influenced depth h_0 = 4m, upward topsoil movement is 0.02m, and loads on pile-top are 10kN, 127kN, 205kN and 400kN, respectively. The calculated displacement and axial force along the pile shaft are seen in Fig.9 and Fig.10, respectively.

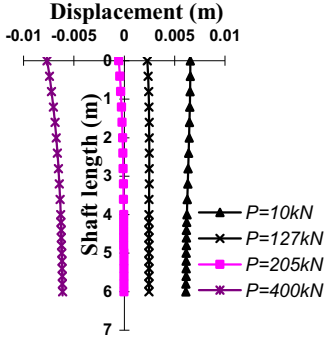


FIG. 9. Relation between axial displacement and pile length

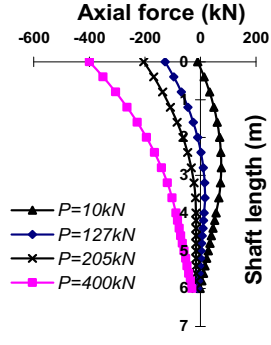


FIG. 10. Relation between pile axial forces and pile length

In Fig 9, the upward displacements of the shaft tend to decrease till zero with the increase of loads at pile-top. After that, settlements start to occur and become bigger and bigger as the loads continue to increase. Poulos and Davis (1980) proposed that the loads for stopping the upward movements of the shaft need to be, at least, half of the maximum swelling tensile force of the expansive soils. Actually, this is a particular conclusion suitable for the pile with the length of twice of influenced depth, and however, as for other pile of different length and influenced depth, the conclusions are different. In this simulation of pile with length L = 6m and influenced depth h_0 = 4m in Fig 10, only the applied load at the pile-top achieves 205kN, does the shaft settlement appears. Compared with the maximum swelling force of 80kN in this situation, the ratio of applied load to the swelling force is 2.5 that is the least loads ratio for stopping the upward movements of pile. Reasonably, the ratio will change if the pile length and/or influenced depth change. It is also presented in Fig.10 that the pile-top is subjected to compressed pressures which decrease along the shaft to the tip when loaded. The increments of compressed pressures reduce from the pile-top to pile-tip.

Effect of the time

Time-dependent behavior of pile in expansive soils is more complicated than other aspects listed before. The key problem is to ensure the deformation law of the soil that are close to the pile and then calculate the pile axial force and deformation based on pile-soil interaction differential equation. In our previous work (Zhang et al., 2007),

the author studied the heave relation to time of the pile-surrounded soil as presented in Equation (4):

$$s(z,t)=\begin{cases} A\cdot e^{-B/t}-\dfrac{A\cdot e^{-B/t}}{h_0}\cdot z, & 0\le z\le h_0 \\ 0, & z>h_0 \end{cases} \tag{4}$$

where, $s(z,t)$ refers soil heave at various depth; A and $B$are fitting parameters; h_0 influenced depth.

Repeating the derivation work (from Equation 15 to 24) in reference Fan et al. (2007), the time-dependent behavior of pile could thereby obtained.

The parameters for the calculating model are like follows: pile length L = 6m， pile diameter d = 0.2m, influenced depth h_0 = 4m, time are 60.9h,180.7h, 300.5h, 480h respectively. A and B are referred in Zhang et al. (2007), being 6.8634 and 0.027, respectively. The calculated displacement and axial force along the pile shaft are seen in Fig 11 and Fig 12, respectively

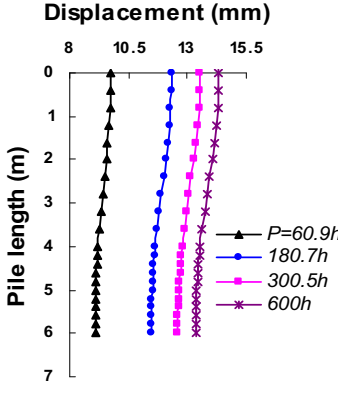


FIG.11. Relation between axial displacement and pile length

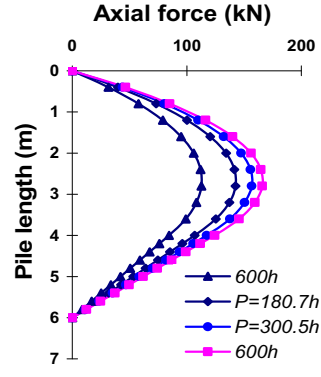


FIG. 12. Relation between pile axial forces and pile length

Fig.11 presents the shaft displacements increase with irrigation in proceeding. The displacement increments of the shaft keep reducing at same time interval as the time pass by. It means the pile displacements trends to be stable as the soil swelling trends to be stable. In Fig.12 the longer the time of introduction of water, the bigger the axial force will be and the biggest incremental forces locate around the middle of the shaft. The increments of axial forces decrease along the two ends of the shaft until zero. At same time interval, the increments of axial forces reduce as well, trending to be zero as soil swelling is close to being stable.

CONCLUSIONS

1）Increasing pile length may decrease the upward shaft displacement but if too long, the soil swelling-induced tensile force for a pile might increase too big to be safe. In this simulation work, minimum pile length is suggested to be 2.5 times of influenced depth

2）Piles with small diameter (d ≈ 0.045L) under influenced depth are able to effectively reduce the upward shaft displacement; however, diameters exceeding 0.0045L have little effect on decreasing shaft displacement.

3）Loads for stopping the upward pile movements depend on different pile length and influenced depth, which is some ratios of maximum swelling force. Thus, the ratio might be 0.5 suggested in Poulos and Davis (1980) or 2.5 in this simulation example.

4）As irrigation proceeds, the upward shaft movements and axial tensile force keep increasing while the increments of the both are less and less at the same time interval, and trend to be zero when soil swelling tends to be stable.

ACKNOWLEDGMENTS

The funding for the research presented in this paper was provided by National Science Foundation of China (No.50378097)

REFERENCES

Fan, Z.H., Wang Y.H., Xiao H.B., and Zhang C.S. (2007). "Analytical method of load-transfer of single pile under expansive soil swelling." *Journal of Central South University of Technology*, Vol. 14 (4): 575-580.

Xiao, H.B. (2005). "Theoretical and application research on load transfer of vertically loading large diameter piles." Central South University.

Wei, D.G.，and Randolph, M.F. (1998). "Rationality of load transfer approach for pile analysis." *Computers and Geotechnics*, Vol. 34(2-3): 85-112

Aschenbrener, T.B. and Olson, R.E. (1984). "Prediction of settlement of single pile in clay." *Proc. of Symposium by ASCE Geotech*, edited by J R Meyer: 41-58

Poulos H.G, and Davis E.H. (1980). "Pile foundation analysis and design". New York: John Wiley & Sons.

Zhang C.S., Xiao H.B., Zeng Q.G., and Fan Z.H. (2007). "Law of pile in expansive soils with introduction of water." *Proceedings of GEO-CHANGSHA 2007, an International Conference on Geotechnical Engineering*: 431-439

This page intentionally left blank

Author Index

Page number refers to the first page of paper

Cao, Wen-Gui, 30, 78
Chen, Cheng, 9
Chen, Qingfa, 57
Cheng, Wen-Chieh, 1, 64
Choi, Yongkyu, 50

Fan, Zhen-Hui, 99

Gao, Feng, 57
Gao, Zhuang-Ping, 72
Ge, Louis, 9
Gua, Chengchao, 84

Hwang, Woong-Ki, 50

Johnson, Dona, 44

Kasbergen, C., 24
Kim, Chan-Kee, 50
Kim, Tae-Hyung, 50

Lee, Minhee, 50
Liu, Bao-Chen, 16
Liu, Xueyan, 24
Liu, Yan, 36
Lu, Ting-Hao, 72

Ni, James C., 1, 64
Nie, Ru-Song, 16

Scarpas, A., 24
Shi, Jian-Yong, 92
Sukumaran, Beena, 44

Wang, Peng, 84
Wang, Yong-He, 99

Xiao, Hong-Bin, 99

Yang, Xiao-Li, 16
Yu, Xiao-Jun, 92
Yu, Xinbao, 36
Yu, Xiong (Bill), 36

Zhang, Chun-Shun, 99
Zhang, Jia Sheng, 9
Zhang, Ling, 78
Zhang, W. X., 24
Zhang, Yong-Jie, 30
Zhao, Heng, 78
Zhao, Ming-Hua, 30
Zhou, Ai-Zhao, 72
Zhou, Keping, 57
Zhou, Zhong, 16

This page intentionally left blank

Subject Index

Page number refers to the first page of paper

Aircraft, 44
Airport runways, 44

Bedrock, 64
Buildings, multistory 1

Clays, 1, 92
Concrete structures, 1
Constitutive models, 24, 72, 78

Damage, 78
Data analysis, 64
Deformation, 16

Embankments, 72
Excavation, 1, 16
Expansive soils, 99

Finite element method, 44
Flexible pavements, 44
Freeze-Thaw, 36
Fuzzy sets, 30

Granular materials, 9, 24, 36
Grouting, 1

Highway and road construction, 16
Highways and roads, 57
Hydraulics, 64

Load factors, 78

Measurement, 36
Mechanical properties, 24
Mixtures, 16
Monte Carlo method, 30

Numerical models, 99

Pavement design, 9
Pore pressure, 50
Pumps, 64

Repeated loads, 9
Research, 92
Resilient modulus, 9
Roadbeds, 92
Rock masses, 57
Rocks, 16, 30, 64, 78

Sediment, 64
Shafts, 99
Shear deformation, 99
Simulation, 24, 99
Slope stability, 16, 30
Soft soils, 1, 64, 92
Soil compaction, 50, 84
Soil compression, 50
Soil deformation, 84
Soil suction, 36
Soil-pile interactions, 99
Soils, 16
Soil-structure interactions, 72
Statistics, 78
Strain rates, 78
Stress, 72
Subgrades, 84

Tests, 84

Unsaturated soils, 50

Volume change, 50

Wheels, 44